MASTER DEGREE THESIS IN MEDICAL PHYSICS AND TECHNOLOGY

DEPARTMENT OF PHYSICS AND TECHNOLOGY

UNIVERSITY OF BERGEN

A Comparative Study of Radiation Environment and Secondary Dose Production in a Particle Therapy Treatment Room Applying Proton, Helium and Carbon Ion Beams

Author:
Jarle Rambo Sølie
Supervisors:
Professor Dieter Röhrich
Dr. Scient. Odd Harald Odland

November 20, 2015

This page intentionally left blank.

Acknowledgements

I would like to express my deepest gratitude towards my supervisors, Professor Dieter Röhrich and Dr. Scient. Odd Harald Odland.
Professor Dieter Röhrich, it was your inspiring lectures that lead me towards a masters degree in medical physics and awoke my passion for radiation physics and radiation protection. You have been an indispensable source of knowledge during this project and I thank you for always keeping an open door.

Thank you Dr. Scient. Odd Harald Odland for introducing me to the field of radiation protection and planning this master thesis with me. Your encouragement, comprehensive feedback and suggestions have been instrumental in the execution and completion of this thesis.

Thanks to Kristian Ytre-Hauge for being most helpful and patient with my questions about both big and small things in FLUKA.

To my fellow students, Eivind, Lars Fredrik, Susanne and Kristian, I offer my warmest thoughts and well wishes.

Thanks to my room mates, especially Ingrid, your conversation and easygoing nature helped me relax when I needed it the most.

Special thanks to Alina Tanja Karafiat for everything that she is, you have thought me more about life than any other person and I'm forever grateful and thinking about you.

A special thanks to my parents, Trine Rambo Sølie and Isak Sølie for their weekly phone calls and boundless encouragement.

This page intentionally left blank.

Abstract

A treatment room used for radiotherapy is generally heavily shielded and has to fulfil and abide to strict rules and regulations in order to ensure the safety and health of hospital personnel and the general public that find themselves in the vicinity of the treatment room during beam time. Secondary particles, especially neutrons and photons due to their neutral property and induction rate, can carry and deposit energy a significant distance away from their initial production site and potentially cause unintended damage and adverse effects in living tissue and materials. Neutrons and photons are induced when energetic particles interact and collide with matter, and in a radiotherapy treatment setting occurs not only in beam components (degrader, collimator, etc.) that are introduced into the beam line, but also in the patient and surrounding shielding. Fixed beam scanning therapy has the advantage of requiring a minimal number of beam components in the beam line and thus contain the main induction of secondary particles to the patient and surrounding geometries. In this thesis a basic treatment room with realistic dimensions modelled after a fixed beam scanning system facility, and a water phantom functioning as a substitute patient, was implemented in the Monte Carlo simulation package *FLUKA*, and the geometry created using the *flair - FLUKA Advanced Interface*. The beam placement, thickness and placement of main treatment walls, size and location of water phantom and the treatment volume were all kept constant and consistent in all simulations when applied. All results were further processed and normalised to a single fractional delivery of 2Gy in the treatment volume.

The purpose of this master thesis has been to perform a comparative study of the induced radiation environment inside a typical treatment room during irradiation of a water phantom with proton, helium and carbon beams, and introduce various entrance structures and shielding materials to the treatment room in order to compare and illuminate their effects and study the differential fluence spectra of neutrons and photons entering and exiting these featured structures. Water equivalent worker phantoms representing hospital personnel were placed inside and outside the vicinity of the entrance structures and effective dose to each of them were scored. A total of 24 simulations covering eight different treatment room layouts were performed in FLUKA and the final results illuminated the many considerations and deliberations that must be taken into account during the planning, building and shielding fitting of a treatment room for use in particle therapy.

This page intentionally left blank.

Contents

List of Abbreviations

Abbreviation	Description
CTV	Clinical Target Volume
FLUKA	FLUktuierende KAskade
IAEA	International Atomic Energy Agency
ICRP	International Commission on Radiological Protection
NCRP	National Council on Radiation Protection and Measurements
NRPA	Norwegian Radiation Protection Authority
SOBP	Spread Out Bragg Peak
TV	Target Volume
UNSCEAR	United Nations Scientific Committee on the Effects of Atomic Radiation

List of Figures

List of Tables

Chapter 1

Introduction

Continuous developments in modern medicine and accelerator technology, and understanding of how energetic particles in the atomic world interacts with matter, has created efficient cancer treatments that offer improved tumour control and low probability of side effects compared to radiation therapy with photons. Through the depth-dose characteristics of accelerated protons, helium and Carbon ions makes it possible to deliver a dose to a target volume with high precision. The first particle therapy facilities were built as early as 1957 and were mainly used as research laboratories. In 2014 there were 48 particle therapy facilities in clinical operation around the world and in September 2013 the Norwegian Minister of health announced that proton therapy facilities will be established in the respective administrative health regions in Norway.

The planning and building of a particle therapy center is a costly and complicated affair not least due to the radiation safety aspect that must be adhered too and follow the regulations set in place to ensure the safety of the general public and hospital personnel in the vicinity. While it is agreed upon that radiation effects increases with the absorbed dose, there is no general consensus on set exposure limits. Instead, planned exposure situations follow a "as low as reasonably applicable" principle coupled with a recommended dose limit that should not exceed 20 mSv/year to an individual in an occupational setting or 1 mSv/year to a member of the public. Medical particle therapy is considered a planned exposure situation and thus requires careful planning and insight into a significant number of aspects, not only limited to daily management, but also to shielding calculations and estimates that affect building layouts, materials and detemination of areas to be kept under supervision.

With the aid of the Monte Carlo simulation tool FLUKA, this thesis aims to deliver insight into the radiation environment induced inside a a typical fixed beam particle therapy treatment room where protons, helium, and carbon ions are applied. Special geometries are introduced in separate simulations where alternative entrances and shielding materials are featured. The fluence and energy spectra of secondary particles, especially neutrons and photons due to their penetrative properties, that exits and enters the featured structures are scored and plotted in

informative plots and tables. Parallel to these measurements, effective dose scoring in worker phantoms located inside and in the immediate surroundings of the simulated geometry are scored and used to calculate the annual dose.

The overall goals of this thesis has been:

- Create an actively modulated proton, helium and carbon beam in FLUKA that results in a spread-out Bragg peak and suitable dose coverage of a clinical target volume located inside a water phantom functioning as the patient.

- Investigate the secondary particles induced when a Monte Carlo simulated proton, helium, and carbon treatment beam interacts with a homogeneous water phantom (human tissue approximation) and how the secondary particles propagates in the treatment room.

- In the "FLUKA Advanced Interface", flair, use the geometry editor to design and build a typical treatment room used in a fixed beam therapy setting and introduce various structures and barriers that functions as entrances and shielding. Finally place human sized water phantoms at locations inside the various entrances as well as outside primary shielding barriers.

- Compare proton, helium and carbon beam induced particle fluence entering and exiting structural hallways and primary barriers.

- Score the effective dose in pre-arranged water phantoms functioning as hospital personnel and calculate the yearly workload they receive in these positions.

Chapter 2 introduces the basic physics most relevant for radiotherapy and are of concern in radiation protection. Most prevalent are the interactions of charged particles, photons and neutrons with matter. This chapter aims to build a foundation of physical concepts that are involved when considering and discussing the origins of a radiation environment induced by the interaction of energetic particles with matter.

Chapter 3 handles the biological effect of induced radiation on living tissue and introduces the concepts, and radiological weighting factors, that are involved in evaluations of a radiation environment and its potential effects on human tissue.

Chapter 4 continues building on the theoretical foundation by introducing the technology and methods involved in dose delivery, and concepts of LET and RBE that make up the rationale behind the use of different particles in radiotherapy.

Chapter 5 forms the final piece in this thesis's theoretical foundation and introduces the principles of radiation protection and shielding in a radiotherapy setting.

Chapter 6 provides a general summary of the Monte Carlo method and FLUKA particle transport code used in this thesis.

Chapter 7 describes the process of creating the three simulated proton, helium, and carbon treatment beams in FLUKA. Outlines the various simulation setups and treatment room layouts that were designed and simulated, together with their respective results and dose calculations.

Chapter 8 contains a final discussion and outlook.

All FLUKA Monte Carlo simulations in this thesis is produced by the author, unless specified otherwise.

Chapter 2

Radiation Physics

In this chapter the basic and most relevant concepts in radiation physics relating to radiation therapy and radiation protection will be presented. In general, radiation is categorized as either *non-ionizing* or *ionizing* depending on whether the radiation is carrying sufficient energy to ionize atoms or not. Ionizing radiation, including γ*-rays*, *X-rays*, *Charged Particles* and *Neutrons*, have the power to excite and ionize atoms by transferring energy to valence electrons and atomic nuclei on its path through matter[1]. These energy transfers occur via several different interaction processes and the energy imparted to individual atoms will cause a highly localised concentration of absorbed energy. This energy absorption can consequently induce biological effects in tissue and has therefore found an application in radiotherapy in medicine. This application makes it imperative to understand the physics and models involved in the interaction between radiation and matter.

2.1 Interactions of Charged Particles with Matter

Heavy charged particles, such as protons and heavy ions, that travel through matter will mainly interact and lose energy via *inelastic collisions* with valence electrons and cause ionizations and excitations of atoms in their path. The incoming charged particles may also experience deflections from their incident direction due to elastic scattering on nuclei, complicating the analysis of particle paths and energy deposition in matter. *Bremsstrahlung*, *Cherenkov Radiation* and *nuclear reactions* may also occur, but these processes are rare compared to electromagnetic interactions and inelastic collisions which are almost solely responsible for the energy loss of heavy charged particles in matter [2].

2.1.1 Energy Loss by Ionization

A charged particle surrounded by its own Coulomb field, will interact with the Coulomb field within every atom it passes and lose a small fraction of its incident energy through inelastic collisions with the atom's orbital electrons [1].

Instead of calculating this energy loss classically with Bohr's formula in terms of the impact

parameter, the more correct quantum mechanical *Bethe formula*, parametrized by the measurable momentum transfer, is used in calculations. [2]. The average energy loss of a heavy charged particle per unit path length, dE/dx $[MeV/cm]$, also called the *stopping power*, is given by the Bethe formula and reads;

$$-\frac{dE}{dx} = K\rho\frac{Z}{A}\frac{z^2}{\beta^2}\left[\ln(\frac{2m_ec^2\beta^2\gamma^2W_{max}}{I^2}) - 2\beta^2 - \delta - 2\frac{C}{Z}\right], \tag{2.1.1}$$

where

$$K = 2\pi N_A r_e^2 m_e c^2 \approx 0.307 MeV mol^{-1} cm^2 .$$

Certain important effects and observations are of note in Bethe's formula: i) To the first order the energy loss is proportional to the inverse square of the incoming particle's velocity, $1/\beta^2$. So as the incoming particle slows down in matter due to its energy loss, and experiences the electric force from atomic electrons for a longer time, it will deposit more of its energy until reaching a certain point where it will deposit all its energy and stop completely. This is illustrated by a sharp dose enhancement referred to as a *Bragg Peak* when plotting depth-dose curves for heavier charged particles (found in more detail in the Bragg Peak topic 2.1.5). There is also a strong dependence on the square of the incident particle's charge, z^2, so for heavier nuclei this dose enhancement effect is even more pronounced [3]. ii) By dividing the stopping power 2.1.1 with the density of the absorber material, the *mass stopping power*, $dE/\rho dx$ $[MeVcm^2/g]$ is obtained, and because the ratio Z/A is observed to have little variation from material to material, from $\sim$ 0.5 for low Z to $\sim$ 0.5 for high Z (except for Hydrogen where $Z/A \approx 1$), the mass stopping power is almost independent from the type of absorber material. Meaning that the incident charged particle will lose about the same amount of energy per g/cm^2 in any type of pure material [3]. For compound materials, 2.1.1 must be modified by using *Bragg's additivity rule*, which states that the stopping power of a molecule or material is the sum of the stopping power of all the atoms it is composed of and thus defining effective values for Z, A, I, etc.:

$$Z_{eff} = \Sigma a_i Z_i ,$$

$$A_{eff} = \Sigma a_i A_i ,$$

$$\ln(I_{eff}) = \Sigma\frac{a_i Z_i \ln(I_i)}{Z_{eff}} ,$$

$$\delta_{eff} = \Sigma\frac{a_i Z_i \delta_i}{Z_{eff}} ,$$

$$C_{eff} = \Sigma a_i C_i ,$$

where a_i is the number of atoms in compound i [2].

In figure 2.1, a representation of the stopping power 2.1.1 as a function of an incoming charged particle's kinetic energy is plotted, starting at zero and for increasing energy, three

Table 2.1: Parameters involved in the Bethe Formula [2, p.24].

N_A	Avogadro's number $= 6.022 \times 10^{23} mol^{-1}$
r_e	Classical electron radius $= 2.818 \times 10^{-15} m$
m_e	Electron rest mass $= 0.511 MeV/c^2$
c	Speed of light $= 299792458 m/s$
z	Charge of incident particle in units of e
ρ	Density of absorber material
Z	Atomic number of absorber
A	Atomic weight of absorber in units of g/m
β	v/c of the incident particle
γ	Lorentz factor $1/\sqrt{1-\beta^2}$
W_{max}	Maximum energy transfer in a single collision
I	Mean excitation potential (eV)
δ	Density correction
C	Shell correction

regions are of note. In the low energy region (1), $\beta \leq 0.05$, particles tend to pick up electrons, effectively lowering the charge and thus the stopping power. Due to these electron capture effects the Bethe formula breaks down and there is no satisfactory theory to take its place in this region. In the intermediate energy region (2), the stopping power decreases until the particle reaches velocity, $v \approx 0.96c$, when the particle is considered to be *minimum ionizing*. With increasing energy in the relativistic region (3), there is a *relativistic rise* due to the logarithmic dependence and correction terms in 2.1.1 [2].

It is also of note that for electrons and positrons, the Bethe formula must be modified in order to take into account the added energy loss mechanism from scattering, as the low mass of electrons and positrons give them a higher probability to scatter on atomic nuclei and radiate electromagnetic radiation (*bremsstrahlung*) [2].

2.1.2 Range

Since a charged particle traversing through matter continuously lose energy from undergoing a multitude of interactions, it will trace out a path until stopping completely due to its energy loss. This *path-length* will approach an expectation value called *range*, $\mathcal{R}$, and is a characterization of the charged particle's type, energy and specific medium it traverses [1].

Assuming the charged particle continuously lose energy at a linear rate along its path, the range can be found by integrating over the reciprocal of the stopping power 2.1.1 [4],

$$\mathcal{R} = \int_0^R dx = \int_0^E \left(-\frac{dE}{dx} \right)^{-1} dE \, . \tag{2.1.2}$$

The stopping power is proportional to $1/\beta^2$, which varies with the energy, so it is expected that the range is proportional to E^2 as can be seen in the semi-empirical approximation of the

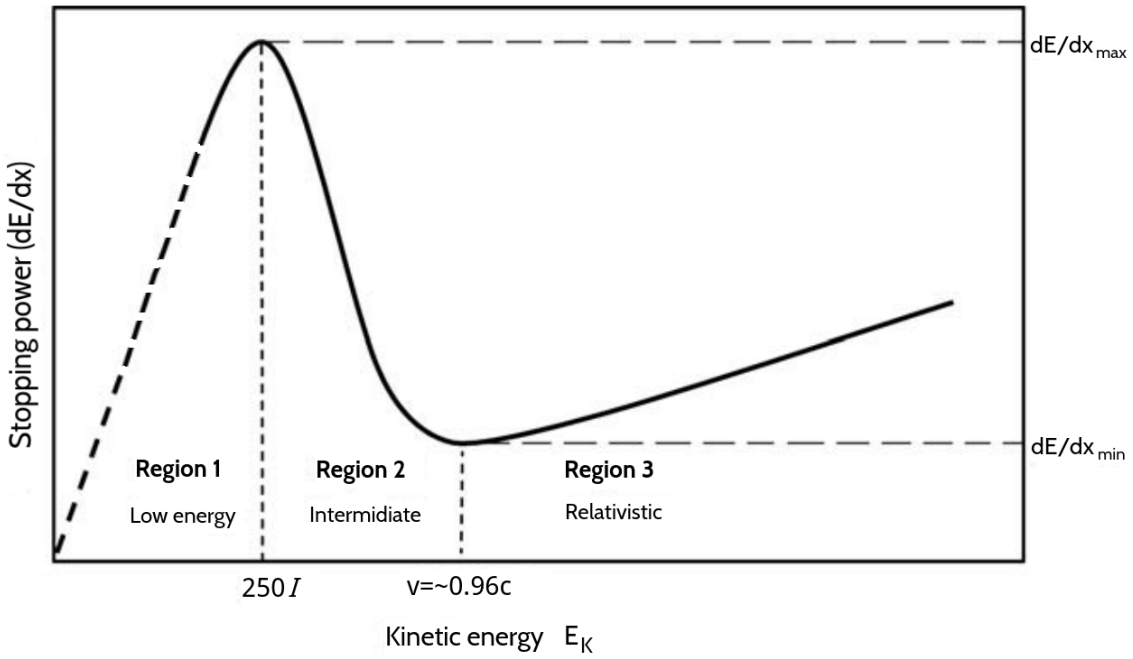

Figure 2.1: Representation of the stopping power as a function of the kinetic energy of a heavy particle [3, p.248].

range based on a simplified Bethe formula [5],

$$\mathcal{R} \approx \frac{\pi \epsilon_0^2 m_e E^2}{n_A Z_A Z^2 e^4 M}\,, \tag{2.1.3}$$

where ϵ_0 is the permittivity of free space and $n_A Z_A$ is the average electron density of the material. It is important to note that the range calculated by 2.1.2 is only valid as long as inelastic atomic collisions are the principal mean of energy loss. This is the case for heavy charged particles in the therapeutic energy range and the results are accurate within a few percent [2]. Based on certain assumptions that the error in 2.1.3 are the same for different particles and energies, it is possible to derive scaling laws for the ranges [5, 2]:
i) For different particles in the same medium,

$$\mathcal{R}_2(E_2) = \frac{M_2}{M_1}\frac{z_1^2}{z_2^2}\,\mathcal{R}_1\left(E_2\frac{M_1}{M_2}\right)\,. \tag{2.1.4}$$

ii) For two absorber materials with different densities ρ_0, ρ_1 and atomic weight A_o, A_1, where the range is known in one, we can estimate the range of the charged particle in the other based on the Bragg-Kleeman rule [6],

$$\frac{\mathcal{R}_1}{\mathcal{R}_0} \cong \frac{\rho_0\sqrt{A_1}}{\rho_1\sqrt{A_0}}\,. \tag{2.1.5}$$

iii) A rough approximation of the range in a compound can be found from

$$\mathcal{R}_{comp} = \frac{\mathcal{A}_{comp}}{\Sigma \frac{a_i \mathcal{A}_i}{\mathcal{R}_i}} \ , \tag{2.1.6}$$

where $\mathcal{A}_{comp}$ is the molecular weight of the compound, a_i is the number of atoms in the ith compound element molecule, and $\mathcal{A}_i$ and $\mathcal{R}_i$ are the atomic weight and range of the ith constituent element respectively [2].

When studying range curves it is observed that the range follows a simple power law equation,

$$\mathcal{R}(E) = \alpha E^p \ , \tag{2.1.7}$$

where E is the initial energy of the particle, α is a material-dependent constant and p is an energy-dependent parameter that are obtained by fitting 2.1.7 to experimental range or stopping power data [7, 8].

2.1.3 Multiple Coulomb Scattering

Another phenomenon of concern in analysis of particle paths are the scattering from atomic nuclei due to the Coulomb force. Multiple small-angle scattering events, referred to as multiple Coulomb scattering, causes a heavy charged particle to deviate from a straight line, resulting in beam divergence illustrated in figure 2.2 [4].

The conical angular distribution of such a deflection is roughly Gaussian at small angles and the solid angle θ^{rms}_{space} where 98% of the beam is concentrated is given by [9]:

$$\theta_0 = \theta^{rms}_{plane} = \frac{1}{\sqrt{2}} \theta^{rms}_{space} \ , \tag{2.1.8}$$

$$\theta_0 = \frac{13.6MeV}{\beta c p} z \sqrt{\frac{x}{X_0}} [1 + 0.038 \ln(\frac{x}{X_0})] \ , \tag{2.1.9}$$

where z is the charge of the incoming particle, βc is the velocity, p is the momentum in MeV and x/X_0 is the thickness of the material in radiation lengths, which can be approximated by,

$$X_0 = \frac{716.4A}{Z(Z+1)\ln(\frac{287}{\sqrt{Z}})} \ . \tag{2.1.10}$$

For $10^{-3} < x/X_0 < 100$, θ_0 is accurate to 11% or better [10].

Generally, the lateral displacement and width of the beam due to multiple Coulomb scattering decreases with increasing charge and mass of incoming particle, but increases for materials with high Z and for low energies as described by the $\beta c p$ term in the denominator of 2.1.9, resulting in a lateral widening of the beam as illustrated in figure 2.3 for some proton and carbon energies [11].

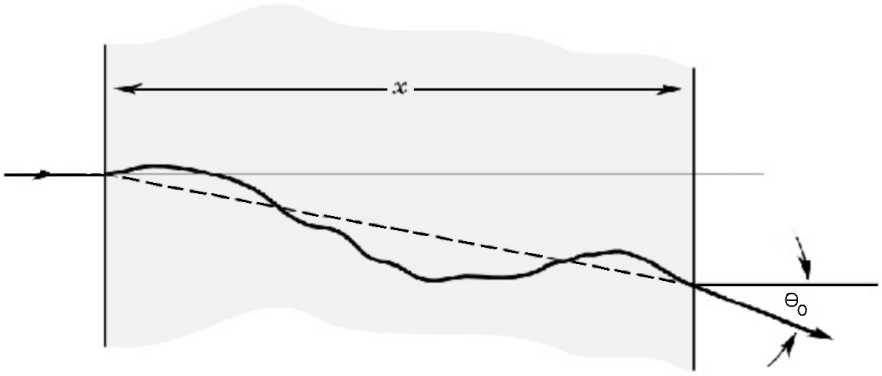

Figure 2.2: An exaggerated representation of the lateral displacement due to multiple Coulomb scattering of a heavy charged particle after a thickness of material x [9].

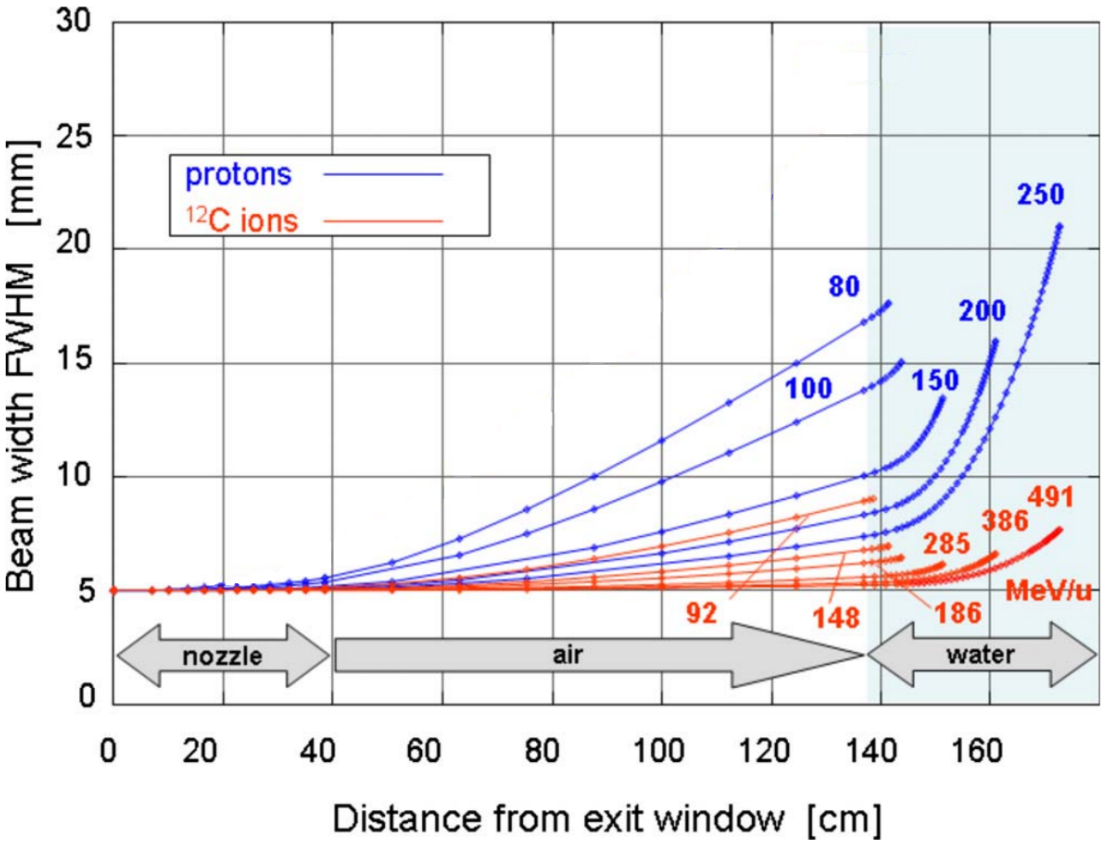

Figure 2.3: Lateral width, of a typical treatment beam line with an initial FWHM of 5mm, as a function of path length for proton and carbon ions in air and water. This illustrates the increased lateral displacement of particles with lower energies and charges, and when penetrating materials with higher Z [11].

2.1.4 Straggling

Fluctuations in the range will also occur because of the statistical nature of particle interactions and energy loss in matter. Due to this random nature, not all mono-energetic particles entering an absorber will travel the exact same path, resulting in statistical variations referred to as *range straggling*, σ_{rs} and *energy straggling*, σ_{rs}. To the first approximation, straggling follows a Gaussian distribution with a straggling parameter that depends on the massive-particle charge and velocity, and the atomic number and ionization energy of the absorber [12].

The ratio of the range straggling and mean range is roughly proportional to $1/\sqrt{M}$, causing heavier ions to experience less straggling, narrowing the localisation of deposited dose [11]. For heavy charged particles the range straggling is only of a few percent and thus travel in an approximately straight line while being narrowly distributed around the mean range [4].

2.1.5 Bragg Peak

As a charged particle loses velocity due to the energy loss caused by interactions with matter, the cross section and interaction rate increases and causes a sudden maximum energy transfer close to the particle's range. This results in the phenomena know as a *Bragg Peak* and is used in hadron therapy to concentrate the dose, and consequently the biological effect, to a given area. After the Bragg peak has reached its maximum, the dose quickly falls to zero for protons, but for particles heavier than protons a dose tail appears due to *fragmentation* [13], which is discussed in the fragmentation topic 2.1.6 below. For a mono energetic beam experiencing range and energy straggling effects there is also a broadening of the Bragg peak to a few millimetres as seen in figure 2.4. The width between the distal 80%, d_{80} and 20%, d_{20} dose level in the Bragg peak depend on the quadratic sum of these two straggling effects [14],

$$d_{20} - d_{80} = 1.3\sqrt{\sigma_{es}^2 \sigma_{rs}^2}\,. \tag{2.1.11}$$

Generally, the straggling is roughly proportional to the inverse square root of the mass of the particle, so for protons this widening is more pronounced than it is for heavier particles [15], as observed in figure 2.4 below.

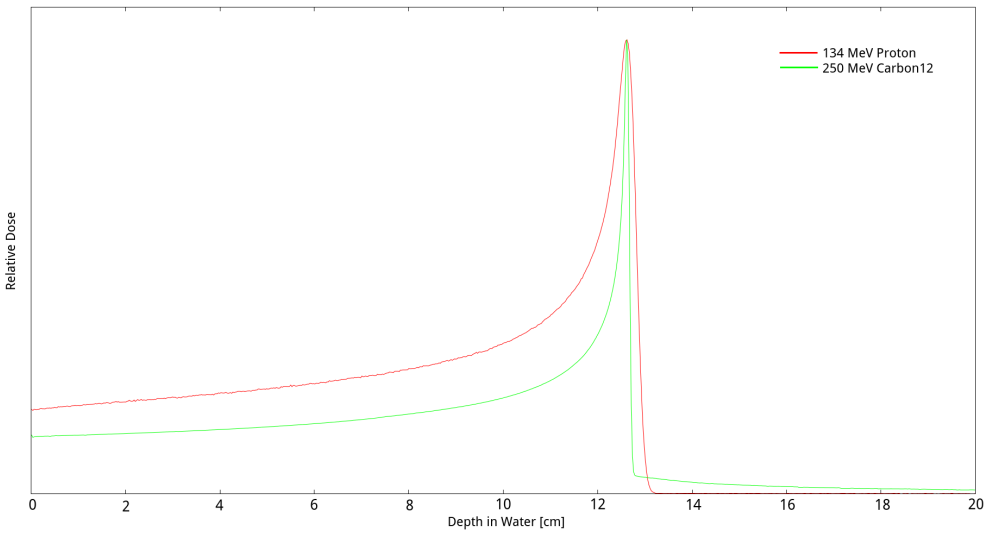

Figure 2.4: FLUKA Monte Carlo Simulations. Comparison of simulated Bragg peaks for a proton and Carbon (^{12}C) beam normalized to the same peak height. The broader width of the Proton Bragg peak is due to stronger straggling effects while the tail at the end of the Carbon Bragg peak is due to fragmentation.

2.1.6 Nuclear Fragmentation

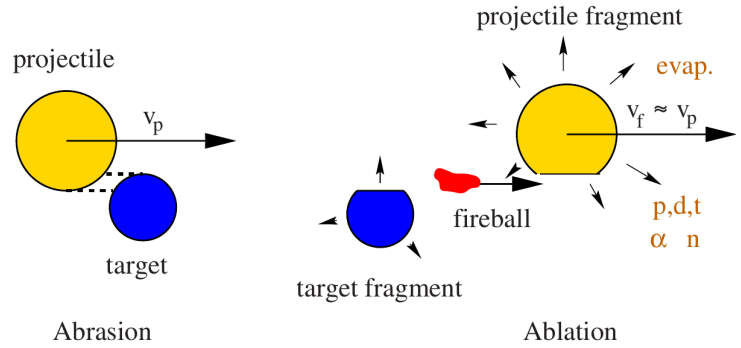

Figure 2.5: Illustration of nuclear fragmentation described by the Abrasion-Ablation model [11].

In fragmentation, incoming charged particles heavier than protons may lose one or more of its nucleons via peripheral collisions with nuclei in matter as described by the *abrasion-ablation* model shown in figure 2.5. In the first abrasion step, nucleons in the overlapping zone between the projectile and target nuclei are abraded and form a reaction zone ("fireball"). The remaining fireball, projectile and target fragments then de-excite in the ablation step by evaporating light clusters and nucleons. This process leads to significant effects such as attenuation of the primary beam flux and a build-up of lower Z fragments [11].

Neutrons and light clusters from the target fragment are isotropically emitted and have much lower energies than the primary ions. Particles emitted from the projectile nuclei how-

ever, are forward peaked with an angular FWHM that diminish with the increasing Z of the fragments. Fragment energies are also close to the beam energy at the point of abrasion, this causes the characteristic *dose tail* to appear behind the Bragg peak due to the larger penetrative depth of lower-Z fragments. While the energy distribution of heavier fragments extends up to the incident beam energy, neutrons and protons can extend up to twice the energy of the incident projectile per nucleon, which is explained by the Fermi-momentum transfer from the target nucleons [16].

2.1.7 Hadronic Cascade

When a high energy particle interacts with matter, a cascade (shower) of secondary particles with lesser energy are produced, which can in turn produce new particles in the same manner and continue the cascade. Hadronic cascade is the most important means of transporting radiation through shielding barriers. There are six distinct and independent processes involved in a hadronic cascade as illustrated in figure 2.6. The extra-nuclear cascade is the most important due to the hadrons interacting directly with the nucleus and releasing forward directed particles that propagate the shower further. Intra-nuclear cascade may also occur when the incoming particle interacts with individual nucleons inside the nucleus, this creates similar particles as the extra-nuclear, but at lower energies at wider angles. Above the pion production threshold (135 MeV), pions may also contribute to the cascade by initiating an electromagnetic cascade when decaying into two photons. Some of the charged pions and kaons will also release a muon when decaying and this will deposit its energy by ionization due to being a very penetrating particle. The remaining struck nucleon de-excites by emitting mainly low energy neutrons and protons (as described in the nuclear fragmentation section) that deposits energy both locally (protons) and continuously over a distance (neutrons). The de-excited nucleus may also be radioactive and emit α , β or γ radiation. For incident hadrons with therapeutic energies, intra-nuclear cascade is the principal process and special consideration are paid to the induced neutrons in intra-nuclear cascades as the induced charged particles do not contribute significantly to the energy transport in matter since they are quickly stopped through their energy loss via ionization. Neutrons are therefore the main propagators of energy in barriers and requires special attention in shielding applications [17, 18].

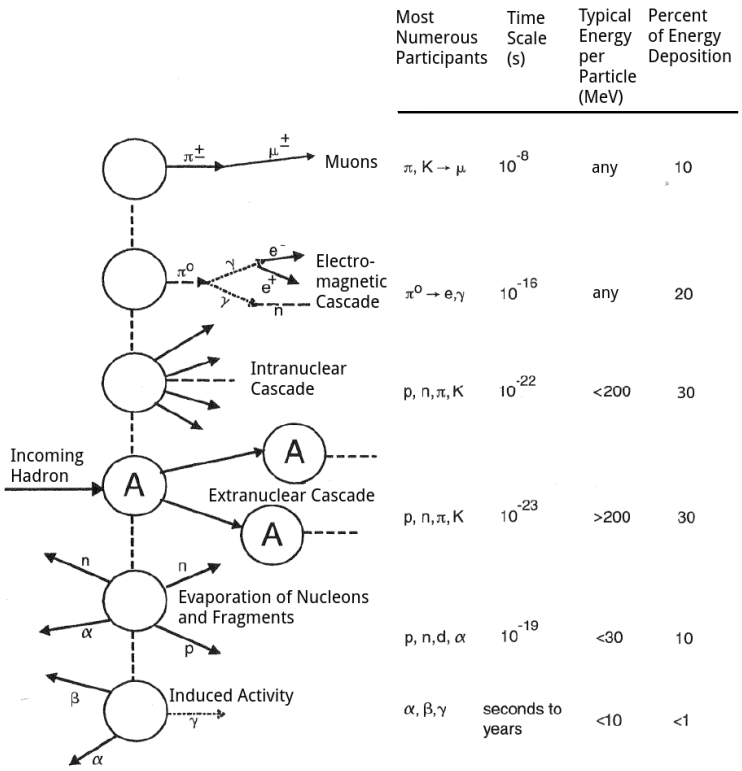

Figure 2.6: Illustration of the six levels of hadronic cascade [18].

2.2 Interactions of Photons with Matter

Photons are neutral, massless particles that carry electromagnetic energy and indirectly ionizes atoms by transferring energy to charged particles through the principal interactions *Photoelectric Effect*, *Compton Scattering* and *Pair Production*. Other interaction processes include elastic *Rayleigh Scattering* that redirects the photon, but does not cause ionization, excitation nor energy transfers to charged particles, and *Photo-nuclear interactions* where photon energies above a few MeV may produce neutrons. These interactions and their effects are not discussed in great detail in this thesis, but their effects are observed in measurements of the total cross section contributions seen in figure 2.7 [1, 5].

The total cross section of a photon interaction is the sum over all the contributing photon interaction cross sections,

$$\sigma_{tot} = \sigma_{pe} + \sigma_{comp} + \sigma_{ray} + \sigma_{pairn} + \sigma_{paire} + \sigma_{ph.n} \ , \tag{2.2.1}$$

where σ_{pe} is the photoelectric effect, σ_{comp} and σ_{ray} are Compton and Rayleigh scattering respectively, σ_{pairn} and σ_{paire} are the cross sections for pair production in the nucleus and in the atomic electrons, and $\sigma_{ph.n}$ is the photo-nuclear cross section [19].

Depending on the incoming photon energy and the density and atomic number of the absorber, a photon may interact with an orbital electron or with the nucleus of an atom. The

photon is then either absorbed and a portion of its energy transferred to an electron or used to create an electron-positron pair, or the photon is scattered with or without an energy loss [3]. So contrary to charged particles that experience energy degrading and have a characteristic range in matter, photons only experience a loss in intensity as they are either attenuated or transmitted in matter. This loss of intensity is given by the exponential decay law,

$$I(x) = I_0 e^{-\mu x} \,, \tag{2.2.2}$$

where I is the intensity at depth x. I_0 is the intensity without an attenuator and μ is the linear attenuation coefficient, which denotes what fraction of the intensity is lost per unit length. The linear attenuation coefficient is also related to the total cross section via

$$\sigma_{tot} = \frac{\mu A}{\rho N_A} \,, \tag{2.2.3}$$

where A is the atomic mass, N_A is Avogadros number and μ/ρ is the *mass attenuation coefficient* [5]. The linear attenuation coefficient is observed to increase with the atomic number Z and density ρ of the absorber, and decrease with increasing photon energy, E_γ. Table 2.2 lists the energy range and Z-dependence of some processes that contribute to the attenuation of a photon beam. Primarily, attenuation is caused by the photoelectric effect, Compton scattering and pair production, and these processes will be introduced in more detail in their respective sections below [20].

Table 2.2: Table of processes contributing to the attenuation of a photon beam [5]

Process	Target	Energy range	Z-dependence	Comment
Photoelectric effect	Bound electron	$0 - 0.5MeV$	$Z^4 - Z^5$	Absorbed photon
Rayleigh Scattering	Bound electron	$< 1MeV$	$Z^2 - Z^3$	Coherent
Compton Scattering	Quasi free electron	$\sim 1MeV$	Z	Incoherent
	Nucleon	$> 100MeV$		Incoherent
Pair Production	in nuclei field	$> 1.022MeV$	Z^2	
	in electron field	$> 2.044MeV$	Z	
Photonuclear effect	Nuclei	$> 10MeV$		Absorbed photon and particle emission

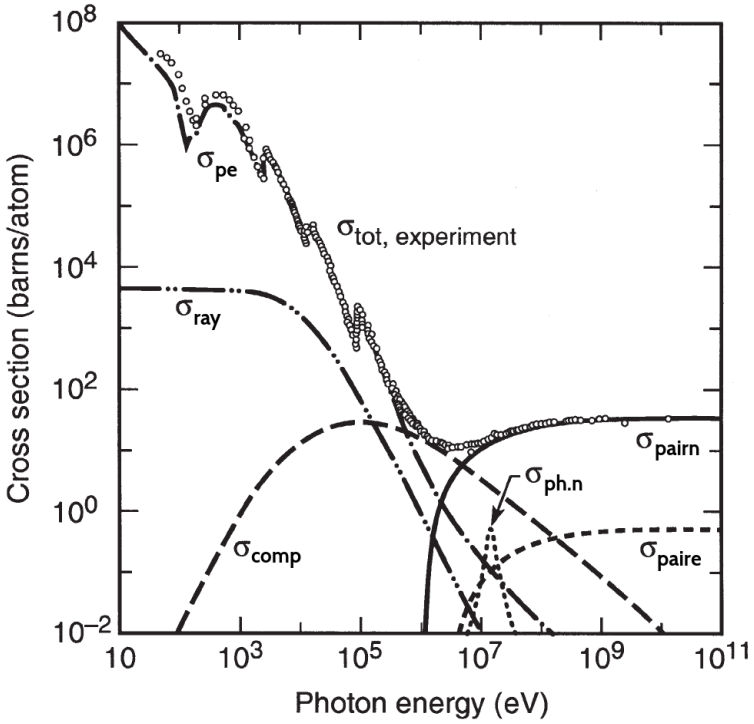

Figure 2.7: The different processes contributions to the total cross section as a function of energy [21]. The photo electric effect dominates in the lowest energies, pair production starts at $\sim$1.022 MeV and is the dominating process for higher energies. Compton scattering reaches its maximum around 1 MeV, but is present for a relatively wide range of intermediate energies.

2.2.1 Photoelectric Effect

The incident photon transfer all its energy to a bound orbital electron and if the energy of the photon is higher than the binding energy of the electron, then the electron, referred to as a *photo electron*, is ejected with the kinetic energy,

$$E_{kin} = E_\gamma - E_{binding} \quad . \tag{2.2.4}$$

This process is illustrated in figure 2.8.

The cross section of photoelectric effect is roughly proportional to $Z^5/E_\gamma^{3.5}$, and so it increases rapidly with the Z of the absorber material, but decreases with increasing photon energy [14]. This is witnessed in figure 2.7 by the declining cross section for increasing photon energies, but with the presence of characteristic *absorption peaks* as the photon energy reaches the binding energy of electrons in the deeper shells (K,L,M shells illustrated in figure 2.8) causing the cross section to increase. Photoelectric effect occurs primarily with K-shell electrons and when the vacancy is filled by an electron from the upper energy shell, a characteristic x-ray is emitted [20]. It is of note that at energies where photoelectric effect is the main process, the energy deposited by the photo electron is considered to be absorbed locally due to its short range [5].

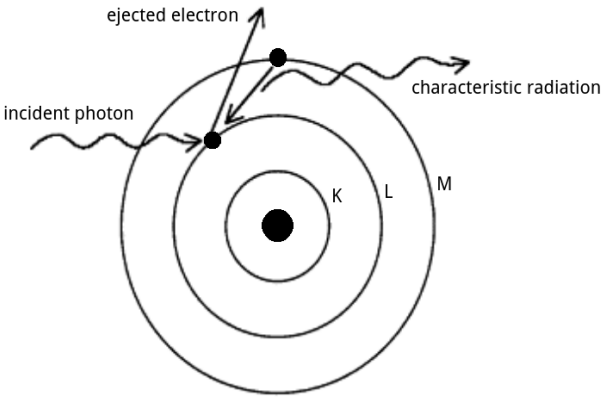

Figure 2.8: Illustration of Photoelectric Effect. An incoming photon is absorbed by an orbital electron which in turn is ejected and a outer laying electron fills the vacancy while emitting characteristic radiation [22].

2.2.2 Compton Scattering

As illustrated in figure 2.9, an incoming photon with energy $E_\gamma = hv$ transfers a fraction of its energy to a loosely bound (or free) orbital electron via an inelastic collision and is deflected from its incident direction while carrying the reduced energy

$$E_\gamma^{'} = hv^{'} = \frac{hv}{1+\epsilon(1-\cos\theta)}\,, \tag{2.2.5}$$

where $\epsilon = hv/m_e c^2$ and θ is the scattering angle of the photon. The scattered photon, from having lost only a portion of its energy, may undergo further photoelectric or Compton interactions as it continues to travel through matter.

The ejected electron receives the energy

$$E_e = E_\gamma - E_\gamma^{'} = hv\frac{\epsilon(1-\cos\theta_)}{1+\epsilon(1-\cos\theta)}\,, \tag{2.2.6}$$

and may cause further excitations and ionizations in its continued path [20, 22]. The additional scattering angle relations from applying energy and momentum conservations are [2]:

$$\cos\theta = 1 - \frac{2}{(1+\epsilon)^2\tan^2\phi + 1}\,, \tag{2.2.7}$$

$$\cot\phi = (1+\epsilon)\tan\frac{\theta}{2}\,, \tag{2.2.8}$$

From equation 2.2.6 and considering a photon making a direct hit on the electron and thus scatter backwards at $\theta = 180^\circ$, while the electron is ejected in the forward direction at $\phi = 0^\circ$, this maximum energy transfer is,

$$E_{e,max} = hv\frac{2\epsilon}{1+2\epsilon}\,, \tag{2.2.9}$$

also known as the *Compton Edge* [2]. From this maximum energy transfer equation 2.2.9 it is evident that Compton scattering causes a larger energy deposition in matter when involving higher photon energies than it does for lower energies[23]. It is also of note that Compton scattering have little dependence on the Z of the material, but rather on the electron density (electrons per cm^3), this is because the electrons in Compton scattering are considered to essentially be free.

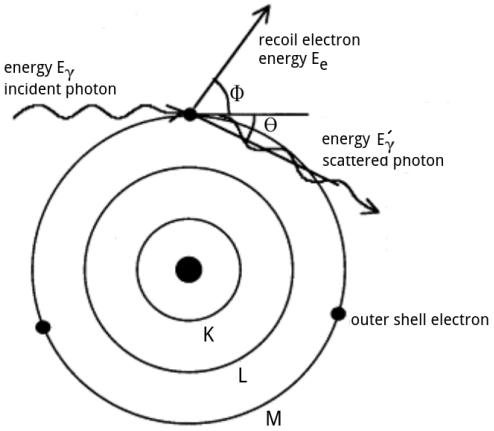

Figure 2.9: Illustration of Compton Scattering [22, p.7].

2.2.3 Pair Production

Photons with energies above $1.022MeV$, twice the electrons rest mass, can interact with the nucleus directly and produce a electron-positron pair. The positron undergoes annihilation with a free electron and creates two $511KeV$ *annihilation photons* as illustrated in figure 2.10. Pair production varies almost linearly with Z^2 of the absorber, and is the dominant interaction process at energies $> 10MeV$ where it accounts for almost all γ-ray absorptions in all Z absorbers [**?**].

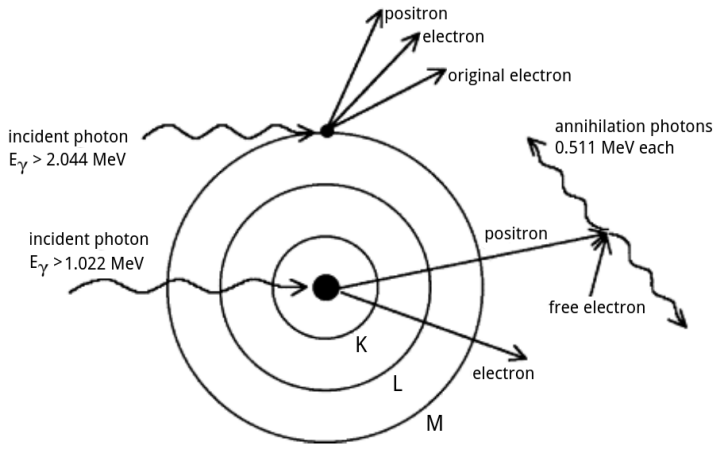

Figure 2.10: Illustration of Pair Production. An incoming photon with an energy larger than $1.022MeV$ is transformed into an electron positron pair [22].

2.3 Interactions of Neutrons with Matter

Neutrons, from not having an electric charge, are not subjected to any Coulomb interactions. Instead, neutrons interact with the nucleus of an atom mainly through the strong force, which makes them very penetrating particles due to the short range of this force. In an absorber, neutrons interact by elastic scattering, inelastic scattering, *neutron capture* and nuclear reactions, and similarly to photons they attenuate exponentially in matter and are categorized as indirectly ionizing radiation [3].

Neutron interactions have a strong energy dependence, as inelastic scattering where the neutron is absorbed by the nucleus and re-emitted with a lower energy and different direction, can only occur when the neutron has sufficient energy, in the order of $1MeV$ and above, to excite the nucleus. Below this threshold there is elastic scattering, where the recoiled nucleus is given a fraction of the neutrons kinetic energy through momentum and energy conservation laws. In nuclear reactions and neutron capture, the reaction cross sections are proportional to $1/v$, where v is the velocity of the neutron, making absorption more likely at low energies. From these energy dependences, neutrons are classified according to their energies, *high energy neutrons* are above $\approx 100MeV$, *fast neutrons* are between a few ten's of MeV and a few hundred keV. Between $\approx 100keV$ and $0.1eV$ neutrons are called *epithermal*, at energies $\approx 1/40eV$ they are known as *thermal* neutrons, and at energies of $meV - \mu eV$ they are *cold* or *ultra-cold* [2].

The probability for a neutron interaction is given by the sum of cross sections,

$$\sigma_{tot} = \sigma_{elastic} + \sigma_{inelastic} + \sigma_{capture} + ... \tag{2.3.1}$$

In practice it is necessary to rely on tables and databases of neutron cross sections for nuclei of interest as there are no convenient way to calculate them [24, 25]. Neutron cross sections for some light elements versus incident neutron energy are plotted in figure 2.11 by using such a database.

If the target nucleus and captured neutron form a compound nucleus, and the energy contribution from the neutron is close to an excited state of the compund nucleus, resonance peaks where neutron reactions are enhanced occur. For lighter nuclei these resonances only occur in the MeV region, while for heavier nuclei they can appear at neutron energies down in the eV region [24].

2.3.1 Moderation

Moderation is the process of slowing down fast neutrons, when fast neutrons enter matter they will scatter both elastically and inelastically on nuclei, losing energy until reaching a thermal equilibrium with the surrounding atoms where it is either absorbed or undergoes an nuclear reaction. Important factors in a moderator are the probability of scattering and the change in kinetic energy of the neutron after an interaction. The maximum energy an neutron with kinetic energy E_n can transfer to a nucleus with atomic weight A in a single head-on elastic

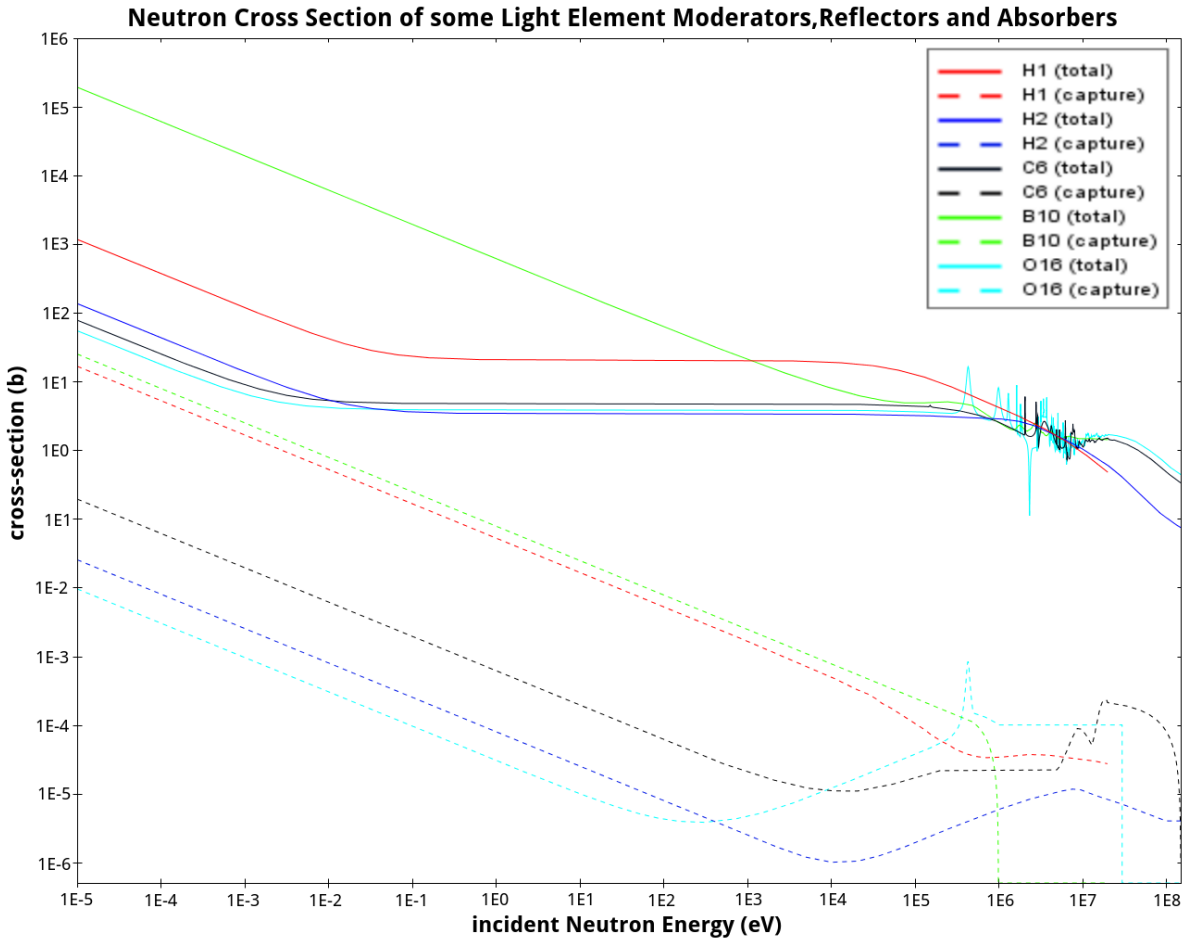

Figure 2.11: Using the JANIS software [26] and database ENDF/B-VII.1 [25], the total (full lines) and absorption (dotted lines) cross sections for some light elements versus incident neutron energy were plotted.

collision is

$$E_{max} = \frac{4AE_n}{(1+A)^2}\,, \tag{2.3.2}$$

this implies that lighter nuclei absorb more recoil energy and are thus more efficient at slowing down neutrons than heavier nuclei [4]. In general, after n elastic collisions, the neutron's energy is expected to change to

$$E_n = E_0[\frac{A^2+1}{(A+1)^2}]^n\,. \tag{2.3.3}$$

By looking at the logarithmic change in energy, the number of collisions needed to reduce the initial energy, E_0, of a neutron down to a certain level E_n can be calculated [24],

$$n = \frac{\log(\frac{E_n}{E_0})}{\log[\frac{A^2+1}{(A+1)^2}]}\,. \tag{2.3.4}$$

Some examples illustrating equation 2.3.4 are collected in table 2.3.

Element	Atomic weight, A	Number of Collisions, n
Hydrogen	1	27
Deuterium	2	31
Helium	4	48
Beryllium	9	92
Carbon	12	119

Table 2.3: Average number of collisions, n, needed to reduce a neutron's energy from $2MeV$ to $0.025eV$ by elastic scattering.

2.3.2 Neutron Reactions

Some neutron reactions of interest in neutron dose deposition and radiation protection [4]:

$$^1_0\mathrm{n} + {}^1_1\mathrm{H} \rightarrow {}^2_1\mathrm{H} + {}^0_0\gamma \tag{2.3.5}$$

Absorption of thermal neutrons by hydrogen is followed by the emission of a gamma photon with energy $Q = 2.22MeV$ representing the binding energy of the deuteron (calculated by the *Q-value*, which expresses the total energy released in a reaction by comparing the total masses on both sides of the arrow [5]).

$$^1_0\mathrm{n} + {}^{10}_5\mathrm{B} \rightarrow {}^7_3\mathrm{Li} + {}^4_2\alpha \tag{2.3.6}$$

Boron has a large cross section concerning neutron absorption and is therefore used as a neutron shielding material. Depending on what state ^7Li is left in, the recoiled ^7Li nucleus and alpha particle will share $Q = 2.31MeV$ in 96% of the reactions and $Q = 2.79$ in the other 4%. If the ^7Li is left in an excited state, as it does for 96% of the reactions, it will emit a $0.48MeV$

gamma ray.

$$^{1}_{0}\mathrm{n} + ^{14}_{7}\mathrm{N} \rightarrow ^{14}_{6}\mathrm{C} + ^{0}_{1}\mathrm{p} \tag{2.3.7}$$

Nitrogen is abundant in tissue and together with hydrogen are the only two capture interactions that delivers a significant thermal neutron dose to tissue. The Q-value is $0.626 MeV$ and the resulting proton and ^{14}C nucleus are deposited locally due to their short range.

$$^{1}_{0}\mathrm{n} + ^{113}_{48}\mathrm{Cd} \rightarrow ^{114}_{48}\mathrm{Cd} + ^{0}_{0}\gamma \tag{2.3.8}$$

Cadmium is used as a neutron shield and has a large, $21000 - barn$, capture cross section concerning thermal neutrons up to $\approx 0.2eV$ and absorbs essentially all neutrons below the cadmium cut-off $\approx 0.4eV$. The emitted gamma from this reaction has an energy of $0.56MeV$ [27].

Chapter 3

Radiation Biology

From a human health perspective the most significant aspect of radiation interactions with matter is the deposition of energy in biological tissue and the development of health effects caused by ionization events inside cells. Damage to tissue can be caused by direct breaking of biological molecules (DNA), or indirectly through the production of *free radicals*.

With the inclusion of radiation biology, *dosimetry* aims to quantify the relationship between deposited energy, referred to as *dose*, and biological effect. To this extent, certain *dosimetric quantities* are defined by the *ICRP* and *ICRU*, these quantities have been modified several times and are still evolving as there is not enough systematic data available to fully describe dose-response relationships, but it is generally agreed upon that the severity of induced damage increases with dose. Radiation therapy takes advantage of this by aiming to deposit a high enough dose to a tumour volume in order to incapacitate cancer cells.

3.1 Dosimetry

Dosimetry relates specific measurements in a radiation field to physical, chemical or biological changes in a target. These changes are quantified as a function of the amount of radiation received and are used to assess radiation exposure in humans and to describe dose-response relationships. Dosimetry is based on measurements of ionization and energy absorption in matter, usually through the measurement of *absorbed dose*, and is essential in the surveillance of a radiation environment and to determine dosimetric quantities like *equivalent dose* and *effective dose* that are used to quantify changes in different biological tissue caused by different types of radiation. These quantities are in turn applied in radiation protection to specify dose limits that ensure acceptable safety in radiation environments [4, 28].

3.1.1 Absorbed Dose

The primary quantity used in dosimetry is the absorbed dose, often referred to as dose, D, which is measured in *Gray* [Gy], where $1Gy = 1J/kg$ and describes the amount of energy dE

deposited per unit mass dm for all types of ionizing radiation in any irradiated target [4],

$$D = \frac{dE}{dm} . \tag{3.1.1}$$

This definition is suitable for use in *micro dosimetry* for describing localised doses in an infinitesimal mass element. Measurements of the absorbed dose however, do not provide sufficient information about the type and energy of the radiation, nor about the tissue where the energy is absorbed, the biological effects of the absorbed dose are therefore unpredictable. To better predict these effects, two dose terms "equivalent dose" and "effective dose" are defined by multiplying the absorbed dose with dimensionless weighting factors w_R and w_T [29].

Instead of the point function D, radiation protection usually make use of the average absorbed dose, D_T, in a tissue or organ with mass, m_T [5],

$$D_T = \frac{E}{m_T} . \tag{3.1.2}$$

It is noted that this average dose approach assumes an uniform dose distribution, while in practice, radiation effects are dependent on the distribution and may therefore make dose-response relationships difficult to evaluate.

3.1.2 Equivalent Dose

Equivalent dose H_T describes the biological effectiveness that certain types of radiation and their energies, denoted R, have on a specified tissue or organ T, and is the sum over all types of radiations involved.

$$H_T = \sum_R w_R D_{T,R} , \tag{3.1.3}$$

where w_R is the *radiation weighting factor* that converts the average absorbed dose $D_{T,R}$ to equivalent dose. The values of w_R are defined to reflect the *relative biological effectiveness* (RBE) of different types of radiations and energies.

$$w_R \cong \frac{1}{D} \int_0^\infty Q(L_\infty) D(L_\infty) dL_\infty , \tag{3.1.4}$$

where L_∞ is the *unrestricted linear energy transfer* of the radiation in water , Q is the quality factor as a function of L_∞, and $D(L_\infty)dL_\infty$ is the absorbed dose between L_∞ and $L_\infty + dL_\infty$ [30]. Table 3.1 lists the 1990 recommended Q-factors and table 3.2 lists the current radiation weighting factors from the 2007 ICRP recommendations for different types of radiations. Equivalent dose has the same basic units as absorbed dose, but to emphasize the change from a physical quantity to a biological response, it is referred to as *Sievert* [Sv] [29].

3.1.3 Effective Dose

All dose limits in radiation protection are given in terms of effective dose and reflects the biological effect of the average absorbed dose by considering the sensitivity that different tissue types have to radiation. By introducing the *tissue weighting factor*, w_T, which is normalized to unity of the full body, defines the effective dose H_E as [29],

$$H_E = \sum_T w_T H_T = \sum_T \sum_R w_T w_R D_{T,R} \, . \tag{3.1.5}$$

Like equivalent dose, effective dose is measured in Sievert. The latest tissue weighting factors recommended by the ICRP, listed in table 3.3, are based on stochastic effects like induced cancer and heritable diseases rather than on mortality. It is also noted that the w_T values are for use in radiological protection and based on a reference population, so they "should not be used to obtain estimates of potential health effects for a given individual" [29] [4].

Table 3.1: Quality Factor Q as a function of L_∞ in water [30].

$L_\infty[keV/\mu m]$	Q
< 10	1
$10 - 100$	$0.32L_\infty - 2.2$
> 100	$300/\sqrt{L_\infty}$

Table 3.2: Radiation weighting factors recommended by the ICRP in 2007 [28].

Radiation type	**Radiation weighting factor (w_R) - 2007 recommendations**
Photons	1
Electrons and muons	1
Neutrons, energy $< 1MeV$	$2.5 + 18.2e^{-[ln(E)]^2/6}$
$1 - 50MeV$	$5.0 + 17.0e^{-[ln(2E)]^2/6}$
$> 50MeV$	$2.5 + 3.25e^{-[ln(0.04E)]^2/6}$
Protons and charged pions	2
Alpha particles, heavy nuclei fission fragments	20

Table 3.3: Tissue weighting factors for different tissues as recommended by the ICRP in 2007 [28]

Tissue/Organ	**Tissue weighting factor(w_T) - 2007 recommendations**
Gonads	0.08
Bone marrow (red)	0.12
Colon	0.12
Lung	0.12
Stomach	0.12
Breast	0.12
Bladder	0.04
Esophagus	0.04
Liver	0.04
Thyroid	0.04
Skin	0.01
Bone surface	0.01
Salivary glands	0.01
Brain	0.01
Remaining tissues and organs	0.12

3.2 Biological Effects of Radiation

Ionising radiation damages living cells by breaking DNA strands and by producing free radicals that attack chemical bonds inside cells. Induced health effects depend on the type of incident radiation and rate of energy deposition along the ionizing particle's path, these quantities are summarized in the term *linear energy transfer* (LET), where higher LET particles will cause more biological damage than lower LET particles.

A damaged cell will usually repair itself with no visible effect, but if the damage is severe enough, a cell will either: i) die, ii) have its natural function impaired (leading to cancer) or iii) experience a permanent genetic alteration [2].

3.2.1 LET - Linear Energy Transfer

LET has units $keV/\mu m$ and is defined as the amount of energy deposited per unit radiation track length in matter. This is closely related to the stopping power 2.1.1, but does not include energy that escapes the defined area in the form of photons or energetic electrons, making LET$\leq$ $|-dE/dx|$. In order to exclude the energy absorbed outside the area of interest, an alternate definition of LET that disregards all secondary electrons with kinetic energies above a limit, Δ, is defined [5],

$$L_\Delta = (-\frac{dE}{dx})_\Delta \, . \tag{3.2.1}$$

L_∞ is then read as the unrestricted linear energy transfer where LET is calculated with all energies, making it equal to the stopping power. Only differentiating itself from the stopping power due to bremsstrahlung photons carrying some energy away [5].

LET basically indicates the quality of different types of radiation. Particles with high LET, including neutrons and heavy charged particles, will ionize and excite more molecules in their paths and thus causes greater biological damage per absorbed dose in tissue than low LET particles like photons. It is noted that LET varies as the particle slows down and deposits more of its energy in matter [31].

3.2.2 RBE - Relative Biological Effect

Biological damage caused by radiation is strongly correlated with the radiation type and its properties. This can be contrasted as a ratio between the dose, D needed to produce a specific biological effect and the X-ray dose, D_X that is needed to produce the same effect under the same conditions.

$$RBE = \frac{D_X}{D} \, . \tag{3.2.2}$$

RBE is not a constant however, and depends on various properties like LET, dose rate and dose fractionation, as well as the measured biological effect. Generally, RBE increases with LET up to a point, as seen in figure 3.1 which illustrates RBE as a function of LET when concerning cell death. Starting at low LET and as the density of ionizations and excitations increases with

higher LET, so does the biological effect until it reaches an optimum around $100 keV/\mu m$. Any further increase in LET result in more energy deposition than what is needed to kill a cell (overkill) [4].

In radiation protection, RBE only appears in the derived quantities, $Q(L_\infty)$ and radiation weighting factor, w_R [32].

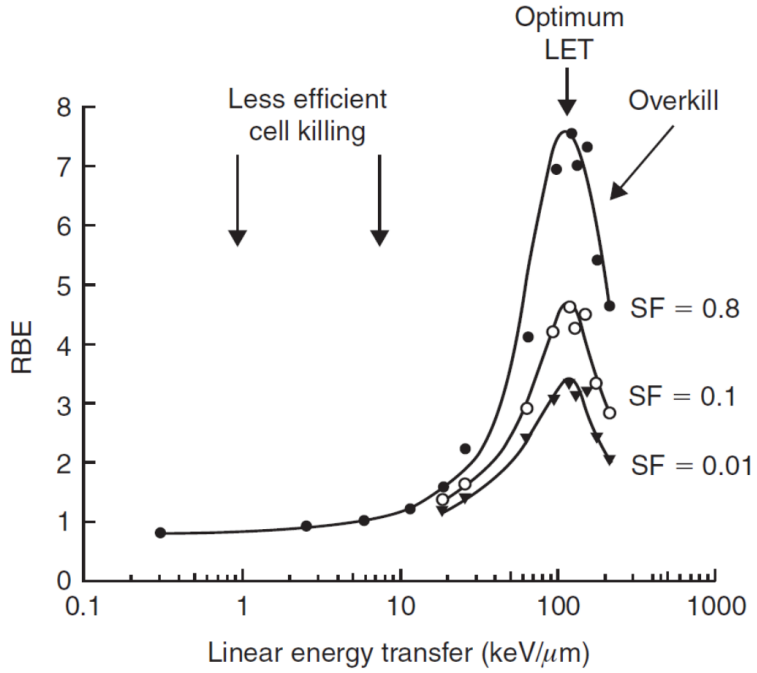

Figure 3.1: Illustrating the relative biological effect's dependence on linear energy transfer (as cited in [22]). SF is and abbreviation of survival fraction

3.3 Health Consequences from Irradiation

Molecular changes in biological tissue can manifest itself as radiation damage and cause both short-term and long-term health effects. High doses cause acute damage to tissue and organs due to cell killing and result in observable short term *deterministic effects*. At low doses tissue reactions are not observed, but future *stochastic effects* from damaged genetic material may occur in the long term and are assumed to increase with dose.

3.3.1 Short term effects

At high doses above a threshold dose, deterministic effects and acute tissue reactions are observable. Among tissue reactions, loss of the reproductive capacity of cells and cell death play a central role in the development of tissue damage. Some of the more radio-sensitive tissues and organs consists therefore of cell systems that divide rapidly. Late tissue reactions may also appear if there is damage to blood vessels or tissues that are important for organ functions, these reactions can appear months or years after radiation. All deterministic effects exhibit a

threshold characteristic, an effect has therefore a certain probability of occurrence above this.

As radiation weighting factors are derived from stochastic effects at low doses, the equivalent dose and effective dose should not be used in quantifying radiation doses or determining treatment in situations where tissue reactions are caused by high doses. Absorbed dose or dose equivalent should instead be used in such instances [28].

3.3.2 Long term effects

In the low dose range, stochastic effects such as induced cancer or heritable diseases may appear. As concluded by the UNSCEAR (cited in ICRP Report 103 [28]), the general assumption concerning the risk of stochastic effects is that it increases linearly, with no threshold, in the low dose range and that it does not depend on the dose rate, but on the total accumulated dose. There is however insufficient data available in the range below $0.5 - 1Gy$ to determine any dose-response relationships or basis for dose limits. The risk of stochastic effects depends only on the effective dose as there are notable differences between different types of tissues and organs when it comes to the sensitivity of radiation inducing stochastic effects, as are reflected in the w_T values in table 3.3 [28].

Chapter 4

Particle Therapy

Using protons and heavy charged particles in medical treatment, given their characteristic depth dose distribution enabling a relatively precise dose delivery to a target volume while simultaneously sparing and reducing deposited dose to surrounding healthy tissue and organs, was first proposed by the American physicist Robert R. Wilson in 1946 [33]. Since then, over 137 000 patients have been treated with particle therapy and in 2014 there were 48 particle therapy facilities in clinical operation around the world and treated approximately 15 000 patients, of which 86% were treated with protons and 14% with carbon ions and other particles [34].

4.1 Radiation Treatment with Charged Particles

The basic goal of radiation therapy is to kill tumour cells while simultaneously minimizing damage to healthy tissue, ideally this would be achieved by delivering a prescribed dose to a tumour while maintaining zero dose to normal tissue. Unfortunately, due to the intrinsic properties of the depth dose distribution will an increased tumour dose also increase normal tissue dose. This is reflected in the *therapeutic ratio* that assesses the radiation treatment quality as a ratio between *tumour control probability* (TCP) and *normal tissue complication probability* (NTCP). The therapeutic ratio, also referred to as the *therapeutic window*, is illustrated in figure 4.1. The choice of treatment plan and dose delivery technique aims to widen this window by achieving good TCP while simultaneously keeping the NTCP low [35]. Hadron therapy accomplishes this with its depth dose distribution characterized by a small entrance dose and distinct Bragg Peak followed by a sharp distal fall-off near the particles range. The small lateral beam spread and enhanced biological effectiveness, especially of heavier charged particles, further improves the therapeutic ratio. There are however several considerations and factors involved when choosing what type of particle to use in hadron therapy [11].

Ions heavier than protons show an improved dose conformity due to their larger mass and close to negligible straggling effects and consequently offer better sparing of normal tissue close to the target. Heavy ions also exhibit an increased LET in the Bragg peak and this allows for a high LET region to be conformed to the tumour, increasing the RBE characteristic that allow for an improved TCP. As seen in figure 4.2, Carbon has an excellent RBE ratio (Bragg

peak vs. entrance region) compared to protons and helium. Ions heavier than neon however show a higher RBE in the entrance region than in the Bragg Peak, consequently increasing the NTCP.

Heavy ions also have the disadvantage of fragmenting into light clusters and neutrons that give rise to a fragmentation tail beyond the Bragg peak which increases the NTCP. There is also the aspect of accelerating particles to energies that are required to treat deep-seated tumours: a proton beam of ≈ 146 MeV can penetrate about 15 cm in water, while a carbon ion requires over 3200 MeV (or about 270 MeV/u) to achieve the same depth. In order to accelerate particles to such energies, a synchrotron is the most suited and this is a much more complicated and cost intensive as opposed to a cyclotron which is widely used in proton particle therapy [36].

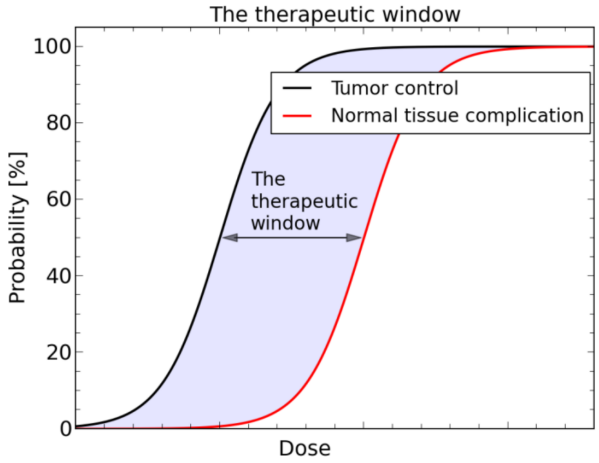

Figure 4.1: Two sigmoid shaped dose-response curves illustrating the TCP and NTCP and the gap between showing the therapeutic window [37]

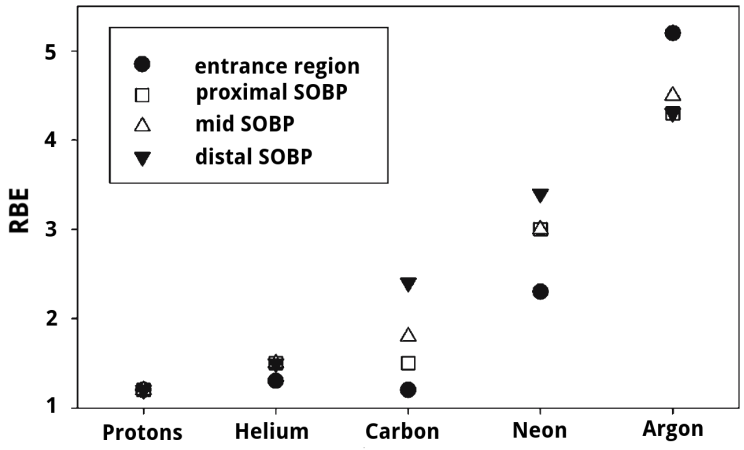

Figure 4.2: The RBE of different ions in different positions of a SOBP with modulation depth 8-10cm. Initial beam energy was 160, 225, 400, 557 and 570 MeV/u for protons, helium, carbon, neon and argon ions respectively [36].

4.2 Spread Out Bragg Peak - Energy Modulation

A mono energetic beam from an accelerator will only form a pristine Bragg peak in matter, so in order to cover a target volume longitudinally, multiple Bragg Peaks of different ranges and intensities are superimposed to form a *Spread Out Bragg Peak* (SOBP). Each Bragg peak is further weighted by delivering a relative number of ions for each peak to achieve a flat dose plateau [15]. This principle is illustrated in figure 4.3. To create multiple Bragg peaks and shape the beam to a target volume in the clinic, two different methods are applicable, *passive beam shaping* and *active beam shaping*[36].

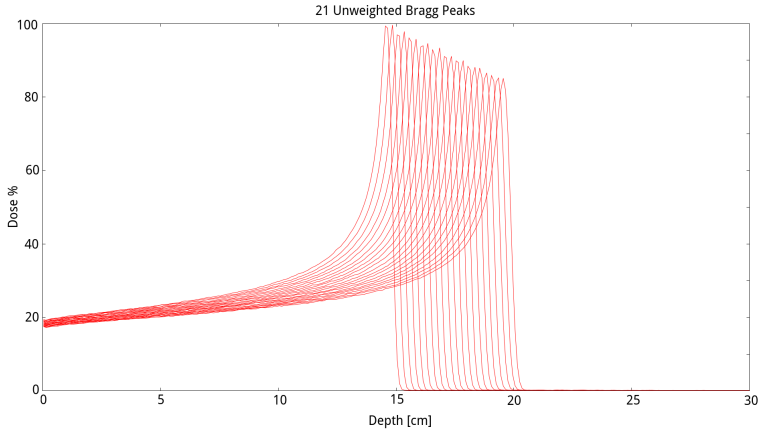

(a) Longitudinal depth dose plot of 21 unweighed proton beams with energies from 145 MeV to 172 MeV.

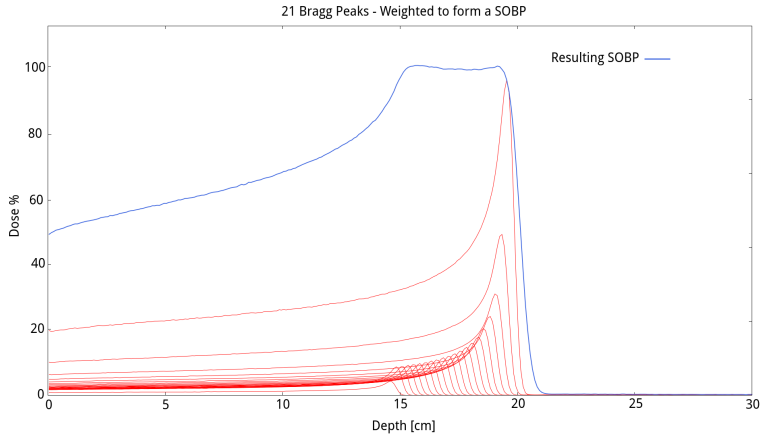

(b) The longitudinal depth dose plots of the 21 proton beams are weighted and added together to form a SOBP with a flat dose plateau covering the 15-20 cm range.

Figure 4.3: FLUKA Monte Carlo simulations. Illustration of the principle behind the formation of a SOBP. Beams of several consecutive energies are added together and weighted to obtain a flat dose plateau that covers a desired depth.

Passive beam shaping modulates the mono energetic beam from the accelerator by introducing a degrader (either a range modulator wheel with varying thickness or a ridge filter) into the beam line. Then, in order to move the resulting SOBP to a certain depth, an additional

range shifter consisting of homogeneous plastic plates of various thicknesses are introduced into the beam line. The last step in passive beam shaping is to spread the beam laterally and homogeneously over the target volume either by scattering or by a magnetic wobbling system. Patient specific collimators and compensators are also used to shape the field to fit the structure (tumour) in the treatment volume [36]. This technique has three major disadvantages: 1.) The depth dose profile can only be tailored to the distal end of the target. 2.) Presence of material in the beam line lead to nuclear fragments that increase the NTCP in the entrance region. 3.) Large number of patient-specific beam modifiers must be manufactured.

Active beam shaping takes advantage of the particles electric charge to produce a pencil beam that is deflected laterally by two magnetic dipoles, allowing for *scanning* of the beam over a treatment volume. By using a modulator wheel, or a synchrotron that allows for adjustments of the output energy pulse by pulse, the target volume can be covered in the longitudinal direction while simultaneously scanning all three dimensions and fitting the dose distribution to both the proximal and distal end of the target. This is mostly done without introducing extraneous material into the beam line such as range shifters and compensators. This reduces the production of nuclear fragments and thus decreases the NTCP [36]. Figure 4.4 illustrates the principle and difference between an active and passive beam delivery system.

4.3 Fractionation

A typical radiation treatment is split into fractions depending on the diagnosis and treatment type, for instance can a prescribed dose of 50 Gy commonly be fractionated into a standard scheme of 2 Gy/fraction to be delivered in 5 days/week. This is done in order for healthy tissue to repair itself and decrease the NTCP. Heavier ions such as carbon with their higher RBE can invoke a better TCP and thus deliver a prescribed dose in fewer fractions (*hypofractionation*) which reduces treatment time and cost while still maintaining TCP and NTCP without an increase in side effects. Such alternative fractionation schedules are undergoing continuous investigations, clinical trials and studies [15].

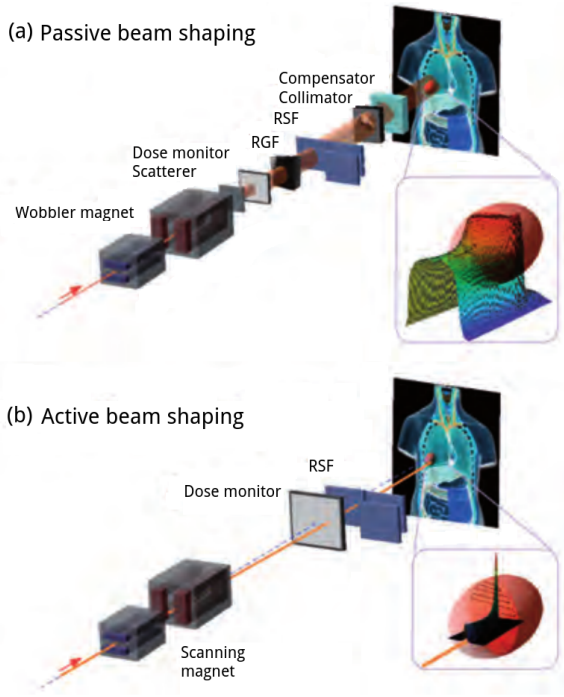

Figure 4.4: (a) Illustrates passive beam shaping with a wobbling magnet, ridge filter(RGF), range shift filter(RSF) and the inclusion of a collimator and compensator. (b) Illustrates the active beam shaping method by scanning a pencil beam in both vertical and horizontal direction with scanning magnets. A synchrotron can also adapt the scanned area to certain depth without introducing a range shift filter into the beam line [**?**].

Chapter 5

Radiation Protection

Radiation occurs naturally in nature and has a constant presence in peoples everyday life through what is dubbed *natural background radiation*. This consists of external exposures from cosmic radiation, and terrestrial radiation caused by the decay of natural radionuclide in the ground, as well as internal exposures caused by the inhalation and ingestion of radionuclide found naturally in air, water and food. Worldwide, the average dose to the human body from naturally occurring radiation accounts to about 2.4 mSv per year [38].

Any additional dose contributions come from artificial radiation sources such as medicine (medical imaging and radiotherapy), occupational hazards in the work environment, or caused by accidental radiation exposure. There is no general consensus on exposure limits, but planned radiation exposures follow the *ALARP* ("As Low As Reasonably Practicable") principle that attempts to declare a common practice centred around risk management that balances risk and societal benefits. Averaged over the world, artificial radiation sources contribute with an additional 0.61 mSv to the annual dose, with over 95% of this coming from medicine. However, with the increasing availability of modern medical imaging and radiotherapy, the annual average dose contribution can reach the same level as the natural dose, as seen in the United States where the average dose contribution from medicine is about 3.0 mSv [39].

With an emphasis on radiotherapy in medicine, this chapter will go deeper into the rationale behind radiation protection and the physical aspects of limiting exposure to the human body through shielding applications.

5.0.1 Radiation Protection Recommendations and Guidelines

Several international and national agencies have been established with the intent of supervising, consulting and researching radiation effects and radiation protection in order to adopt routines, recommendations and technology that improves the security and safety of workers and the general public at large. Some of these agencies includes the IAEA who create safety standards that incorporates information on health effects of radiation provided by the UNSCEAR and also apply recommendations concerning radiation protection and radiation levels made by the ICRP, whom in turn also takes the scientific information provided by the UNSCEAR into their recommendations [35]. Many countries have their own competent authority on ra-

diation protection and nuclear safety that supervise and manage the use of radiation sources in medicine and research on a national level, in Norway this authority is "Statens Strålevern" (NRPA) [**?**].

In 2007 the ICRP issued a revision of their 1991 recommendations by taking new biological and physical information into account while simultaneously improving and streamlining the presentation of their recommendations. This revision culminated in *Publication 103* [**?**] which updated radiation and tissue weighting factors, maintained individual dose limits and reinforced the principle of optimisation of radiation protection. These recommendations provide a consistent basis for national and regional regulation standards and will be discussed further in this section.

The ICRP base their recommendations on the assumption that doses below 100 mSv follow the Linear-Non-Threshold (LNT) dose-response model in accord with that given by the UNSCEAR [28, 40]. Based on the implication made by the LNT model, that there is always a finite risk involved in radiation, ICRP conceived three fundamental principles of any radiological protection system [28]:

- **Justification**: "Any decision that alters the radiation exposure situation do more good than harm."
- **Optimisation of protection**: "The likelihood of incurring exposures, the number of people exposed, and the magnitude of their individual doses should all be kept as low as reasonably achievable, taking into account economic and societal factors."
- **Application of dose limits**: "The total dose to any individual from regulated sources in planned exposure situations other than medical exposure of patients should not exceed the appropriate limits recommended by the Commission."

While the recommendations in ICRP Report 103 are applied to all sources and exposed individuals, they are differentiated by three types of exposure situations that take different circumstances into account: i) *Planned exposure situations* where radiation sources are deliberately introduced and operated. ii) *Emergency exposure situations* that may occur as a result of an incident in a planned or unexpected situation. iii) *Existing exposure situations* where exposure already exist and must be regarded. Another three exposure categories are further addressed in order to distinguish between different exposure types in a given situation: 1) *Occupational exposure*, radiation exposure to workers as a result of situation that is under the responsibility of an operating management. 2) *Medical exposure of patients* that occur in diagnostic, interventional and therapeutic procedures. 3) *Public exposure* that considers all exposures to the public other than occupational and medical exposures.

Together with the principle of protection optimisation, three concepts of dose restrictions; *dose limit*, *dose constraint* and *reference level* are defined and applied in their respective situations in order to reduce the dose to a "as low as reasonable level". Table 5.1 lists the dose restrictions applied in relation to the exposure situation and category, and figure 5.1 illustrates the contrast between the different dose restrictions for occupational and public exposure. This thesis will

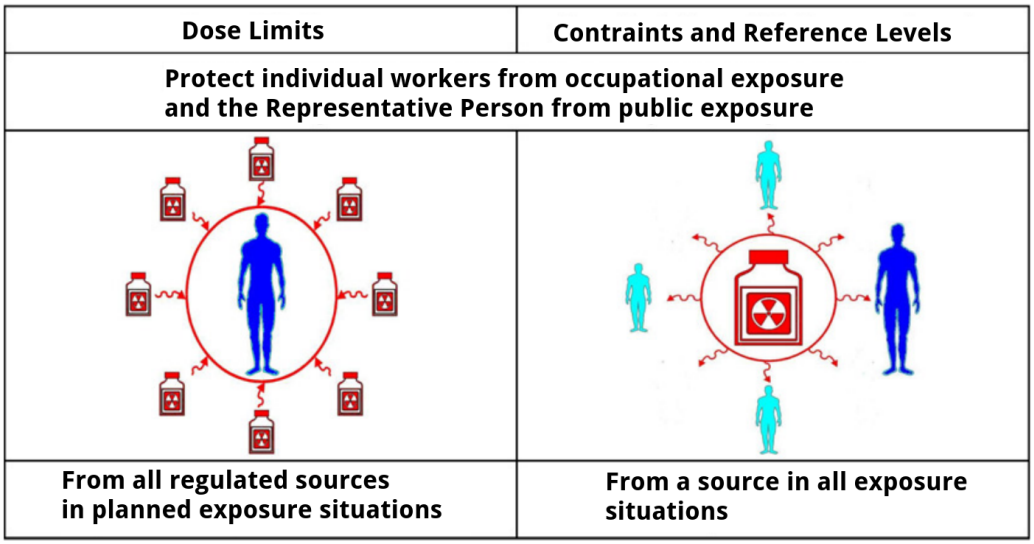

Figure 5.1: Illustration of the contrast between dose limits, dose constraints and reference levels for workers and the general public [28]

not go into detail of the framework around dose constraints and reference levels, but the reader is referred to page 97 in the ICRP Report 103 [28].

Table 5.1: The ICRP's dose restrictions shown in relations to the exposure situation [28, p.94].

Type of Situation	**Occupational exposure**	**Public exposure**	**Medical exposure**
Planned exposure	Dose limit	Dose limit	Diagnostic reference
	Dose constraint	Dose constraint	level (Dose constraint)
Emergency exposure	Reference level	Reference level	N.A.
Existing exposure	N.A.	Reference level	N.A.

Dose Limits

The updated weighting factors recommended by the ICRP as seen in table 3.2 and 3.3 in chapter 3 are used to specify the dose limits that ensure that health effects are kept below unacceptable levels. Re-evaluation of available data based on a broad range of RBE values updated the previous 1991 recommendations for neutrons (from 5-20 to a function of neutron energy) and protons (from 5 to 2), but maintained the w_R values for photons and heavy ions. In a planned occupational exposure situation it is recommended that the limit, expressed as effective dose, should be 20 mSv per year averaged over defined 5 year periods (100 mSv in 5 years), and with an additional condition that the effective dose should not exceed 50 mSv in any single year. Table 5.2 lists the recommended dose limits for workers and the public in a planned exposure situation.

Table 5.2: ICRP's recommended dose limits in a planned occupational and public exposure situation [28].

Type of limit	Occupational	Public
Effective dose	20 mSv per year, averaged over periods of 5 years	1 mSv in a year
Annual equivalent dose in:		
Lens of the eye	150 mSv	15 mSv
Skin	500 mSv	50mSv
Hand and feet	500mSv	-

5.0.2 Radiation Environment in Radiotherapy

All radiation in a radiotherapy treatment room, except for the primary beam, is comprised of secondary radiation produced at locations where beam loss and scattering occurs, this takes place during beam propagation in matter (patient and shielding) and in beam line devices. Secondary radiation particles that arise due to hadronic cascades, as described in chapter 2, section 2.1.7, are mainly comprised of neutrons, photons, protons, and fragmentation fragments with energies up to the incident primary beam energy. The distribution of secondary neutrons for protons, helium and carbon ion beams are very different however as fragmentation only occurs for particles heavier than protons. The resulting projectile fragment from fragmentation will emit high energy and forward peaked neutrons that are added to the isotropic neutron distribution from target fragments, as opposed to protons where there are no projectile fragments present [**?**]. Photon radiation produced by inelastic neutron scattering and neutron absorption in matter also plays a role in the radiation environment, especially in thick shielding where the higher density of neutron reactions emit photons, and for neutrons below 25 MeV where the relative dose contribution from photons is higher. A radiation field of a specific type is fully described by the fluence, energy, and spatial distribution of the particles.

Radiation Field Properties

The spatial distribution of radiation in a therapeutic setting is divided into two regions based on the dose level and radiation quality. i) *In-field volume* is the directly irradiated volume where primary particles dominates the dose delivery. ii) *Out-of-field volume* that surround the in-field volume where secondary particles are the main contributors to dose delivery. In the out-of-field volume for a fixed beam treatment room, the neutron dose rate from heavier ions is higher in the forward direction than it is for protons, even though protons have a much higher intensity (more protons are required to deliver a prescribed dose than what is required for heavy ions), this is due to the mentioned fragmentation. At large angles however the isotropically emitted neutron dose from protons is higher than that from heavier ions. [**?**]. Ideally the energy and angular distribution of all particles throughout the entire room and shielding would be known,

Fluence describes the number of particles, dN, that passes through a cross-sectional area, dA, normal to the beam direction and has the unit m^{-2}:

$$\phi = \frac{dN}{dA} \,. \tag{5.0.1}$$

In radiation transport calculations, fluence can also be expressed as the density of particle trajectories in a volume,

$$\phi = \frac{dl}{dV} \,. \tag{5.0.2}$$

Where dl is the sum of particle trajectories in the volume dV [17].

Neutron yield (number of neutrons emitted per incident primary particle) and energy of the neutrons, generally increases with the energy and Z of the primary particle as illustrated in figure 5.2 showing the neutron yield in tissue (ICRU tissue phantom composed of: 76.2% O, 10.1% H, 11.1% C and 2.6% N) in the forward ($0° - 10°$ degrees) direction.

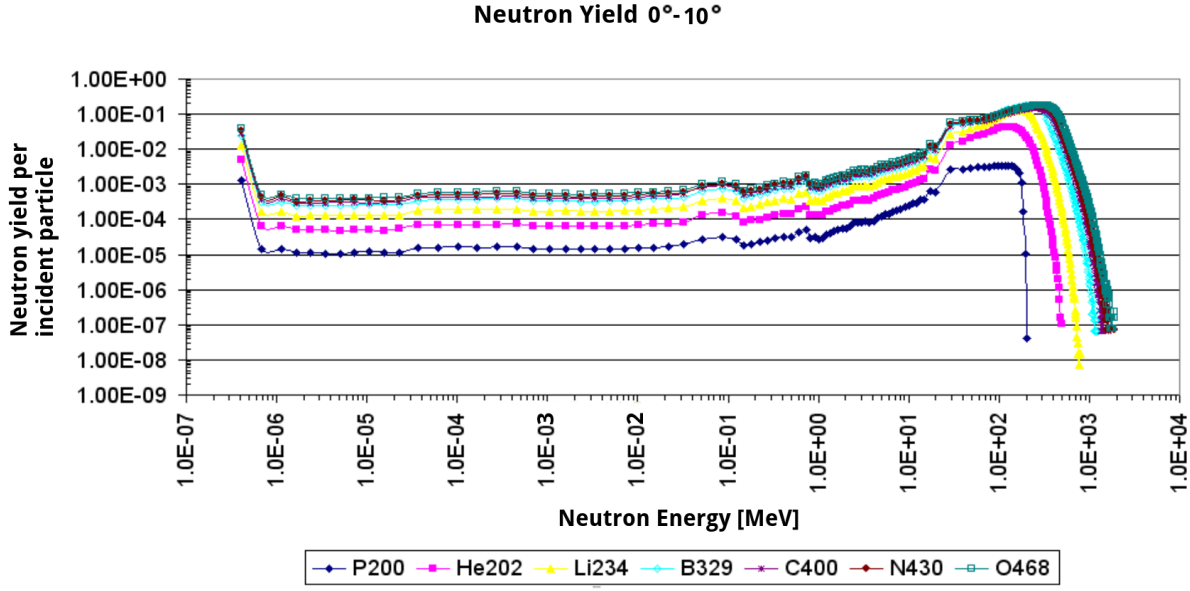

Figure 5.2: Total secondary neutron yield produced in the ICRU tissue phantom for various ions with energies so that the range in water was 26.2 cm; protons (200MeV), helium (202 MeV/n), lithium (234 MeV/n), boron(329 MeV/n), carbon (400 MeV/n), nitrogen (430 MeV/n and oxygen (468 MeV/n)) [17]

5.0.3 Radiation Protection in Radiotherapy

The IAEA has in its safety standards concerning radiation protection classified different radiological areas that are of concern in a radiation environment [41]. Figure 5.3 illustrates these radiological areas when applied to a particle therapy facility (in Germany, Italy and Switzerland [17]). Areas where the beam is active are inaccessible (dark blue), *controlled areas* where specific protection and safety measures are applied in order to control exposure and radiation contam-

ination (light blue), *supervised areas* where occupational exposure is supervised, but without any specific protective measures necessary (yellow), and *public area* that is unrestricted and open for the general public (green).

Shielding Barriers in a Fixed Beam Treatment Room

A particle therapy treatment room is composed of barriers that intercept radiation and aim to limit exposure leakage into supervised and public areas. Shielding walls, ceiling and floor are all an integral part of a treatment room and are divided into primary and secondary barriers. The *primary barrier* is the wall, or any other structure that intercepts the secondary radiation emitted at 0° from the interaction between the primary beam and target. Any other barrier that is not the primary barrier is considered to be a *secondary barrier*. Shielding walls in the forward direction (primary barrier) are thicker than the ones in the lateral and backward facing direction (secondary barriers), this is especially prominent in a fixed beam room as the radiation will always be directed at the primary barrier as opposed to a gantry that distributes the radiation over several primary barriers [42, 17].

The goal of shielding is to attenuate secondary radiation levels in order to keep them within regulatory dose limits and protect against unreasonable radiation exposure. Table 5.3 lists the factors that should be considered during shielding design. From a radiological perspective in a radio-therapeutic setting, neutrons are the most significant as these are produced in prominent numbers in beam line devices, patient and shielding, are scattered throughout the whole room and have the potential to carry and deposit energy a significant distance away from their initial induction site. Photons that arise in shielding due to neutron interactions are also of concern as they may escape the shielding with sufficient energy to cause ionization events in tissue [18].

Shielding can be estimated over a wide range of thicknesses by combining the inverse square law and exponential attenuation characterized by indirectly ionizing particles [18]

$$H(d,\theta) = \frac{H_\theta e^{d(\theta)/\lambda}}{r^2} \tag{5.0.3}$$

Where: $H(d,\theta)$ is the dose equivalent at depth d and angle θ in the shielding
H_θ is the dose equivalent term at production angle θ with respect to the incident beam
r is the distance between the target and point of interest outside the shield
λ is the effective attenuation length (attenuated by a factor of e) for dose equivalent through the shield.
In idealized circumstances, assuming that each increment of barrier thickness reduces the radiation by a constant factor, the *transmission factor* (T) of a barrier with thickness (x) may be expressed as:

$$T(x) = e^{-x/\lambda} \tag{5.0.4}$$

These analytical models are however limited in their use and superseded by Monte Carlo codes.

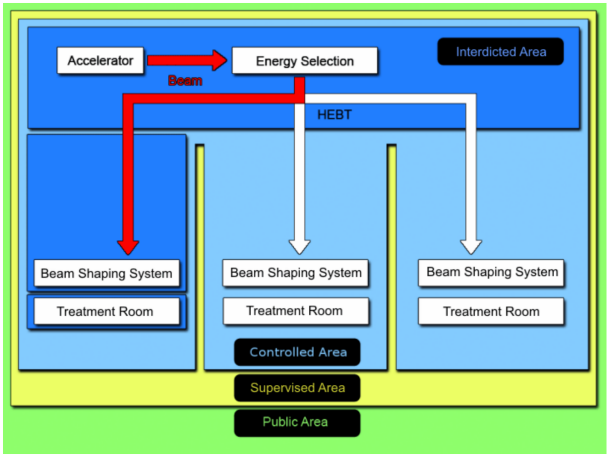

Figure 5.3: Classification of the radiological areas in a particle therapy facility based on safety concepts from the IAEA [17, p.85]

Table 5.3: Factors to be considered in shielding design[18]

ALARA Principle
Available Space
Comparison with other facilities
Construction Techniques
Environmental Radiation
Induced radioactivity
Radiation weighting factors
Radiation exposure history at the institution
Regulatory limits
Shielding materials
Trends in regulatory limits with time

Shielding Materials

Shielding must be comprised of enough material to effectively attenuate radiation of all energies and reduce the dose to acceptable levels. Materials of high atomic number and density are valuable in shielding against photons as the photon cross sections increase strongly with the Z of the material and the density of shielding ensure a high rate of interactions. Neutrons however, may attain energies that make them transparent to high-Z materials (Steel for instance is transparent to $\tilde{0}$.2-0.3 MeV neutrons) and require materials of low atomic number, especially hydrogen, that are more efficient at slowing down and capturing neutrons [17]. The most common radiation shielding materials are concrete and steel, with potential linings of boron to reduce thermal neutrons in mazes or at critical locations [18]:

- **Concrete** has the advantage of being a relatively inexpensive and readily available shielding material that can be poured into almost any configuration and used as structural support for both the building and any additional shielding. Ordinary concrete without any supple-

mentary materials has a density between 2.2 and 2.4 g/cm^3 and provides shielding against both photons, and neutrons, depending on the water content (5% water content is recommended for neutron shielding) [17]. Water contains hydrogen and this makes it efficient at slowing down fast neutrons (kinematically illustrated in chapter 2, section 2.3.1, equation 2.3.4) and at absorbing thermal neutrons due to its capture cross section, neutrons absorbed by hydrogen will however emit a $2.22MeV$ photon and may therefore be a source of unintended radiation and require additional gamma radiation shielding.

- **Boron** is sometimes introduced as linings (or by boronating concrete) and functions as a more efficient and potentially safer neutron absorber with its, higher than hydrogen, neutron capture cross section (as seen in chapter 2, figure 2.11) and that the neutron reaction with boron emits an alpha that is stopped locally and a $0.48MeV$ photon.

- **Steel** (or iron) is often used when space is limited as it has a high density ($\sim 7.4g/cm^3$) and is an efficient shield against photons and fast neutrons. There is however a build-up of low energy neutrons ($< 1MeV$) as the elastic scattering neutron cross section of materials with high atomic number is too small to efficiently stop these. Steel must therefore be followed by a hydrogenous material that can shield against low energy neutrons. Steel and concrete are therefore commonly combined, where steel is constructed towards the source and concrete is placed on the outside in order to remove these intermediate-energy neutrons generated in steel.

Shielded Doors and Mazes

A movable shielded door can be used to provide access to a treatment room, but several problems arise with such a solution. The door must offer the same degree of safety and radiation attenuation as the barrier that surrounds it, making it a very massive construction and important that it operates reliably and safely. Cracks and gaps around the perimeter of a door must be avoided to prevent leakage of scattered radiation, usually solved by overlapping shielding. Each individual door must be given special attention and proper design as every installation has its own unique configuration. This thesis will not go deeper into the design of a door, but a simple shielded (iron) door will be compared to a maze configuration in the results chapter 7

Instead of having a massive shielded door, a *maze* can be used as an entrance to a treatment room and is typically designed to avoid a direct propagation of radiation through a passageway, usually by having more than two *maze legs* that form one or more 90° bends as seen in figure 5.4. In the design of a maze, two basic rules are of consideration: i) The sum of the individual maze wall thicknesses should be equal to the thickness of the primary barrier. ii) Placement of the maze should be so that the forward-scattered radiation from the target is not directed towards it, implying that only a lower shifted energy distribution of secondary radiation enters the maze.

It is possible to analytically estimate the dose-equivalent inside a multi-legged mazes based on experimental data from an Am-Be neutron source and a concrete maze [18, 17].
The dose-equivalent in the first leg, where there is a dramatic change in the radiation spectrum, is essentially defined as an inverse square law with a scattering factor of two:

$$H(r_1) = 2H_0(r_0)(r_0/r_1)^2 \,. \tag{5.0.5}$$

And the succeeding legs, where the subsequent radiation spectra are similar to one another, in the form of two exponentials:

$$H(r_i) = \left(\frac{e^{-r_i/0.45} + 0.022A_i^{1.3}e^{-r_i/2.35}}{1 + 0.022A_i^{1.3}}\right)H_{0i}\,, i^{th}leg(i > 1)\,, \tag{5.0.6}$$

where for 5.0.5 and 5.0.6:
$H_0(r_0)$ = dose equivalent at a point in the mouth
r_0 = distance (in meters) from the source to the mouth of the labyrinth
r_1 = center line distance (in meters) of the first maze leg
r_i = center line distance (in meters) of the i^{th} leg
A_i = cross sectional area of the maze (typically door sized $1mx2m$)
H_{0i} = dose equivalent at the entrance to the i^{th} leg

So by increasing the length of the maze or decreasing the cross-sectional area will increase the attenuation and thus lower the dose-equivalent.

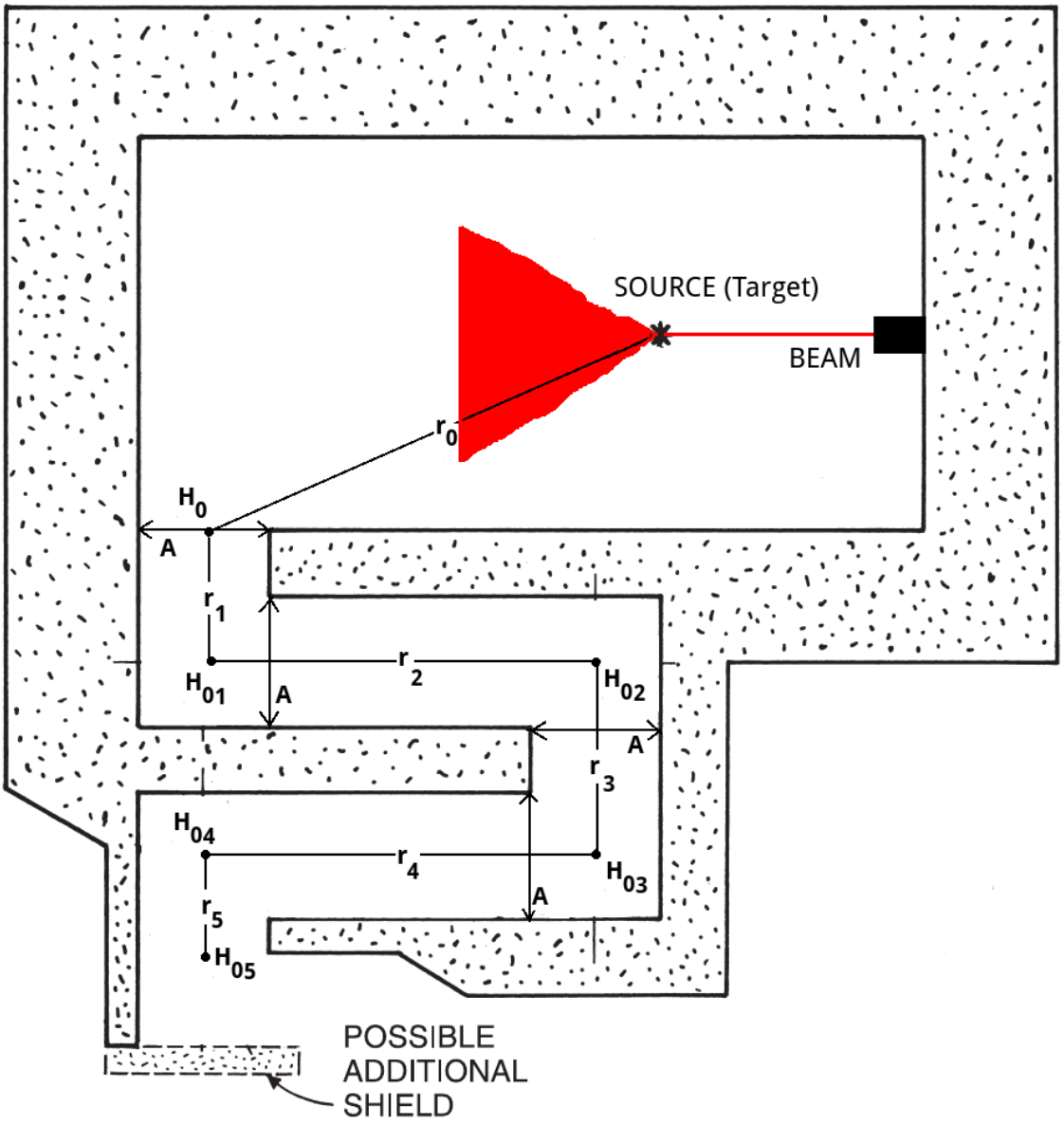

Figure 5.4: Example of a maze in a fixed beam treatment room where the walls are made of normal concrete and five legs with four 90° bends. [18, 17]

Chapter 6

The Monte Carlo Simulation Method

The Monte Carlo method is one of the most accurate and useful methods in computational physics and can be used to evaluate and simulate particle transportation when analytical and numerical calculations are impossible due to complicated geometries or the presence of too many degrees of freedom. In essence, the Monte Carlo method creates a solution to a macroscopic system by simulating the system's microscopic interactions [43].

Using probability distributions containing all physical processes and interactions that occur at the atomic level and under (detailed in chapter 2), it becomes possible to follow and keep a history of an individual particle's energy and path through matter by randomly choosing an event from the distribution. These probability distributions are obtained from experimental measurements or from reliable models of particle transportation and aim to mimic the fundamental interaction processes that occur. For each step the particle takes, a new energy, direction or path length value will be obtained until the particle gets absorbed, leaves the region of interest or its energy falls below a user defined threshold, for this reason it is important to keep the step size small in order get good resolution. The desired statistical precision and information to be obtained will depend on the number of histories (N), as the error in Monte Carlo calculations is proportional to $1/\sqrt{N}$. The increase in computation time with increasing N is also of importance as Monte Carlo simulations can be very data heavy and time consuming [18, 44].

There are several Monte Carlo codes available concerning particle transportation, but this thesis will only focus on *FLUKA*, a general purpose tool for calculations of particle transport and interactions with matter. This Monte Carlo code will be detailed together with a summary of the physical models behind it in the section below.

6.1 FLUKA

FLUKA is a multi-purpose transport Monte Carlo code capable of handling and simulating about 60 different particles in a wide range of energies spanning from thermal energies (for neutrons) or $0.1 - 1$ keV (for all other particles) up to thousands of TeV (20 TeV for hadrons and neutrons) with high accuracy. It is widely used in basic physics research and has many

applications in various fields including shielding design, dosimetry, radiotherapy, particle accelerators, etc. FLUKA is based on microscopic models and conservation laws are enforced at every step, this ensures a solid physical base and consistency among all reaction steps and reaction types. Results are further benchmarked against experimental data, making the final predictions with a minimal set of free parameters. All physical models are integrated into the code and the user has limited means of tuning them [45, 46].

6.1.1 Physics and Models in FLUKA

The following is an excerpt from the FLUKA manual [46, p.4-7], detailing and summarising the physical models, capabilities and limitations of FLUKA:

Hadron inelastic nuclear interactions;

Inelastic hadron-hadron cross sections are represented by parametrised experimental fits.
Interactions are simulated by the Dual Parton Model (DPM) for particles with momentum < 20 TeV/c and > 5 GeV/c, and by resonance production and decay model from threshold momentum to 5 GeV/c.
Inelastic hadron-nucleus interactions are simulated by Glauber-Gribov multiple scattering and Generalised Intranuclear Cascade (GINC) for particle momentums < 20 TeV/c and > 5 GeV/c, and by the Preequilibrium-cascade model(PEANUT) below 5 GeV/c.

Elastic Scattering;

Parametrised nucleon-nucleon cross sections and tabulated nucleon-nucleus cross sections and phase shift data on pion-proton, as well as detailed kinematics of elastic scattering on hydrogen nuclei and proton recoil transport.

Nucleus-Nucleus interactions;

DPMJET-II or DPMJET-II is used for energies above 5 GeV/u, between 0.125 and 5 GeV/u a modified Relativistic Quantum Molecular Dynamics (RQMD) model and below 0.125 GeV/u the Boltzmann Master Equations (BME) is used.

Transport of charged hadrons;

Uses Bethe-Bloch theory with Mott correction to Rutherford scattering cross section and shell and low energy corrections from Ziegler.
Optional delta-ray production and transport.
Ionisation potentials and density effects parameters from Sternheimer, Berger and Seltzer.
Non-ionising energy losses (NIEL) and Displacements Per Atom (DPAs).
Special transport algorithm based on Molière's theory of multiple Coulomb scattering improved by Bethe.
Accurate treatment of boundaries and curved trajectories in magnetic and electric fields.
Path length correction and automatic control of the step.
Spin-relativistic effects at the level of the second Born approximation.

Nuclear size effects (scattering suppression) on option.
Fano correction for heavy charged particle multiple scattering.
Single scattering algorithm based on the Rutherford formula with a screening factor in the form used by Molière, integrated analytically without any approximation, and nuclear form factors and spin-relativistic corrections at the first or second Born approximation level accounted for by a rejection technique.
Correction for cross section variation with energy over the step.
Bremsstrahlung and electron pair production at high energy by heavy charged particles, treated as a continuous energy loss and deposition or as discrete processes depending on user choice.
Muon photo nuclear interactions, with or without transport of the produced secondaries.

Low energy neutrons;
FLUKA uses its own neutron cross section library (multigroup P5) for energies lower than 20 MeV and contains over 250 different materials that are of interest in physics.
Gamma-ray generation and different temperatures available and Doppler broadening for temperatures above 0 K.
Transport uses standard multigroup with photon and fission neutron generation, detailed kinematics of elastic scattering on hydrogen nuclei. Transport of proton recoils and protons from N(n,p) reaction and capture photons are generated according to multigroup treatment, but transported with the more accurate EMF package.

Photons;
Photoelectric effect with actual photo-electron angular distribution according to the fully relativistic theory of Sauter.
Parameterisations/tabulations for photoelectric cross sections including all known edges up to Z = 100 and down to a few eV.
Compton effect with Doppler broadening using a fit of the Compton profiles, and accounts for atomic bonds through use of inelastic Hartree-Fock form factors.
Rayleigh scattering.
Pair production with actual angular distribution of electrons and positrons, including Landau-Pomeranchuk-Migdal pair production suppression effect.
Photon polarisation taken into account for Compton, Rayleigh and Photoelectric effects.

6.1.2 FLUKA Geometry

For creating geometries, FLUKA uses an entirely rewritten and improved version of the Combinatorial Geometry (CG) package from MORSE with additional bodies like infinte planes and cylinders. The user can define and combine "bodies" of various shapes and sizes and assign materials to body defined "regions". This lets the user create and define complex and accurate geometries such as detectors, therapeutic beam delivery systems, treatment rooms, etc [46].

6.1.3 FLUKA Input

The interaction between FLUKA and users is based on text input files written in a standard ASCII character encoding scheme with the file extension .inp and may contain the following information [46]:

- Title and comments
- Description of the problem geometry
- Definition of the materials involved
- Material assignments
- Definition of the particle source
- Definition of requested detectors used to calculate physical quantities like dose, fluence, etc.
- Definition of biasing schemes, problem settings such as energy cutoffs, step size, optional physical effects, etc.
- Initialisation of the random number sequence, starting signal and number of requested histories.

The user can directly define the type of beam particle, its energy (or momentum), starting position and direction of the beam in these input files. Rarely is any programming required from the user, but in the case of more complex beams (therapeutic beams), special user routines can be written in Fortran 77 and linked to the input file.

Chapter 7

Monte Carlo Simulations, Methods and Results

This chapter will describe the simulation setups defined in flair and run by FLUKA, as well as describe their performance, motivation, and results. The FLUKA Monte Carlo code version 2011.2c-2, and *flair - FLUKA Advanced Interface*, version 2.1-7 was applied in all parts of this thesis. The geometry editor in flair, *Geoviewer* was instrumental in the designing and relative positioning of all geometries that make up the treatment rooms and phantoms in the simulations. Processing and plotting of the simulation outcomes were also done in flair by utilizing its incorporated Gnuplot environment.

The number of particles simulated in each simulation setup is guided by the work done by J. Bauer et al, who evaluated Monte Carlo simulations with an analytical treatment planning system. They evaluated the number of simulated primary beam particles in Monte Carlo simulations via a sensitivity study that depended on the fraction of simulated particles with respect to the number of total particles in the treatment plan. Their results for achieving sufficient Monte Carlo statistics with reasonable computation time, showed that $0.5 - 1\%$ of the total number of treatment particles when applying protons, and at least 1% (up to 6%) of the total number of carbon ions in a treatment fraction should be simulated 14. The number of particles simulated in each setup in this project work are gathered in table C.1 in appendix **??**.

Due to the high number of geometrical layouts and scoring situations in this project work, eight different simulation set-ups for each of the three particles (24 simulations in total) were designed and run separately with the intent of streamlining the execution of the simulations with the computer resources available, and allowing the processing of the results to happen in succession. Each simulation is identified by a *"simulation name"* as listed in table C.1 and the individual simulation setups are further illustrated in Appendix **??**, section C.2-C.8.

The comparative feature of this project work necessitates the determination of aspects and variables that are to be kept constant and consistent across all simulations in order to normalise the results and limit variations. This is realized by defining the treatment beam, dose delivery and treatment room to have the same properties for all three particle types in all simulations. The treatment beam, treatment room and individual simulations defined for FLUKA are detailed in section 7.1, 7.2 and 7.3 respectively. Results from the individual simulations are processed and presented in section 7.4. Section 7.5 presents *annual dose* calculations and results

to water equivalent phantoms outside the treatment rooms.

7.1 Definition of Therapeutic Treatment Beam

Kine Johnsen designed in her thesis "Simulations of a Therapeutic Proton Beam with FLUKA Monte Carlo Code and Varian Eclipse Proton Planning Software" [22] an actively modulated proton beam resembling a spot scanning system that aimed to deliver a homogeneous dose to a target volume located at a defined depth inside a water phantom. This was achieved by editing and linking a *source.f* user routine to the FLUKA input file. This user routine contains an energy distribution and a set of weights that are randomly applied to the simulated primary beam particles and subsequently form a SOBP covering the target volume longitudinally. The user routine simultaneously defines initial beam particle positions that covers the target volume laterally. This thesis builds upon the work performed by Kine Johnsen by editing the energy distribution, weights and beam position for the three particles, proton, helium, and carbon. The beams are defined to fully cover a $5 \times 5 \times 5cm^3$ Target Volume, located at the depth 15cm to 20cm depth in a water phantom situated at a fixed position in the treatment room, with a homogeneous *physical treatment dose* of $2Gy$. The creation of the energy distribution and weights for each of the beams in the source.f files that form the SOBP and longitudinal dose coverage of the target, is based on the Bragg-Kleeman (BK) relationship between range and energy of the particle in a material [8, 47],

$$\mathcal{R} = \alpha E^{p_0} \, . \tag{7.1.1}$$

E is the initial energy of the particle, α and p_0 are material dependent constants. The α and p_0 parameters for proton, helium and carbon used in this project work are found in table 7.1 and were obtained from the work done by Wayne D. Newhauser and others, who fitted the exponential BK rule to range curves and experimental data from proton, helium and carbon ions over a wide range of energies [8].

To create a SOBP spanning a desired range, several successive beams of sequential energies must be added together. The range of each of these contributing beams ($k = 1, 2, ..., n$) are determined by the equation,

$$r_k = \left[1 - \left(1 - \frac{k}{n}\right)\chi\right] R_0 \, , \tag{7.1.2}$$

where R_0 is the desired maximum depth, χ is the fraction of the maximum depth and width of the SOBP, and n is the number of energy intervals involved [22]. By applying the ranges from equation 7.1.2 to the BK rule 7.1.1, the corresponding energy of each beam (e_k) in the SOBP are obtained,

$$e_k = \left(\frac{r_k}{\alpha}\right)^{\frac{1}{p_0}} \, . \tag{7.1.3}$$

In order to achieve a flat *dose plateau* in the SOBP, the individual beams must be weighted such that the proximal Bragg peak in the SOBP receives the lowest weight and the distal Bragg peak receives the highest, as detailed in theory chapter 4, section 4.2. These beam weights w_k are calculated by the equation[22, 47],

$$w_k = \begin{cases} 1 - (1 - \frac{1}{2n})^{1-\frac{1}{p}} & \text{for } k = 0 \\ [1 - \frac{1}{n}(k - \frac{1}{2})]^{1-\frac{1}{p}} - [1 - \frac{1}{n}(k + \frac{1}{2})]^{1-\frac{1}{p}} & \text{for } k = 1, ..., n-1 \\ (\frac{1}{2n})^{1-\frac{1}{p}} & \text{for } k = n \end{cases} . \tag{7.1.4}$$

The parameter p will vary slightly with energy, depth and width of the SOBP as seen in K. Johnsen's work. The p values in table 7.2 have been found to give a sufficiently flat SOBP plateau for this thesis.

The maximum range (R_0) and SOBP width used in conjunction with equations 7.1.2, 7.1.3 and 7.1.4 to find the necessary energy range and corresponding weights needed to create a SOB at a predefined depth, are listed in table 7.3. In this thesis, 50 equidistant beam energies are applied and the maximum range for both the protons, helium and carbon ions, is set to approximately 20cm depth in water. In the FLUKA source.f file, the energies are listed as **DATA ENEDGE** in GeV, and the weighting factors under **DATA CUMPR**. The user routines were further edited with initial particle coordinates constructed to fully cover the target volume in the lateral (x and y) directions.

```
* Particle coordinates [cm] that cover the volume in X and Y direction:
* Gaussian sigma 0.297(=0.7FWHM) to account for lateral spread of beam
*Proton:
      CALL FLNRR2(RGAUS1, RGAUS2)
      XFLK (NPFLKA) = (-3.43 + 0.297*RGAUS1)+ FLRNDM(DUMMY)*6.92
      YFLK (NPFLKA) = (-3.445 + 0.297*RGAUS2)+ FLRNDM(DUMMY)*6.905
      ZFLK (NPFLKA) = ZBEAM
```

The full details of the source.f files are found in appendix A.

Table 7.1: Fitting parameters α and p for water when applying the BK rule.

Particle type	α	p_0
Proton	$2.633x10^{-3}$	1.735
Helium	$2.367x10^{-4}$	1.735
Carbon	$5.605x10^{-5}$	1.545

Table 7.2: p-values used for calculating the beam weights.

Particle type	p
Proton	1.6
Helium	1.54
Carbon	1.543

Table 7.3: Predefined values R_0 and SOBP width used to calculate the range and corresponding energies.

Particle type	Maximum range (R_0)	SOBP width	Minimum energy	Maximum energy
Proton	20.35 cm	5.085 cm	147.3 MeV	174.4 MeV
Helium	20.22 cm	4.8 cm	147.4 MeV/n	172.8 MeV/n
Carbon	20.04 cm	4.52 cm	280 MeV/n	331.5 Mev/n

Results

The resulting longitudinal and lateral dose profiles of the proton, helium, and carbon beam defined in their source.f files, are displayed in figure 7.1, 7.2 and 7.3 respectively. The dose plateau inside the target volume deviates no more than 4% from the set 100% (2Gy) level. A measure of the physical dose coverage inside the target volume was obtained by measuring the ratio between the volume covered by the 95% (1.9Gy) isodose line and the total volume of the Target Volume,

$$\frac{V_{95}}{V_{TV}} \, . \tag{7.1.5}$$

The dose coverage achieved and listed in table 7.4 is within 0.5% for all three particle beams.

Table 7.4: Dose coverage factors and plateau deviations.

Particle type	Dose Coverage	Plateau Deviation from 2Gy
Proton	0.995	1.2%
Helium	1.004	3.25%
Carbon	1.001	2.7%

To obtain a more clinically optimized dose deposition based on the sparing of healthy tissue and the effect of the higher RBE of helium and carbon ions, a designated Treatment Planning Software such as Eclipse (Varian) should be used. The goal of this thesis however, is not to make clinically optimized treatment plans and the transition from physical to effective dose in the Target Volume is an normalization aspect not applied in this work. The dose deposition is instead normalized to a *physical dose* of $2Gy$ and the 95% coverage factor of 1.000 ± 0.005 are kept consistent through all simulations in this project work. The normalization to 2Gy is done by determining the number of primaries that are needed in a single treatment fraction to achieve 2Gy in the SOBP plateau. Simulation results obtained from FLUKA are intrinsically normalized to *per primary* and by studying the dose profile plots and the FLUKA calculated integral of total energy deposited per primary in a projection covering the Target Volume, the number of primaries in a single treatment fraction delivering 2Gy was obtained and collected in table 7.5.

Table 7.5: Number of Primaries in a treatment fraction delivering 2 Gy to the CTV.

Particle type	# of primaries in a treatment fraction
Proton	5.814E10
Helium	1.34E10
Carbon	2.268E8

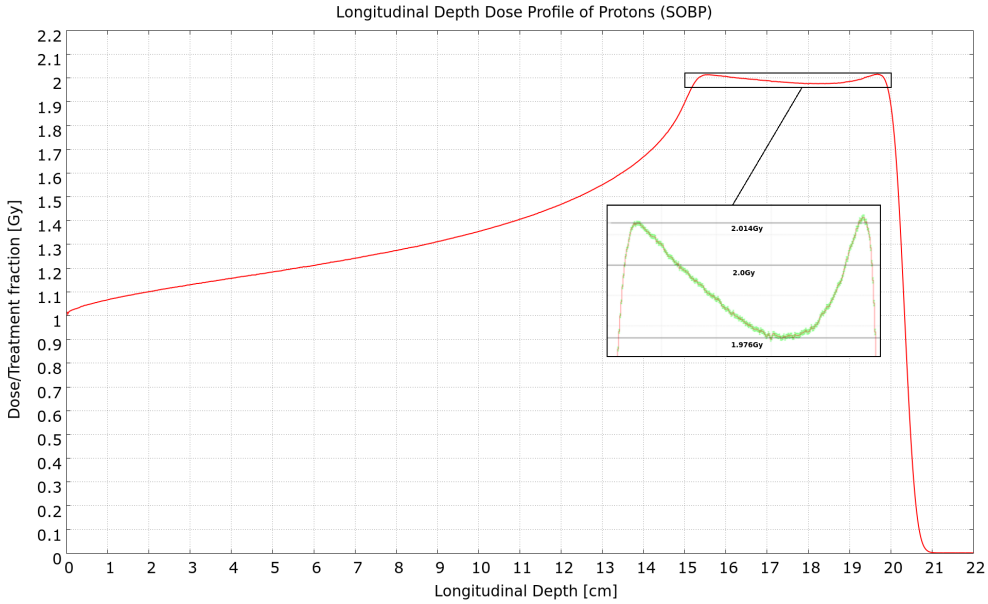

(a) Depth dose profile along the central beam axis for protons with energies 147-174 MeV. The Target Volume covered by the dose is located at the 15cm-20cm range.

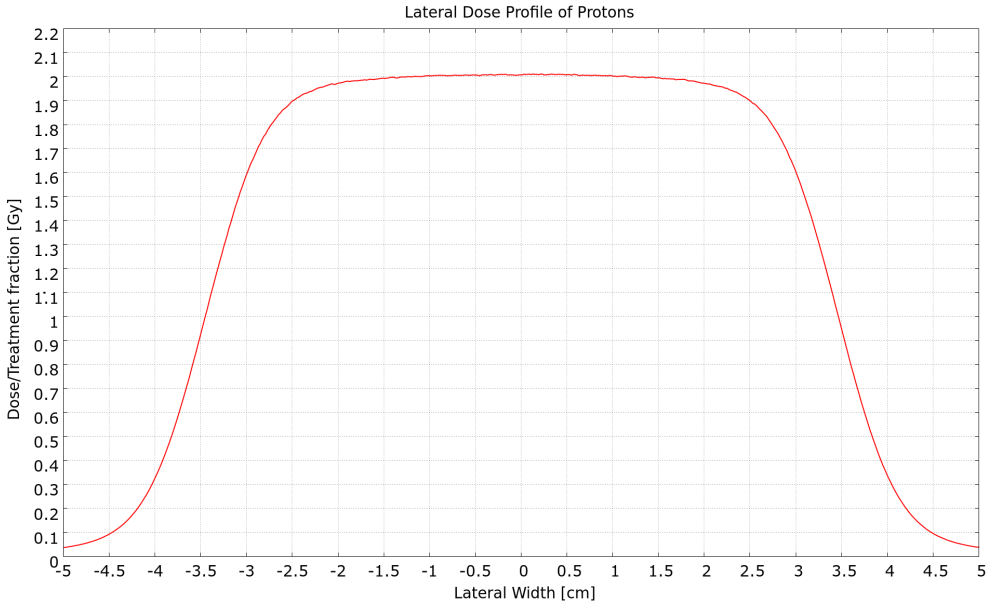

(b) Lateral dose profile of treatment protons, the Target Volume is located at the $-2.5cm$ to $2.5cm$ range.

Figure 7.1: The longitudinal dose profile (a) and lateral dose profile (b) of the actively modulated proton beam defined in the source.f user routine and simulated in FLUKA.

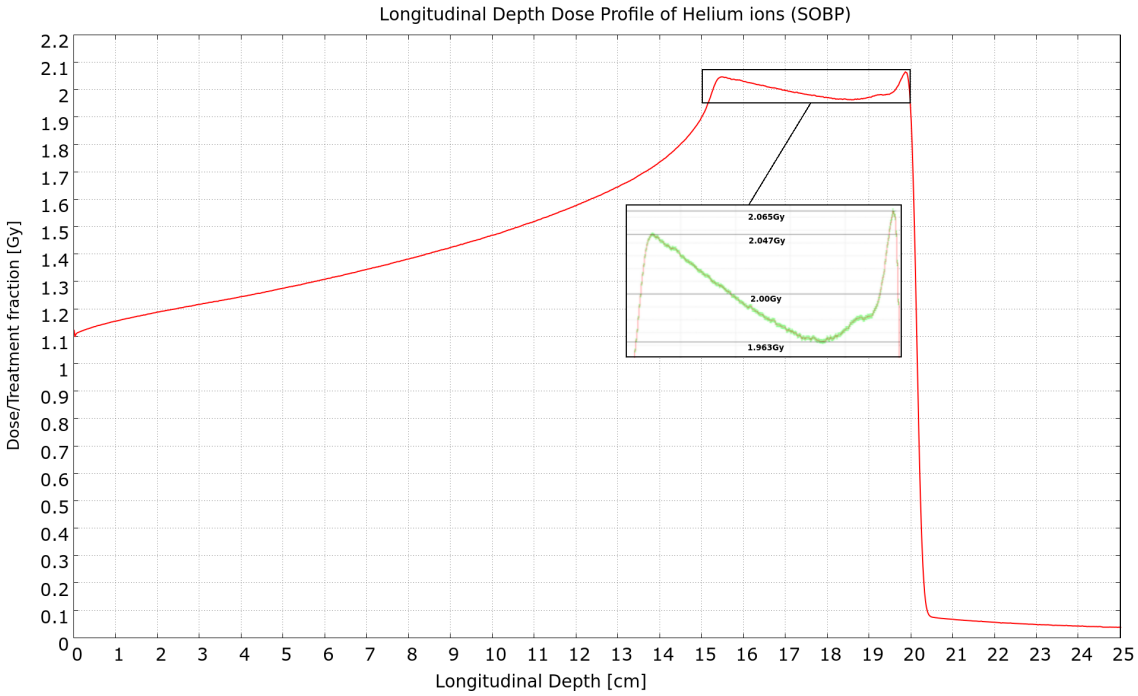

(a) Depth dose profile along the central beam axis for helium ions with energies 147-173 Mev/n. The Target Volume covered by the dose is located at the 15cm-20cm range.

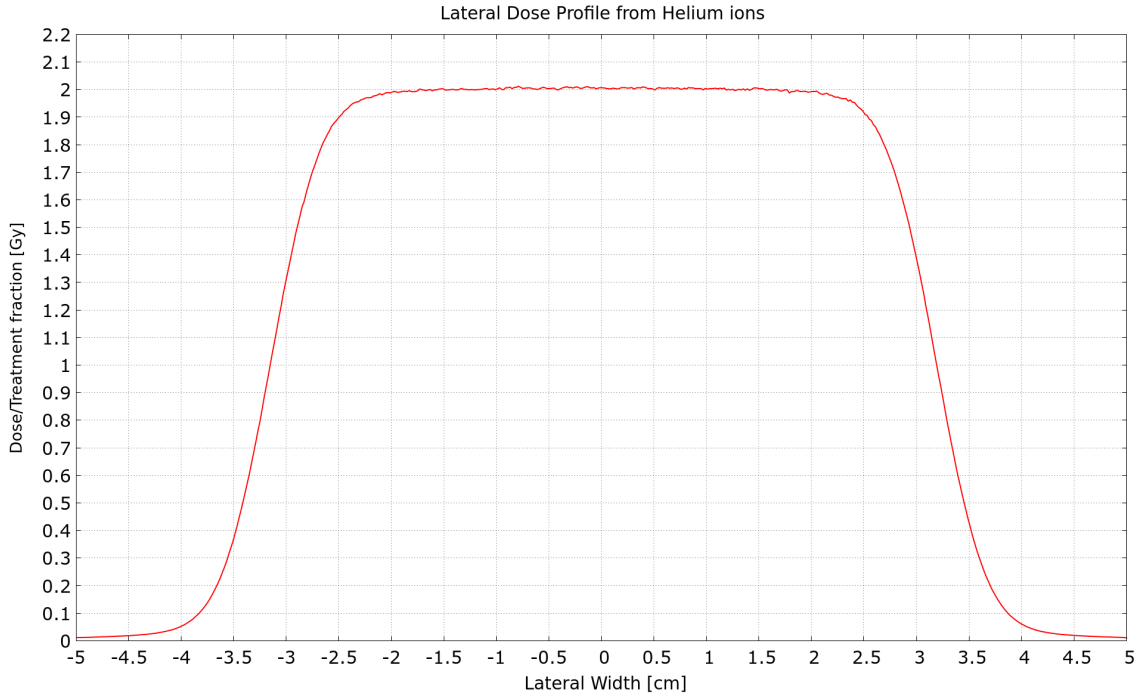

(b) Lateral dose profile from helium, the Target Volume is located at the $-2.5cm$ to $2.5cm$ range.

Figure 7.2: The longitudinal dose profile (a) and lateral dose profile (b) of the actively modulated helium beam defined in the source.f user routine and simulated in FLUKA.

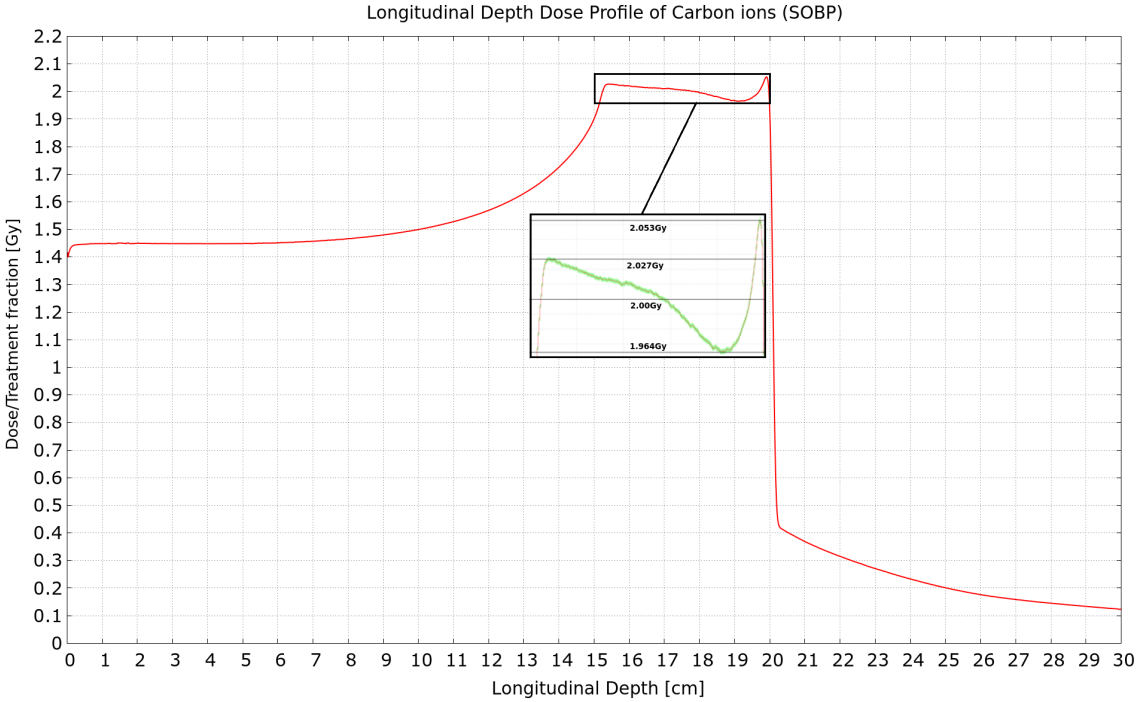

(a) Depth dose profile along the central beam axis for carbon ions with energies 280-331.5 MeV/n. The Target Volume covered by the dose is located at the 15cm-20cm range.

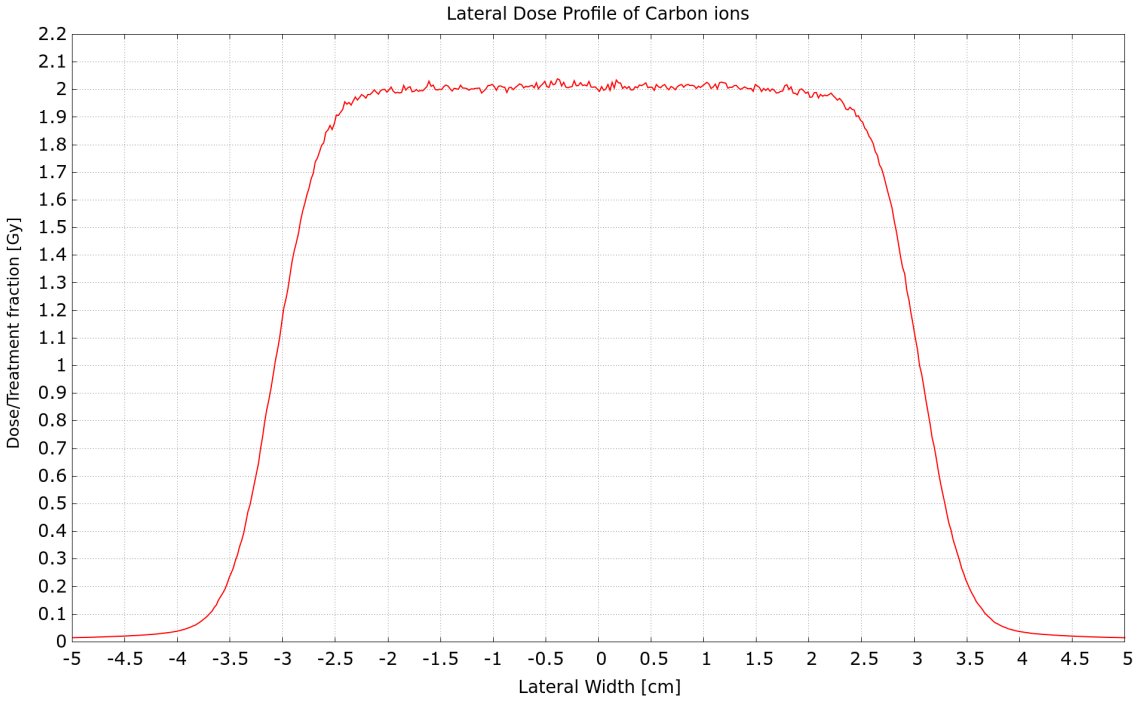

(b) Lateral dose profile from carbon, the Target Volume is located at the $-2.5cm$ to $2.5cm$ range.

Figure 7.3: The longitudinal dose profile (a) and lateral dose profile (b) of the actively modulated carbon beam defined in the source.f user routine and simulated in FLUKA.

7.2 Creation of Treatment Room in FLUKA

The treatment room is modelled after a technical drawing of a two gantry treatment room (SC360, model version D0001177) setup from ProNova Solutions, a status report on the MedAustron project (an Austrian ion therapy and research centre) [48], public images of a fixed beam treatment room at the Heidelberg Ion-Beam Therapy Center (HIT) [49] and the treatment room model used in the project thesis of John Alfred Brennsæter [50]. The treatment room set up in FLUKA's Geoviewer application, and used as the foundation for all simulation set-ups featured in this thesis, is illustrated in figure 7.4 and has the following dimensions; $1300cm$ along the z-axis (length), $880cm$ along the x-axis (width) and $450cm$ along the y-axis (height). The room is filled with air and surrounded by $200cm$ thick concrete walls on all sides except for a $400cm$ thick forward facing wall (primary barrier). The direction of the simulated beam is always along the positive Z-axis (parallel to the floor and flank walls) and starts at position $0, 0, -100cm$ ($1m$ before the water phantom functioning as the patient). No additional beam components, such as those discussed in chapter 4, figure 4.4, panel (b), are introduced into the beam line in this project work.

A liquid water phantom modelled after an average adult human torso ($70 \times 20 \times 40cm^3$ [4]) functions as the patient and has its isocenter placed 120cm above the floor, 480cm away from the primary barrier and 440cm from the two flank walls. Several other water phantoms (named Worker1,2,3 and 4) with the same proportions as the patient phantom ($40 \times 70 \times 20cm^3$) are placed in the upright position at key scoring locations in the different simulation setups where relevant. A relevant simulation layout is shown in figure 7.5 and illustrates how the worker phantoms are arranged. All simulation geometries and layouts created for this thesis are detailed in appendix **??**, and densities and molecular contents of all materials involved are listed in appendix B.

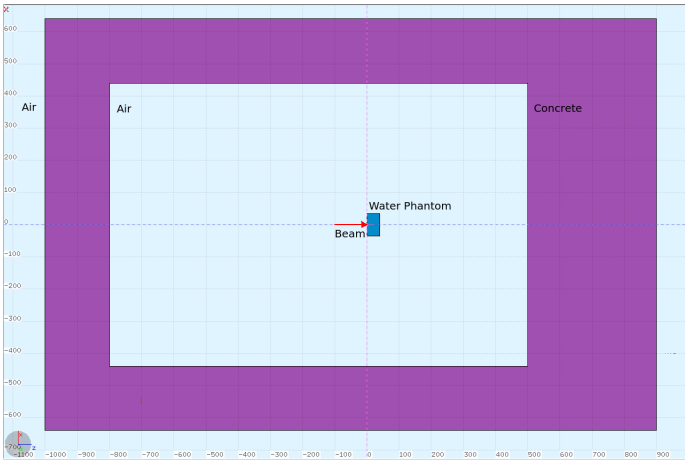

(a) Two dimensional layout of the basic treatment room as set up in Geoviewer and viewed along the y-axis (top-down view).

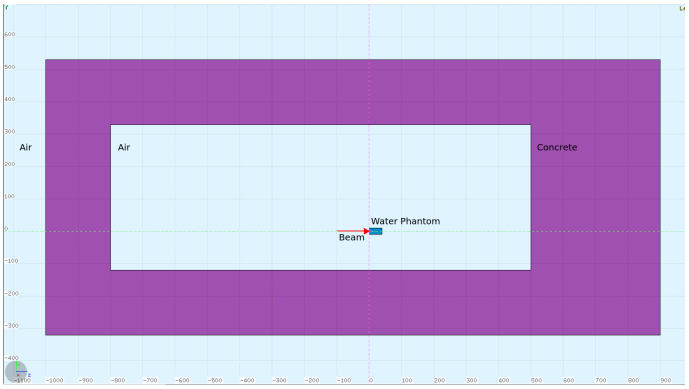

(b) Two dimensional layout drof the basic treatment room as set up in Geoviewer and viewed along the x-axis (side view).

Figure 7.4: Two dimensional layouts of the basic treatment room viewed along the (a) y-axis and (b) x-axis.

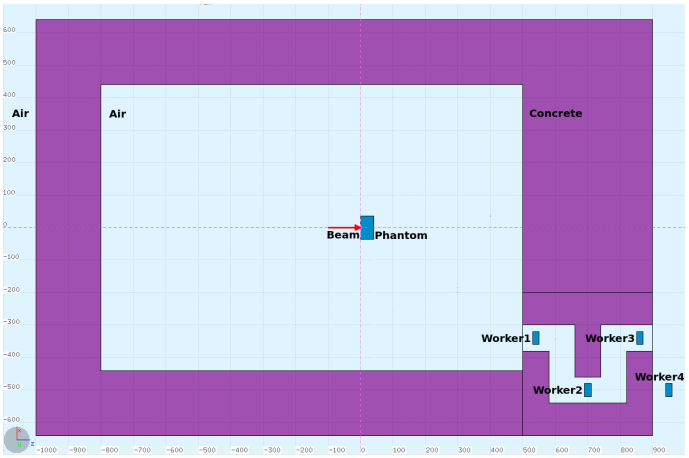

Figure 7.5: Two dimensional layout of the *"RightMaze"* setup as viewed along the y-axis (top-down view).

7.3 FLUKA Simulations

Each of the eight individual simulation setups used in this project work are detailed in appendix C, and two-dimensional layouts are found in their respective sections C.0.1-C.0.8. The computing resources available made it possible to run a total of six simulations simultaneously where each run would take approximately 90 hours to complete. Every simulation was performed with proton, helium, and carbon ions separately for a total of individual 24 simulation runs, the number of simulated primaries in each simulation are listed in table C.1 in appendix C. In this project work each simulation setup is identified and referred to by an *"identification name"*.

"WaterPhantom"(appendix C.0.1) and ***"ClosedRoom"*** (appendix C.0.2) were created and performed in order to score the secondary particle production induced in the interactions between the treatment beam and treatment phantom. Fluence scoring detectors and regions were designed to give insight into the effect of back scattered particles of off treatment room walls by assessing the difference in dose and fluence entering the treatment phantom, both with and without surrounding walls.

"RightMaze" (appendix C.0.3) was built with a zigzagged maze made of four 90° bends and functions as the entrance to the treatment room, the maze was placed inside the primary barrier. The sub-geometry ***"RightMazeBoron"*** (appendix C.0.4) considers an identically placed maze, but with two added boron layers located inside the last two maze arms.

"MiddleMaze" (appendix C.0.5) has a pure concrete maze with the same proportions and dimensions as the maze in *"RightMaze"*, but is located inside the right flank wall of the treatment room.

MiddleDoor (appendix C.0.6) considers a straight corridor through the right flank wall and separates the inside and outside of the treatment room with a 100cm thick iron door.

PrimaryBarrier (appendix C.0.7) focuses on the 400cm thick forward facing primary barrier made of pure concrete.

BeamDump (appendix C.0.8) considers the dumping of the treatment beam into a 30cm tick steel layer covering the first part of the primary barrier.

In order to assess the dosimetric consequences of the changes in the entrance geometries and through the introduction of shielding materials, water equivalent phantoms called Worker1, 2, 3 and 4 were placed at various locations inside and outside the structures of interest. Their exact locations are shown and detailed in the individual simulation layouts found in their respective layout sections in appendx C. Each worker phantom has dose scoring detectors measuring their respective effective doses associated with them. These scoring detectors implements fluence conversion factors based on the 2007 recommendations from the

ICRP, and outputs the effective dose in $pSv/primary$. Each result is manually normalised to $mSv/treatmentfraction$ and illustrated as bar charts with a logarithmic y-axis in applicable parts of the results found in section 7.4. Detailed results and error bars associated with the effective doses are gathered in appendix F, table F.1.

Differential fluence spectrum of particles entering and exiting specific structures, with an emphasis on photons and neutrons due to their penetrative properties, were scored and plotted in an isolethargic manner. This means that the differential fluence spectra are plotted as,

$$\frac{d\Phi}{d(logE)} = E\frac{d\Phi}{dE}\,. \tag{7.3.1}$$

Such plots were chosen due to the fact that isolethargic spectra plotted with a logarithmic x-axis and linear y-axis, ensures that the area under the curve between two points $log(x_1)$ and $log(x_2)$ are proportional to the integral of $E(x)$ resulting in an intuitive and informative plot of the energy distribution and corresponding fluence. In addition, 2-dimensional colour plots of particle fluence through specific structures are added for the sake of visualising particle paths and fluence intensity in a bin by bin basis, but note that unless specified otherwise, all 2-dimensional colour plots are from the carbon treatment beam. The carbon beam was chosen for this for having the highest energy and fluence activity compared to the proton and helium treatment beam. It should be noted that all isolethargic fluence plots are shown with error bars for either Carbon and helium exclusively, this was done for the sake of readability. Error bars that are omitted are of the same order as the error bars plotted unless specified otherwise in the figure caption.

7.4 Results

WaterPhantom and ClosedRoom

In the *"WaterPhantom"* simulation (layout drawing C.0.1 in appendix C.0.1) a scoring region was placed on the back-side of the patient phantom (towards the primary barrier) in order to score the differential fluence of selected secondary particles exiting towards the primary barrier. This same scoring region was applied to simulation *"ClosedRoom"* (layout drawing C.0.2, appendix C.0.2) in order to score the differential fluence of neutrons and photons entering the patient phantom due to backscattering off of the primary barrier. Resulting isolethargic differential fluence of neutrons and photons exiting and entering the patient phantom are found in figure **??** and 7.7 respectively. Figure 7.6, panel (a) show that the majority of neutrons exiting are fast neutrons. Panel (b) in the same figure show the energy spectrum of neutrons entering the backside of the patient phantom and an elevated thermal peak is noted. Figure 7.7, panel (a) and panel (b) show photons exiting and entering the backside of the patient phantom respectively. Some characteristic photon peaks are observed, notably the characteristic $511keV$ photo-peak from electron-positron annihilation and the $2.2MeV$ photon peak characteristic of

hydrogen neutron capture. Additional plots of secondary protons, helium 4 and heavy ions exiting the patient phantom for each of the three treatment beams are found in appendix D, figure **??**. Fluence of backscattered protons, helium and heavy ions entering the patient phantom are negligible.

In addition to the differential fluence spectrum of secondary particles exiting and entering the backside of the patient phantom for each of the three treatment beams, a comparison of the absorbed dose and fluence inside the patient phantom from some selected secondary particle types, was made. This was performed in order to investigate the difference in dose to the patient phantom with the inclusion of surrounding walls (*"ClosedRoom"*). The results displaying the absorbed dose and composite fluence spectra inside the patient phantom are listed in appendix E, table E.1 and table E.2 respectively. The results show that there is less than 0.3% increase in neutron fluence and 0.8% photon fluence in the patient phantom when there are walls present. The change in absorbed dose to the patient phantom is observed to be approximately zero.

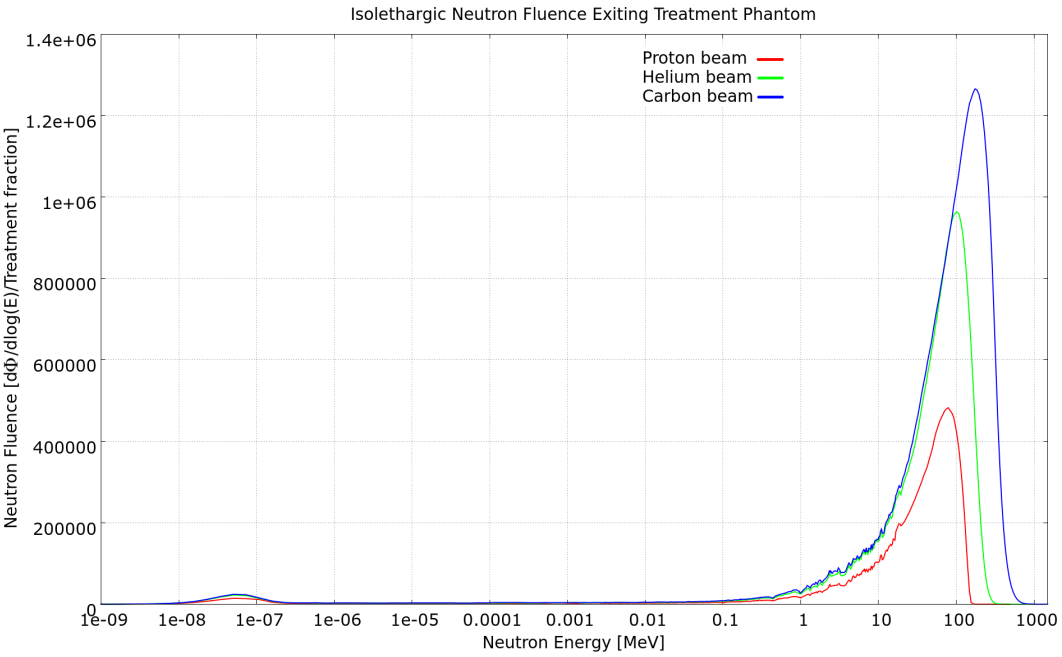

(a) Isolethargic differential fluence spectrum of neutrons exiting the backside of the patient phantom. Error-bars are omitted completely from the figure for the sake of readability as they are too small to be effectively read

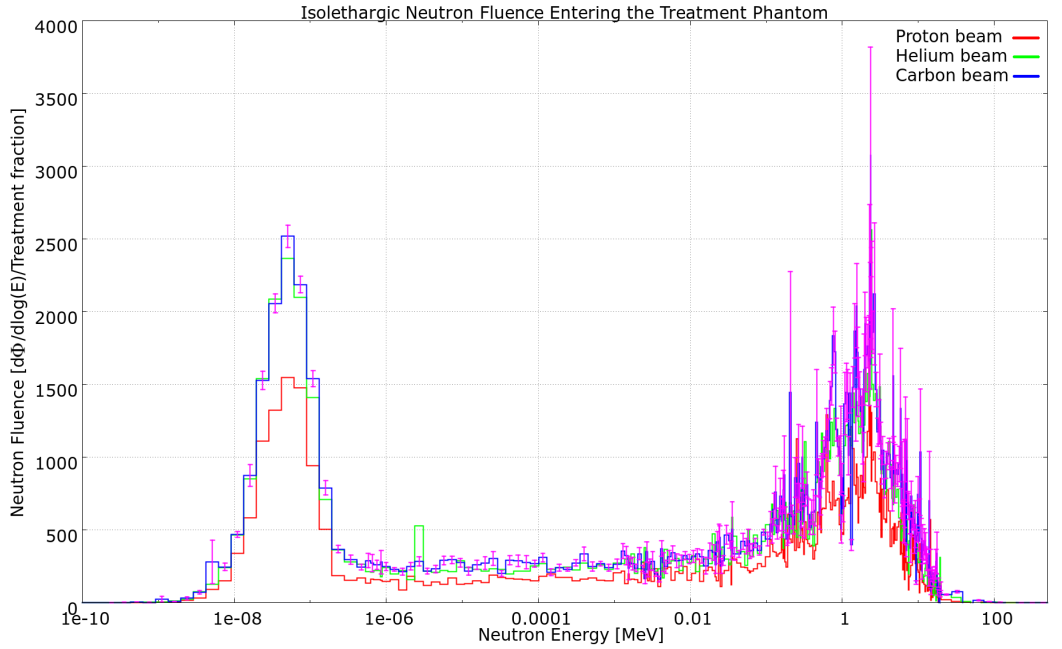

(b) Isolethargic differential fluence spectrum of neutrons entering the back-side of the patient phantom. Results are corrected for neutrons entering the phantom when there are no walls.

Figure 7.6: Panel (a) shows the energy distribution of neutrons exiting the patient phantom. Panel (b) shows the energy distribution of neutrons entering the patient phantom.

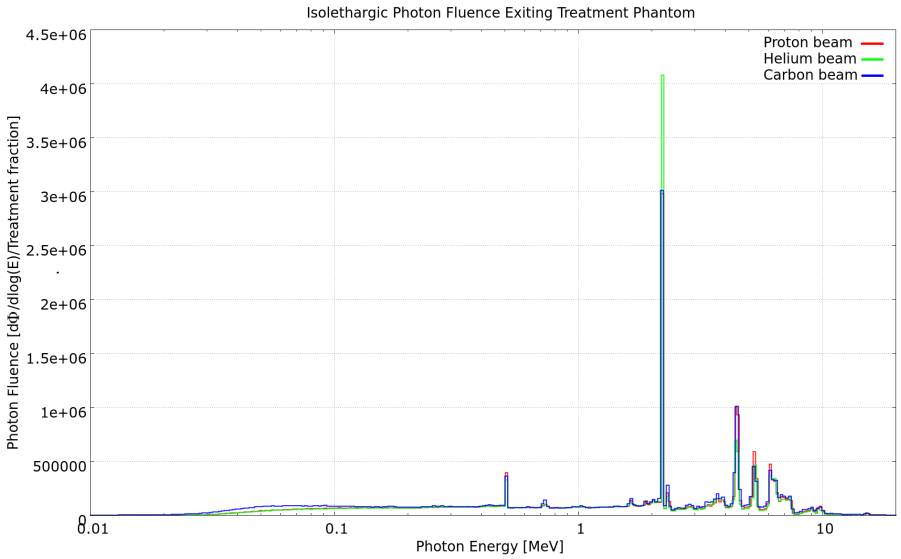

(a) Isolethargic differential fluence spectrum over photons exiting the patient phantom in the forward direction. Error-bars are omitted completely from the figure for the sake of readability as they are too small to be effectively read

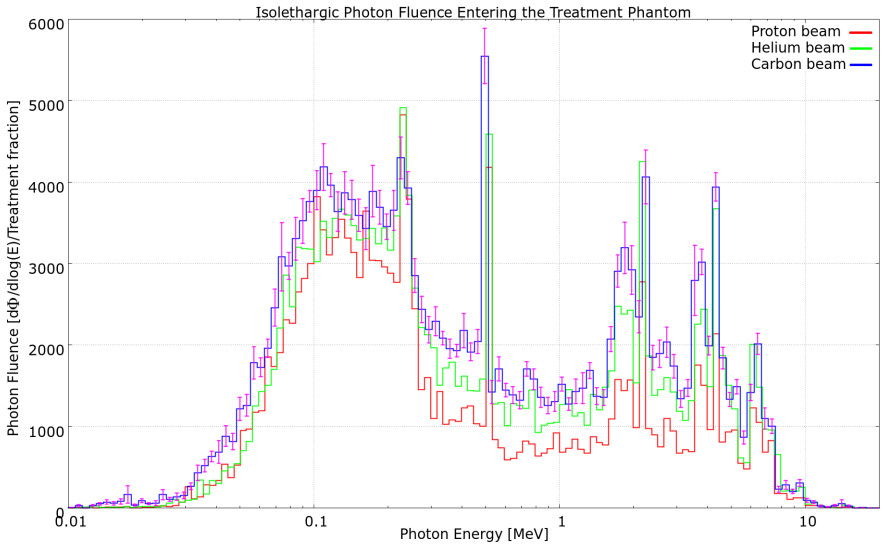

(b) Isolethargic differential fluence spectrum of photons entering the back-side of the patient phantom.

Figure 7.7: Panel (a) show the energy distribution of photons exiting the patient phantom and panel (b) show the energy distribution of photons entering the patient phantom.

RightMaze and RightMazeBoron

The two simulation setups *"RightMaze"* and *"RightMazeBoron"* were designed to yield information about the secondary particle and dose production in a region around around an entrance maze with and without the presence of boron layers for shielding purposes. Simulation setup *"RightMaze"* contains a maze made only of concrete, a two-dimensional layout drawing can be studied in appendix C.0.3, figure C.3. The simulation setup *"RightMazeBoron"* (two-dimensional layout drawing can be studied in appendix C.0.4, figure C.0.4) includes two 10cm

thick boron layers located in each of the two inner maze arms. Besides the boron shielding, the two simulation setups are identical. Three water phantoms (Worker1-3) were placed inside the maze next to each of the three maze arms, while a fourth (Worker4) was placed outside the last arm of the maze. Effective doses were scored in each of these phantoms and visualised as two a bar charts in figure 7.8. Panel (a) displays the effective dose to worker1-4 in simulation *"RightMaze"* and panel (b) in *"RightMazeBoron"*.

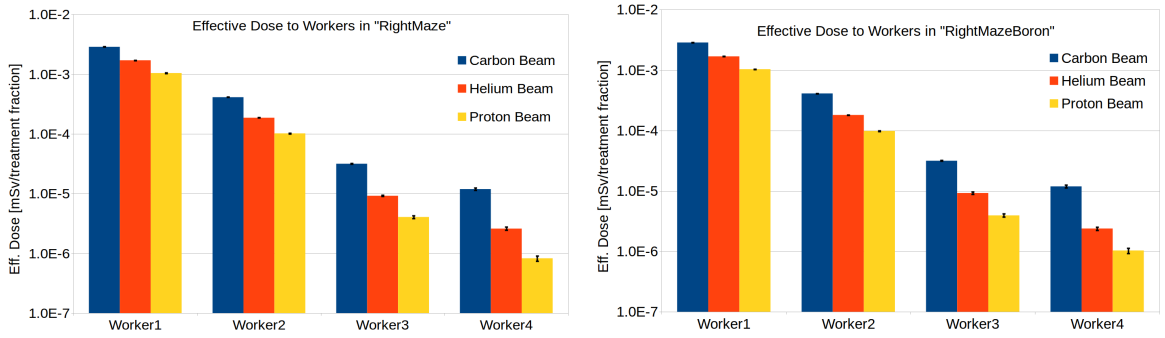

(a) Bar Chart Illustrating Effective Dose to Workers1-4 in simulation *"RightMaze"*

(b) Bar Chart Illustrating Effective Dose to Workers1-4 in simultion *"RightMazeBoron"*

Figure 7.8

Additionally, a fluence detector covering the entirety of the maze and scoring the fluence of neutrons, photons and protons was placed and the results plotted in order to gain insight into the effect of the boron layers on the neutron fluence, and simultaneously observe how particles, especially neutrons and photons, behaved inside the maze. Differential isolethargic fluence plots of secondary neutrons and photons entering the maze hallway is approximately identical in both simulation setups and are therefore only plotted for the *"RightMaze"* setup in figure 7.9. Panel (a) shows the neutron spectrum and panel (b) the photon spectrum entering the maze hallway. The isolethargic differential fluence and two-dimensional fluence plots of neutrons and photons exiting and travelling through the maze hallway for the two simulation setups are presented in figures 7.10 and 7.11 respectively. A decrease in the number of neutrons and photons exiting the maze hallway with boron layers are noted.

The same quantities are plotted for protons entering and exiting the maze hallway and are shown in figure 7.12. The results of protons, and to an extent, the heavier ions exiting the maze hallway, show little activity and this is observed to the same degree in all other simulation setups presented in this thesis. Fluence plots of secondary protons and heavier ions are therefore omitted and only fluence plots concerning secondary neutrons and photons will be presented in the coming simulation results.

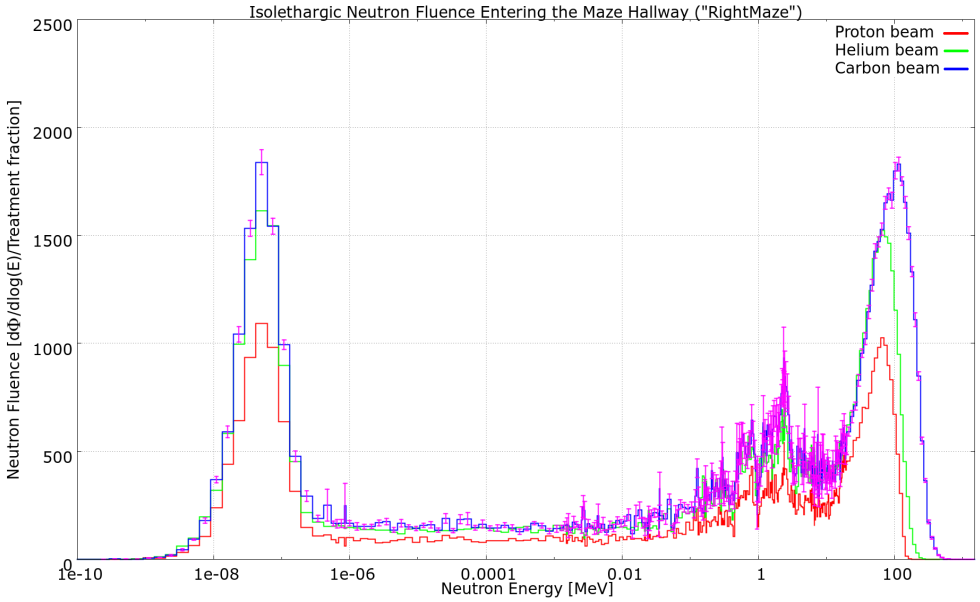

(a) Differential isolethargic fluence plot of secondary neutrons entering the maze hallway in *"RightMaze"*.

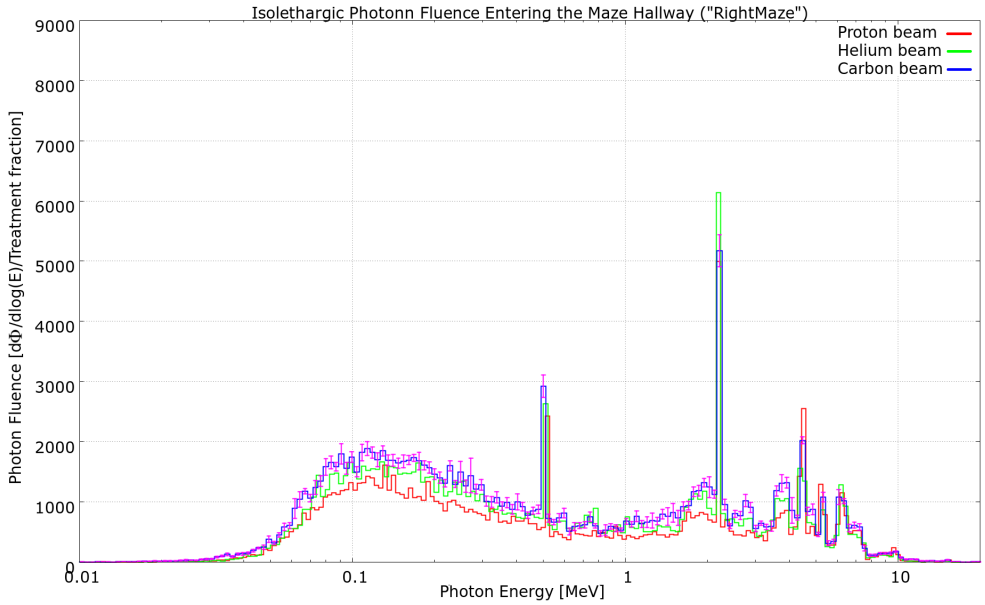

(b) Differential isolethargic fluence plot of secondary photons entering the maze hallway in *"RightMaze"*.

Figure 7.9

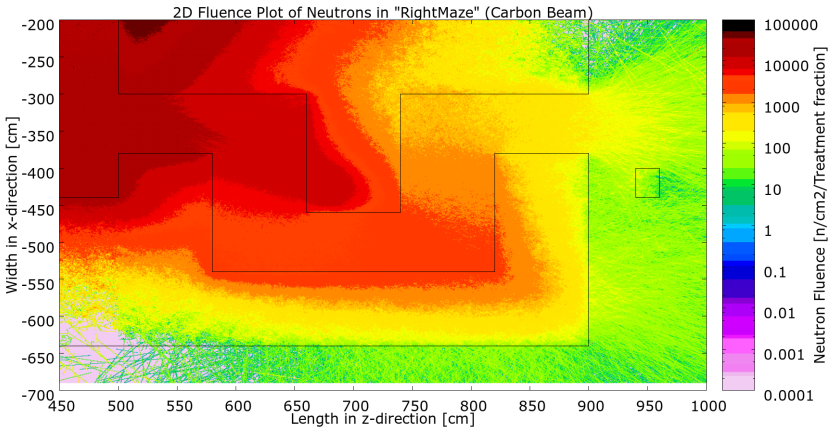

(a) Two-dimensional fluence plot of secondary neutrons inside the maze in simulation setup *"RightMaze"* when the carbon beam is applied.

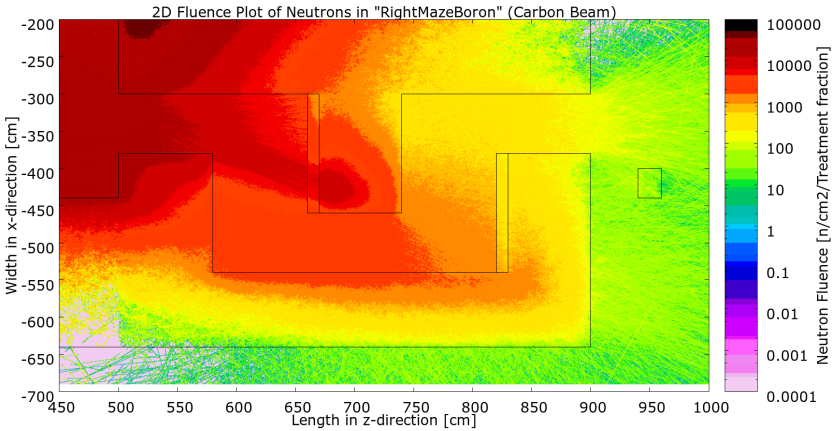

(b) Two-dimensional fluence plot of secondary neutrons inside the maze in simulation setup *"RightMazeBoron"* when the carbon beam is applied.

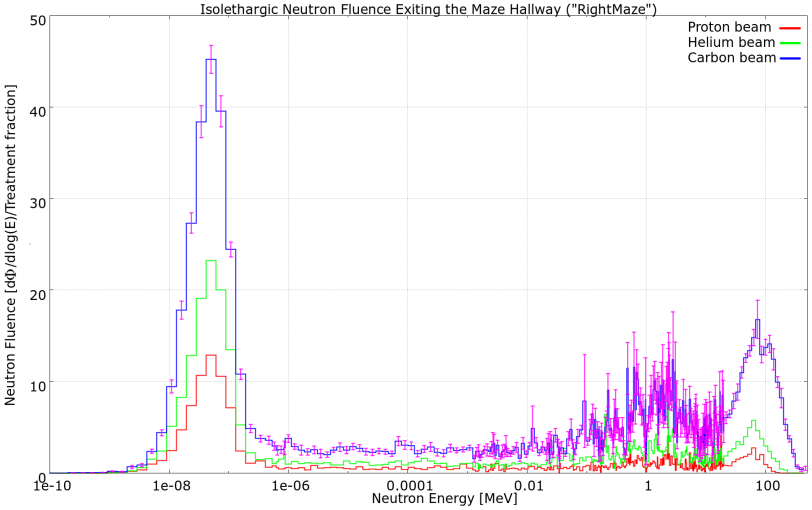

(c) Isolethargic differential fluence plot of secondary neutrons exiting the maze hallway in simulation setup *"RightMaze"*.

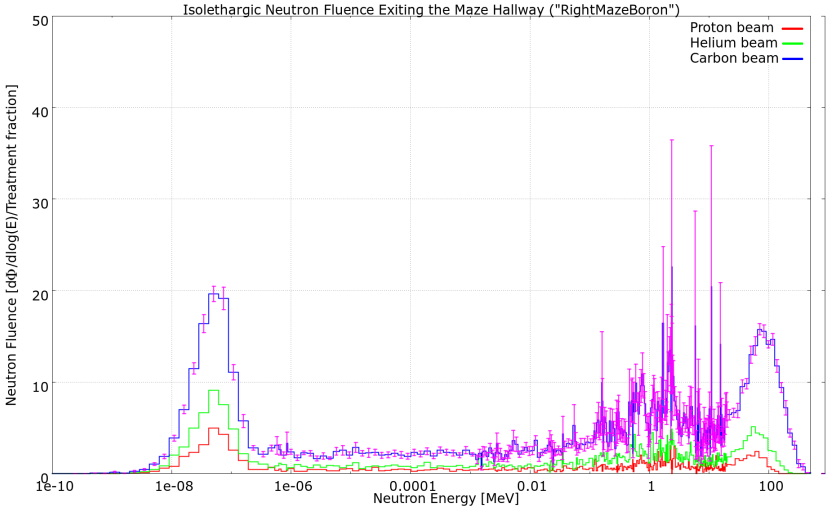

(d) Isolethargic differential fluence plot of neutrons exiting the maze hallway in simulation setup *"RightMazeBoron"*.

Figure 7.10

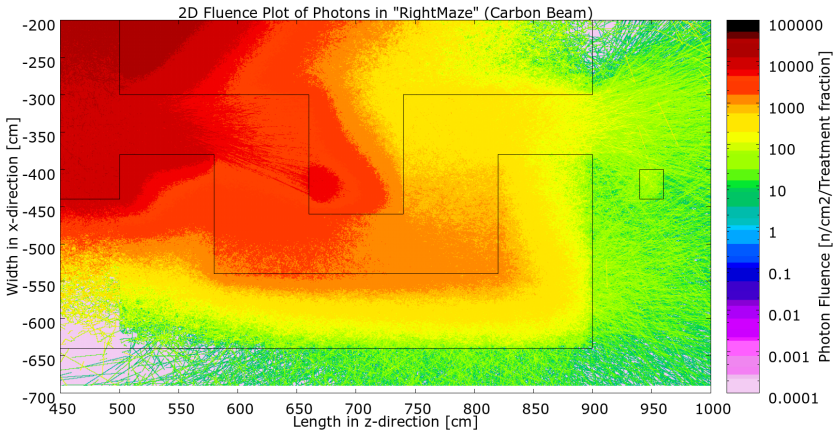

(a) Two-dimensional fluence plot of photons inside the maze in simulation setup *"RightMaze"* when the carbon beam is applied.

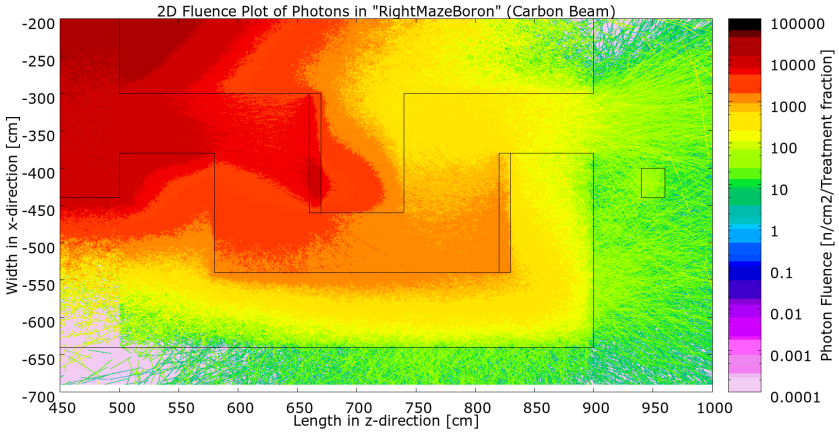

(b) Two-dimensional fluence plot of photons inside the maze in simulation setup *"RightMazeBoron"* when the carbon beam is applied.

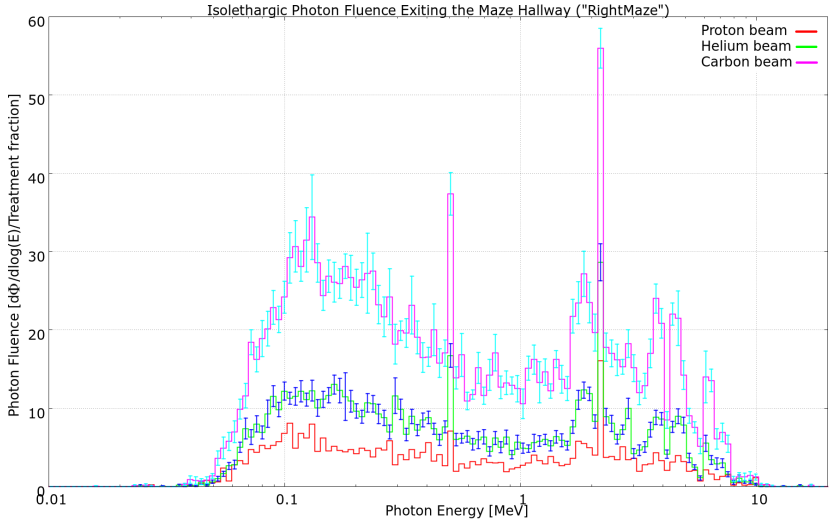

(c) Isolethargic differential fluence plot of neutrons exiting the maze hallway in simulation setup *"RightMaze"*.

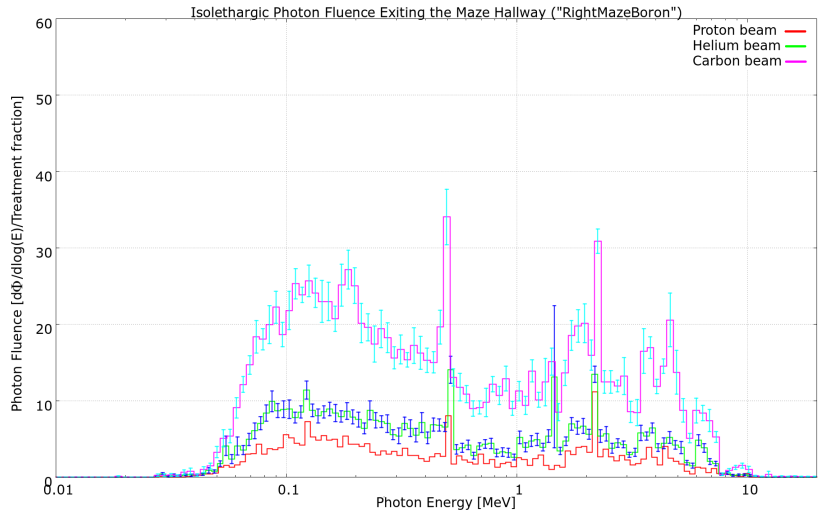

(d) Isolethargic differential fluence plot of neutrons exiting the maze hallway in simulation setup *"RightMazeBoron"*.

Figure 7.11

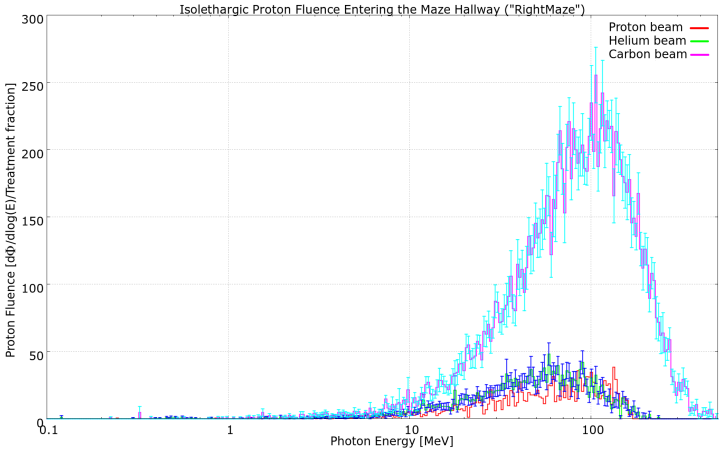

(a) Isolethargic differential fluence spectrum of protons entering the maze hallway in simulation setup *"RightMaze"*.

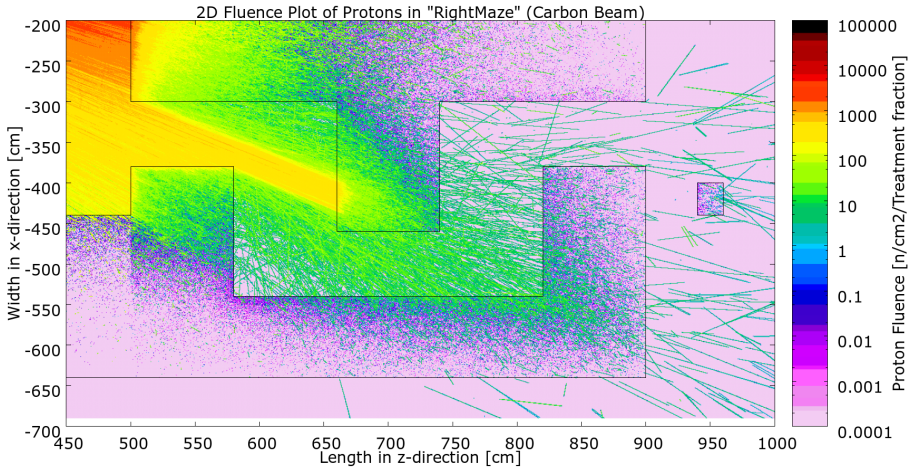

(b) 2-dimensional fluence plot of protons inside the maze in simulation setup *"RightMaze"* when the carbon beam is applied.

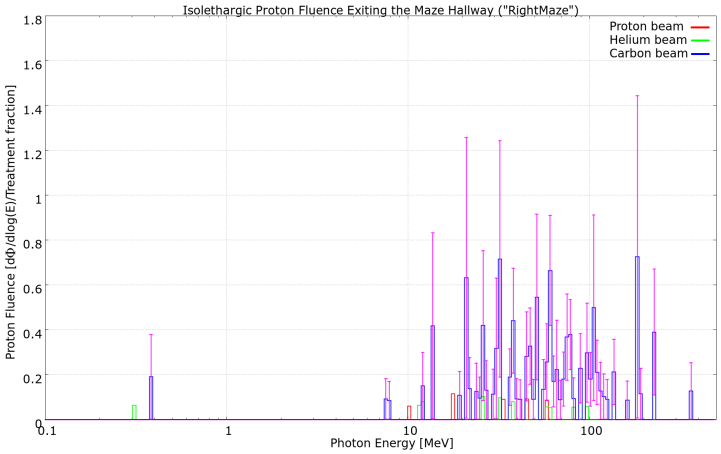

(c) Isolethargic differential fluence plot of protons exiting the maze hallway in simulation setup *"RightMaze"*.

Figure 7.12

MiddleMaze

The last simulation concerning a maze functioning as an entrance (*"MiddleMaze"*) is centred around a maze with the same dimensions as the maze found in *"RightMaze"*, but is instead placed in the middle of the right flank wall of the treatment room (layout drawing is found in appendix C.0.5). The same water phantoms (Worker1-4) were placed at similar locations inside the maze and consequently scored for effective dose while irradiating the patient phantom with protons, helium and carbon ions. The results are illustrated as a bar chart in figure 7.13 below and detailed results and error bars associated with the effective doses are gathered in appendix F, table F.1.

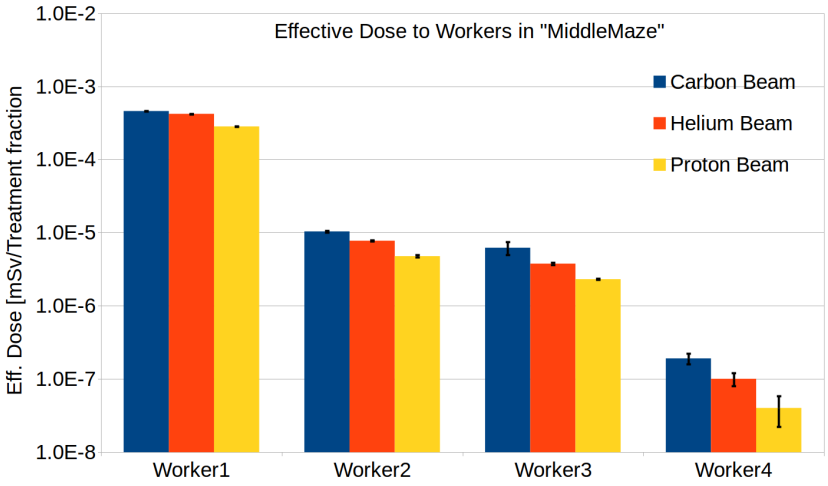

Figure 7.13: Bar chart showing the effective dose [mSv/treatment fraction] to worker1-4 located inside and outside the maze.

Isolethargic differential fluence plots of secondary neutrons and photons entering and exiting the maze hallway together with two-dimensional fluence plots inside the maze are found in figure 7.14 and figure 7.15 for neutrons and photons respectively. Error bars are plotted for the carbon beam and the others are omitted for the sake of readability, but the error bars for helium and protons are of the same order, except for the single 155MeV proton spike where the y-axis error is ± 1000.

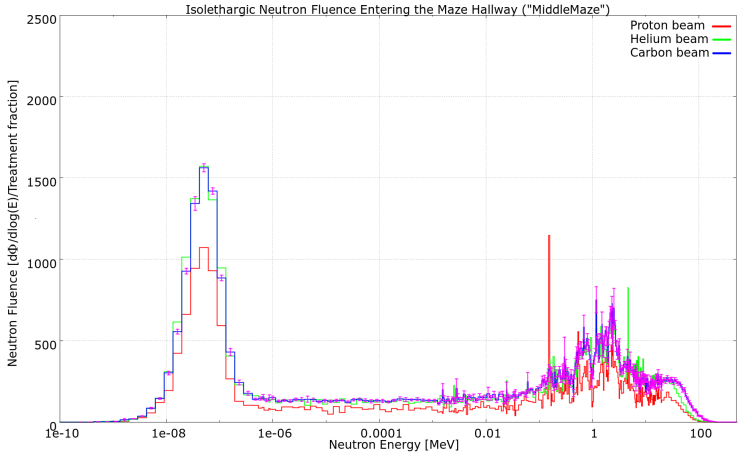

(a) Isolethargic differential fluence spectrum of neutrons entering the maze hallway in simulation setup *"MiddleMaze"*.

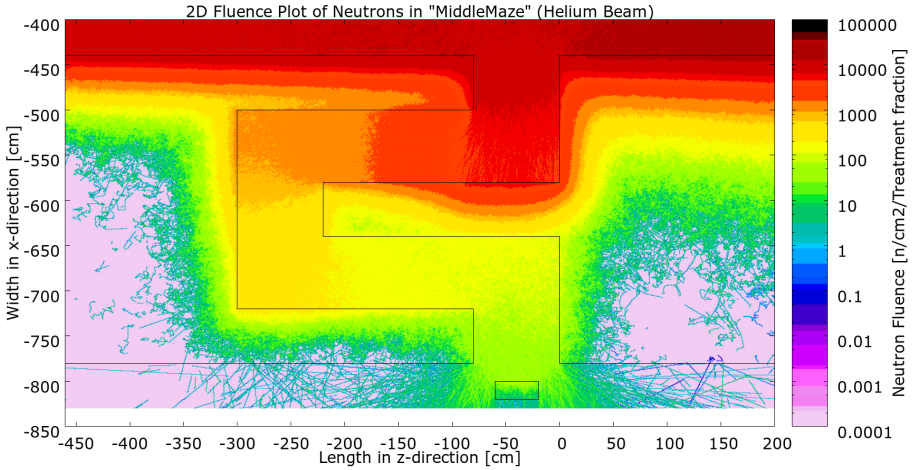

(b) 2-dimensional fluence plot of neutrons inside the maze in simulation setup *"MiddleMaze"* when the helium beam is applied.

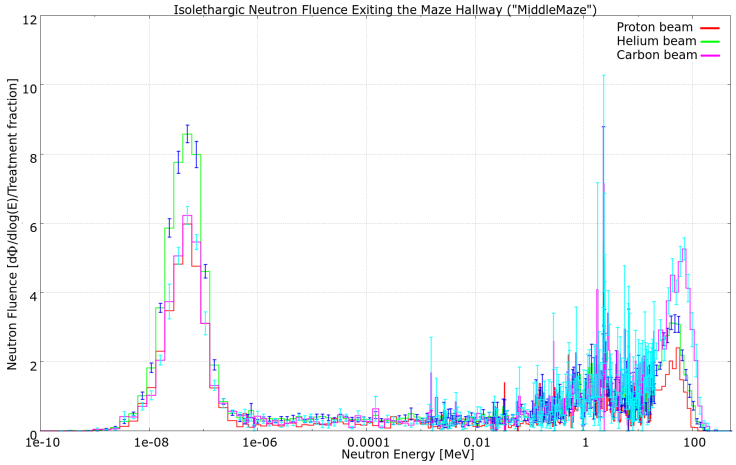

(c) Isolethargic differential fluence spectrum of neutrons exiting the maze hallway in simulation setup *"MiddleMaze"*.

Figure 7.14

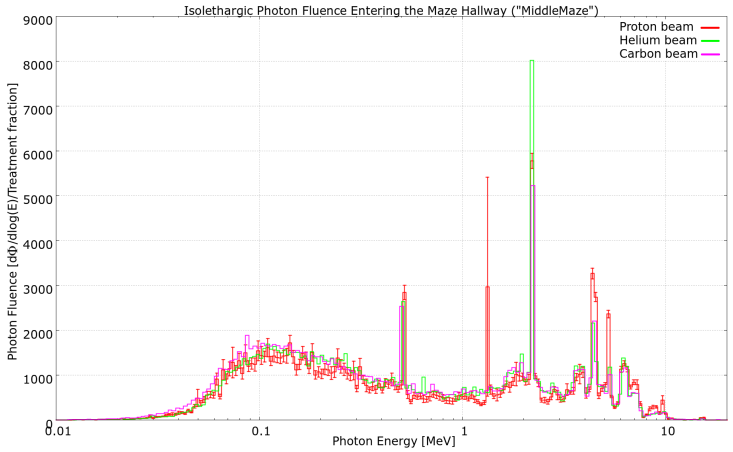

(a) Isolethargic differential fluence spectrum over neutrons entering the maze hallway in simulation setup *"MiddleMaze"*.

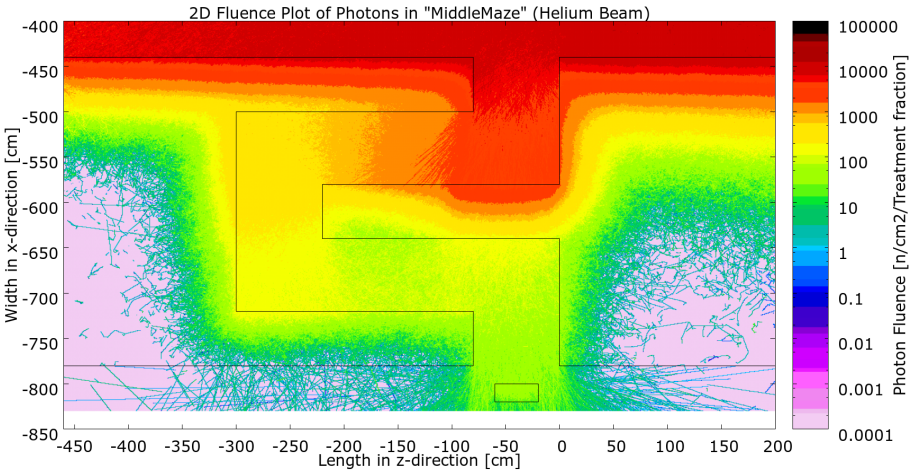

(b) 2-dimensional fluence plot of photons inside the maze in simulation setup *"MiddleMaze"* when the helium beam is applied.

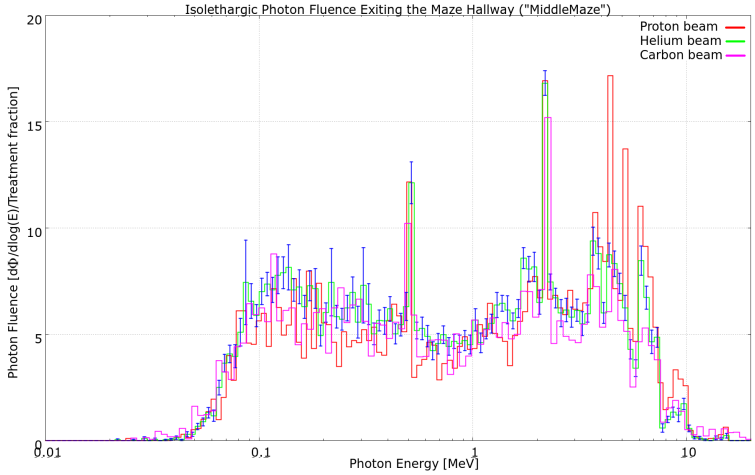

(c) Isolethargic differential fluence spectrum of photons exiting the maze hallway in simulation setup *"MiddleMaze"*.

Figure 7.15

MiddleDoor

A simulation setup connected to the *"MiddleMaze"*, but instead of a maze, a corridor with a 100cm thick iron door in the middle is placed inside the right flank wall of the treatment room (layout drawing is seen in figure **??**, appendix C.0.6). Two water phantoms (Worker3 and Worker4) were placed at two locations on the other side of this flank wall, one close to the door and one further away. The effective doses to these phantoms are found in table F.1 in the appendix F and illustrated as a bar chart in figure 7.16.

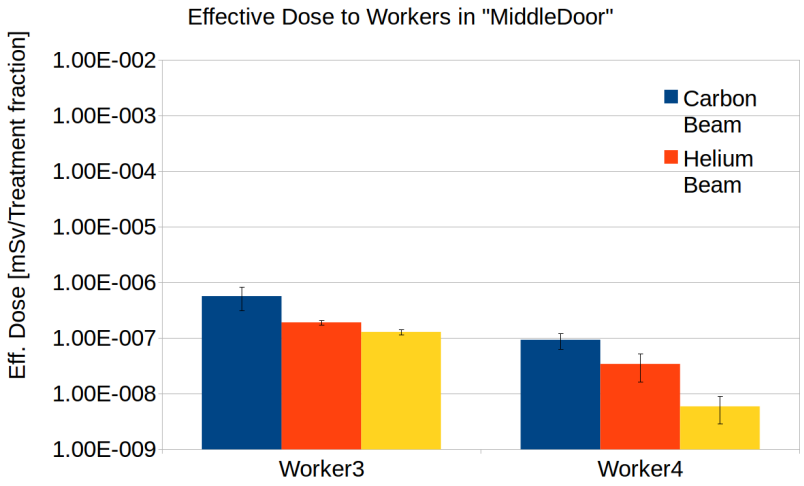

Figure 7.16: Bar chart showing the effective dose [mSv/treatment fraction] to worker3 and 4 located on the outside of the treatment room.

Isolethargic differential fluence spectrum of neutrons and photons entering and exiting the corridor, together with two-dimensional fluence plots of neutrons and photons inside and around the corridor are found in figures 7.17 and 7.18 respectively.

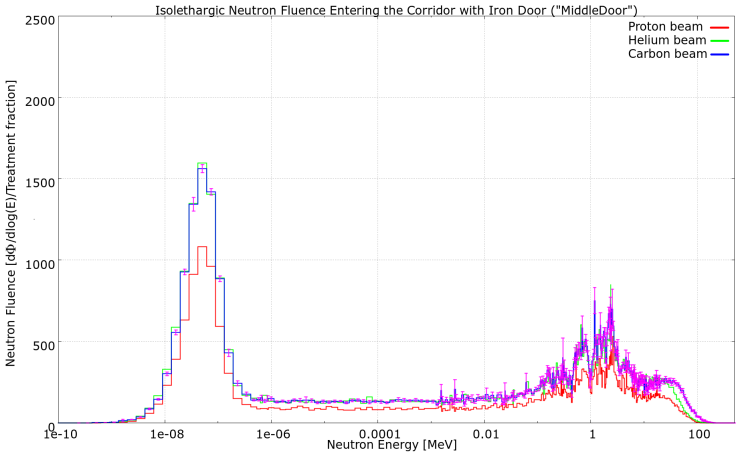

(a) Isolethargic differential fluence spectrum over neutrons entering the corridor in simulation setup *"MiddleDoor"*.

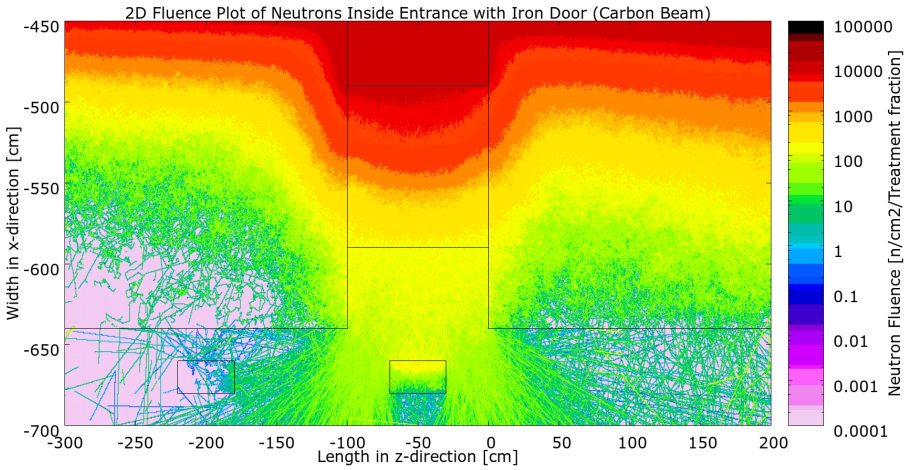

(b) Two-dimensional fluence plot of neutrons inside the corridor in simulation setup *"MiddleDoor"* when the carbon beam is applied.

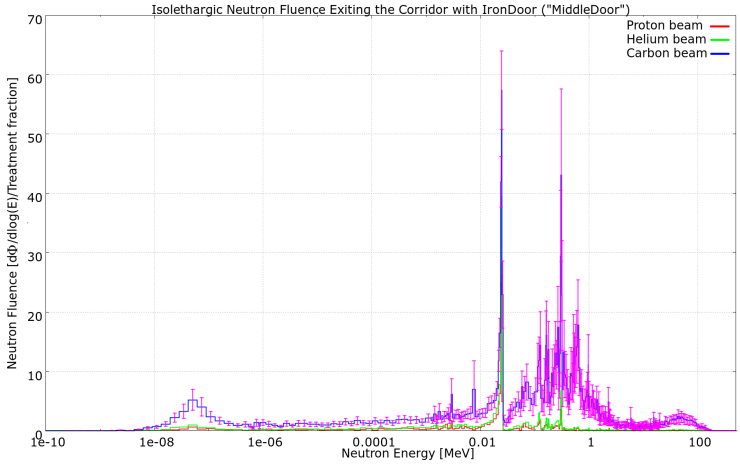

(c) Isolethargic differential fluence spectrum of neutrons exiting the corridor in simulation setup *"MiddleDoor"*.

Figure 7.17

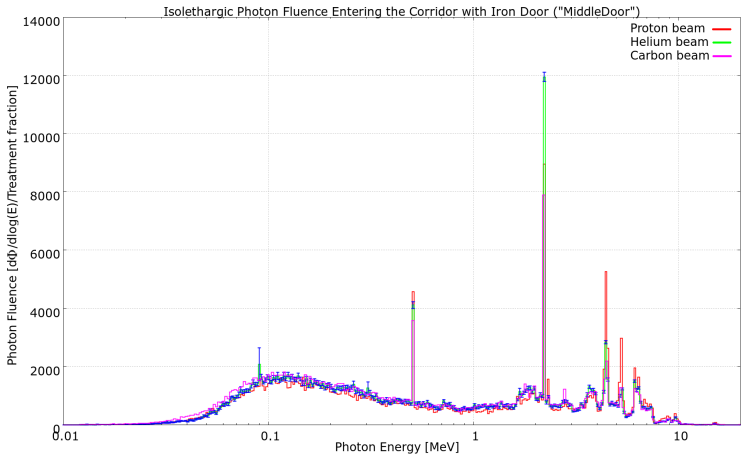

(a) Isolethargic differential fluence spectrum over photons entering the corridor in simulation setup *"MiddleDoor"*.

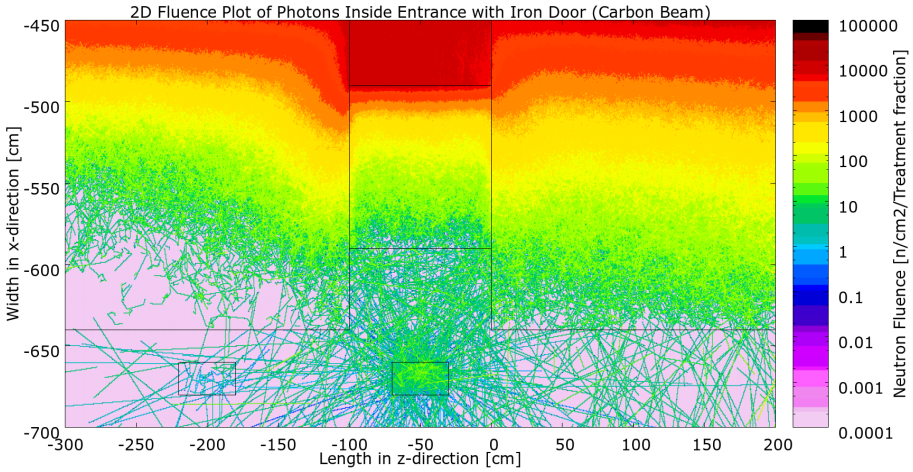

(b) Two-dimensional fluence plot of photons inside the corridor in simulation setup *"MiddleDoor"* when the carbon beam is applied.

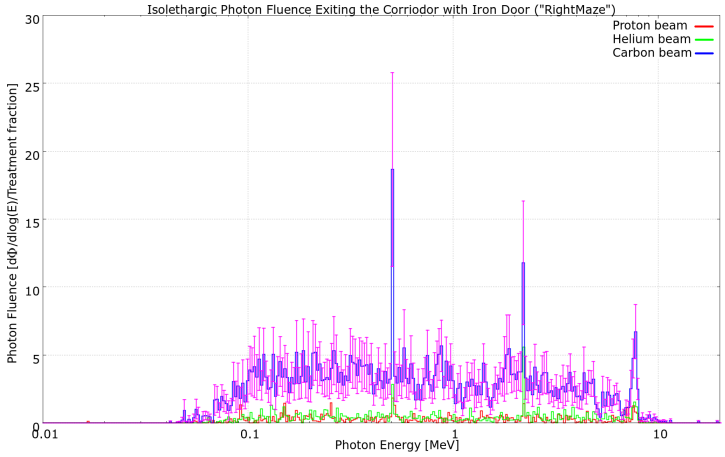

(c) Isolethargic differential fluence spectrum of photons exiting the corridor in simulation setup *"MiddleDoor"*.

Figure 7.18

PrimaryBarrier

A simulation focused entirely on the primary barrier was performed (layout drawing is found in figure C.7, appendix C.0.7), where a single water phantom (Worker4) was placed 50cm from the concrete wall in the central beam axis outside the treatment room for the sake of measuring the resulting effective dose while irradiating the patient phantom with proton, helium and carbon respectively, the results are shown in the bar chart in figure 7.19.

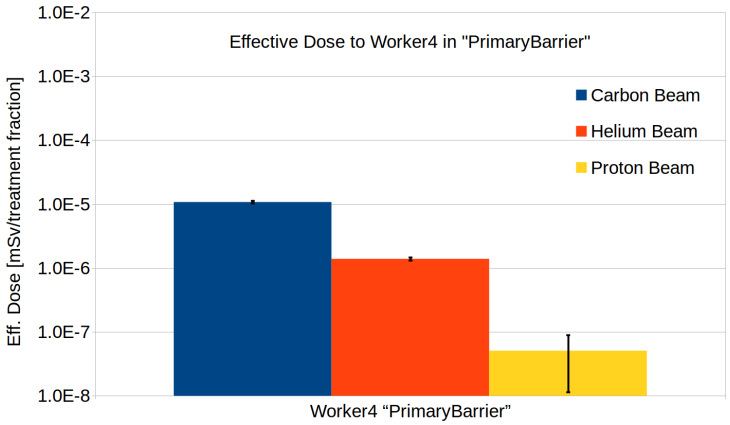

Figure 7.19

Due to their penetrative properties, neutron and photon fluence plots, in both one- and two-dimensions, together with isolethargic differential fluence plot of neutrons and photons exiting the primary barrier, were scored and shown in figure 7.20 and 7.21 for neutrons and photons respectively. $A 50cm \times 50cm$ projection limit in x- and y-direction centred around the isocenter was chosen in the one dimensional fluence plots in order to focus on the the maximum fluence within the barrier. In all two dimensional plots, a 100cm thick y-projection slice, centred around the isocenter and thus covering the maximum fluence, was chosen.

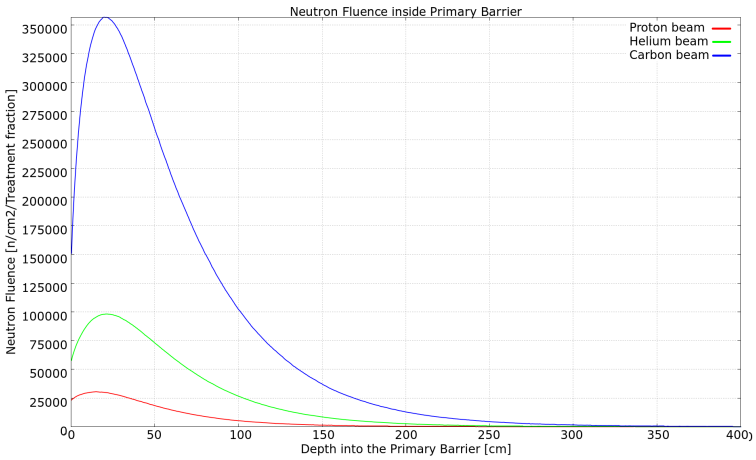

(a) Neutron fluence plotted in 1-dimension with respect to the primary barrier depth (*"PrimaryBarrier"*).

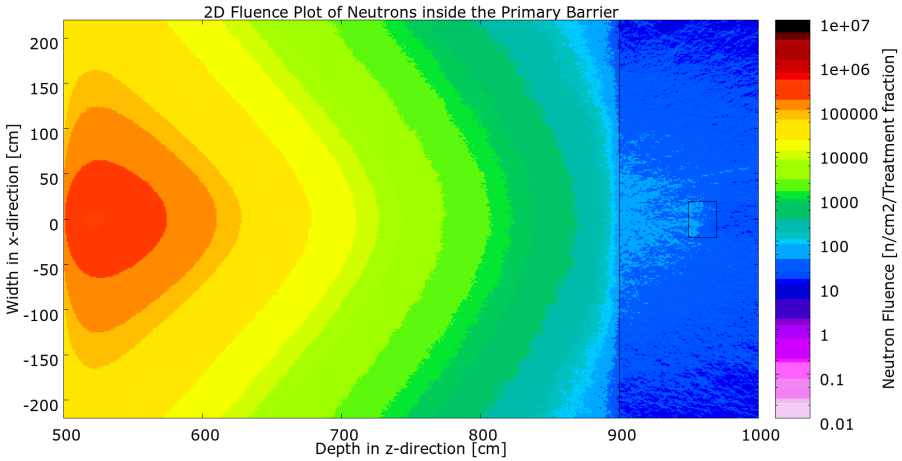

(b) Two-dimensional fluence plot of neutrons inside the primary barrier in simulation setup *"PrimaryBarrier"* when the carbon beam is applied.

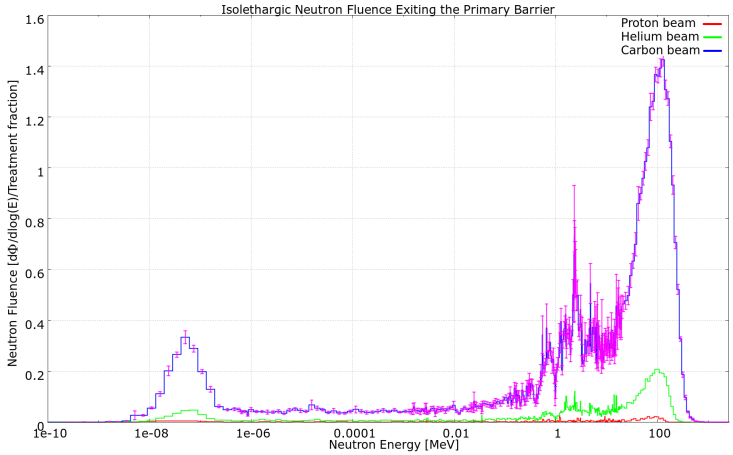

(c) Isolethargic differential fluence spectrum of neutrons exiting the primary barrier in simulation setup *"PrimaryBarrier"* for each of the three treatment beams.

Figure 7.20

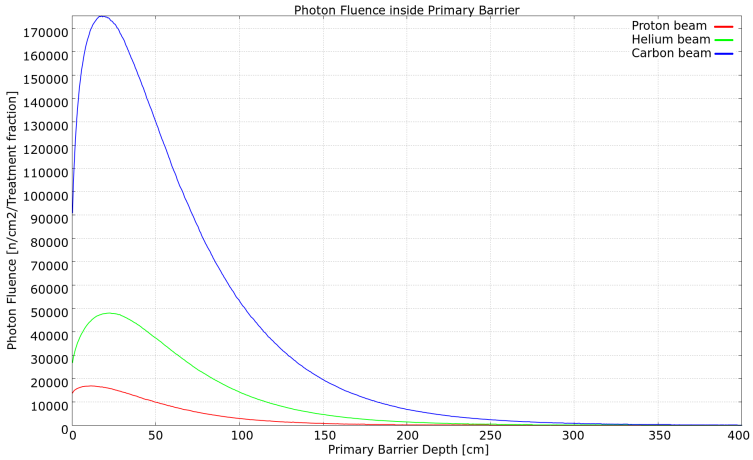

(a) Photon fluence plotted in one-dimension with respect to the primary barrier depth (*"PrimaryBarrier"*).

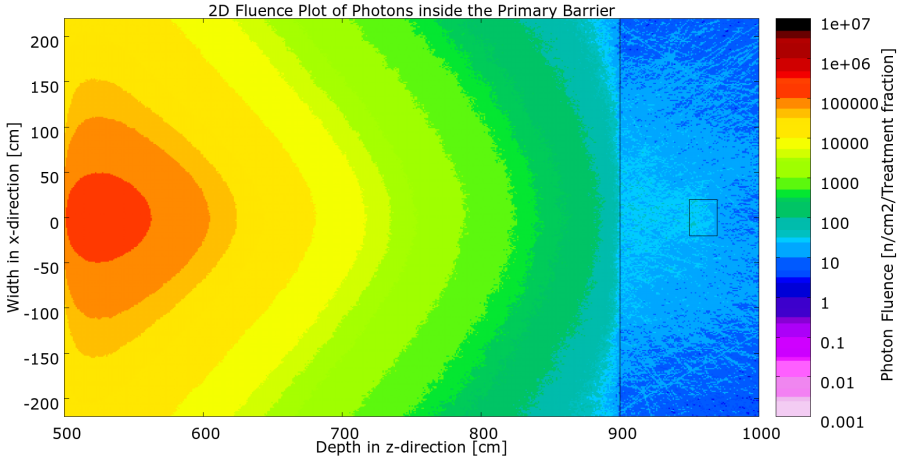

(b) Two-dimensional fluence plot of photons inside the primary barrier in simulation setup *"PrimaryBarrier"* when the carbon beam is applied.

(c) Isolethargic differential fluence spectrum of photons exiting the primary barrier in simulation setup *"PrimaryBarrier"* for each of the three treatment beams.

Figure 7.21

BeamDump

The last simulation aimed at the primary barrier focused on a beam dump aspect (*"BeamDump"*, layout drawing is found in figure C.8, appendix C.0.8. The two main differences between this simulation and *"PrimaryBarrier"* is the absence of a patient phantom, and the inclusion of a 30cm steel layer covering the first 30 centimetres of the primary barrier. Similarly as in the *"PrimaryBarrier"* simulation, a single water phantom (Worker4) was placed outside the room on the opposite side of the primary barrier in order to measure the effective dose shown in figure 7.22.

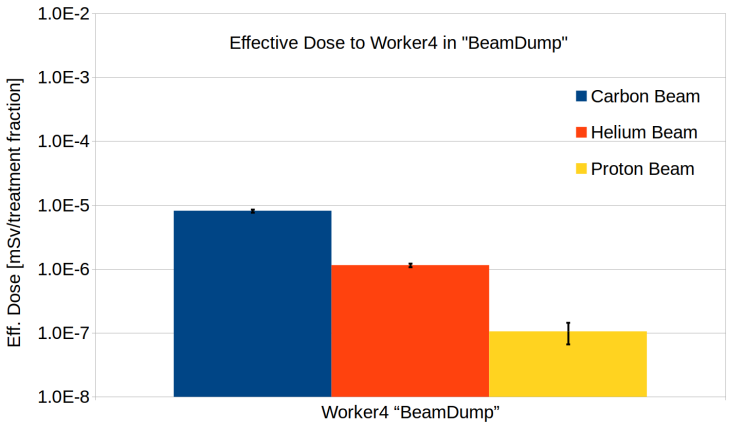

Figure 7.22: Effective dose to Worker4 in *"BeamDump" simulation* [mSv/Treatment fraction]

Fluence plots in one- and two-dimensions, together with isolethargic differential fluence plots of neutrons and photons exiting the primary barrier, were scored and shown in figure 7.23 and 7.24 respectively. Same as in the *"PrimaryBarrier"* setup, a $50cm \times 50cm$ projection limit in x- and y-direction centred around the isocenter was chosen in the one dimensional fluence plots and in all two dimensional plots, a 100cm thick y-projection slice centred around the isocenter was chosen.

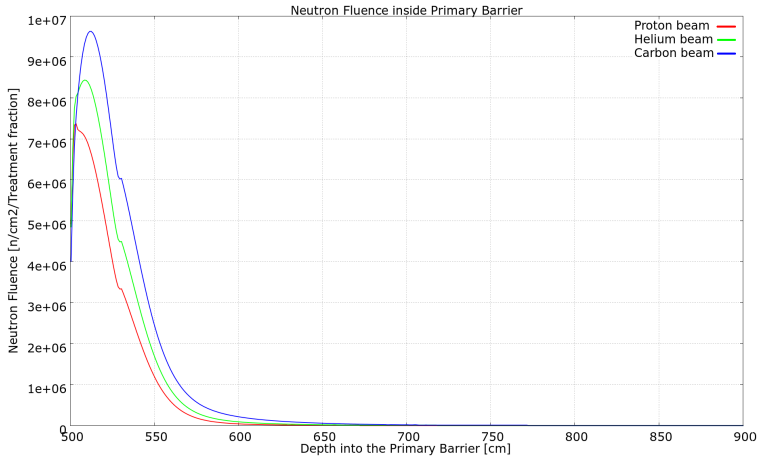

(a) Neutron fluence plotted in one-dimension with respect to the primary barrier depth (*"BeamDump"*).

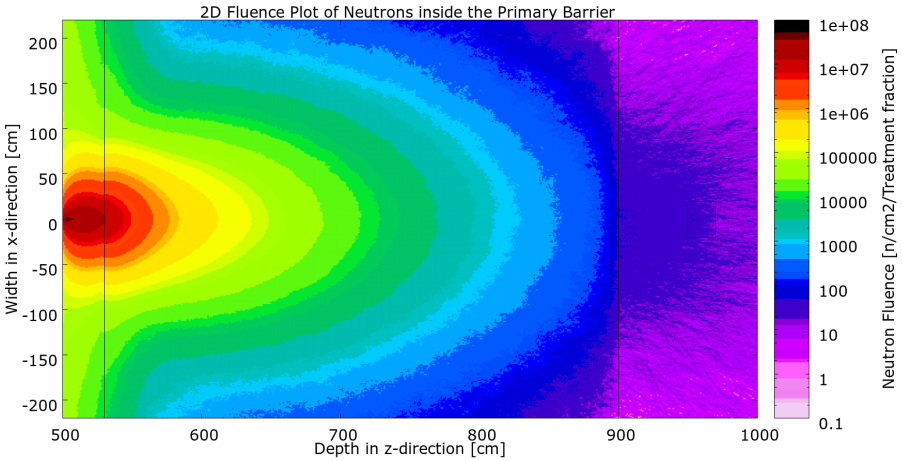

(b) two-dimensional fluence plot of neutrons inside the primary barrier in simulation setup *"BeamDump"* when the carbon beam is applied.

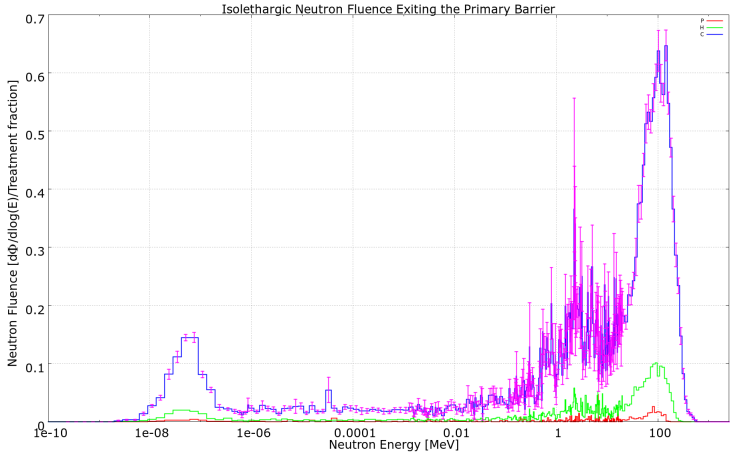

(c) Isolethargic differential fluence spectrum of neutrons exiting the primary barrier in simulation setup *"BeamDump"* for each of the three treatment beams.

Figure 7.23

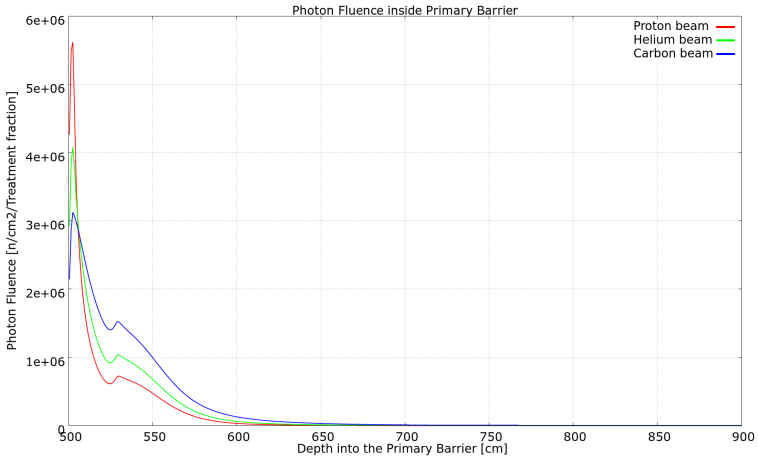

(a) Photon fluence plotted in one-dimension with respect to the primary barrier depth (*"BeamDump"*).

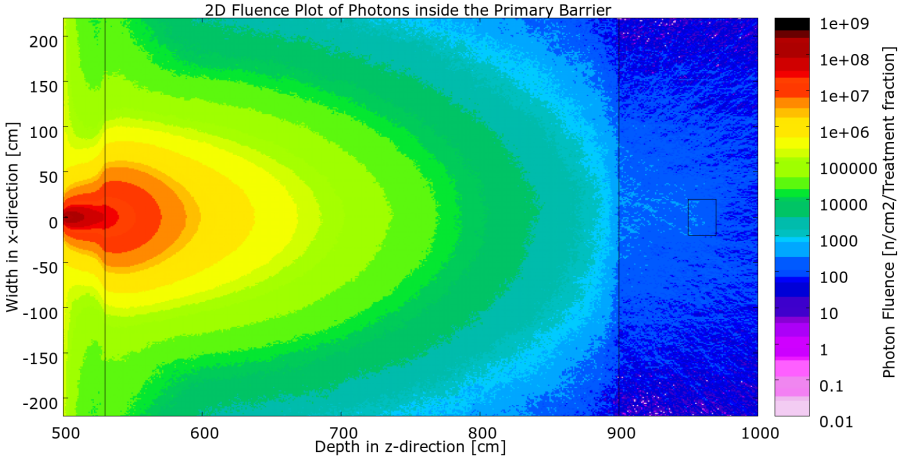

(b) Two-dimensional fluence plot of photons inside the primary barrier in simulation setup *"BeamDump"* when the carbon beam is applied.

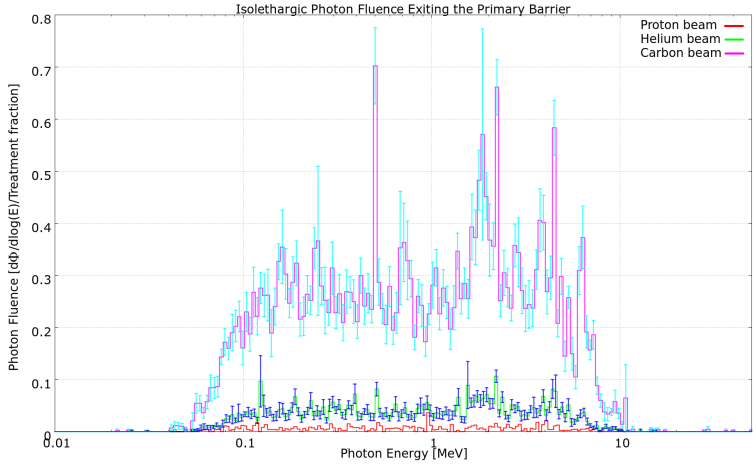

(c) Isolethargic differential fluence spectrum of photons exiting the primary barrier in simulation setup *"BeamDump"* for each of the three treatment beams.

Figure 7.24

7.5 Annual Dose to Outside Workers

In each simulation, one or two worker phantoms were placed outside the treatment room. Worker3 was typically placed inside or close to the entrance of the geometrical structure of interest and Worker4 was located outside and behind walls. Exact positions are shown in the respective appendix C sections. Each of these two workers had an effective dose scoring detector associated with them. FLUKA calculates these by using its integrated fluence conversion factors based on the 2007 ICRP recommendations. These effective dose measurement were used in calculations of the workers *anual dose*, based on an assumption that a single treatment room would be used for 25 treatments (each delivering a physical dose of 2Gy) per day, 235 days per year. The effective dose each phantom receives per year [mSv/year] in each simulation setup is calculated and presented in table 7.6 below.

Table 7.6: Calculated annual dose to Workers outside the treatment room for each treatment beam in each individual simulation setup.

Simulation Setup	Particle Type	Workload to Worker3 [mSv/year]	Workload to Worker4 [mSv/year]
RightMaze	Proton	0.024±0.001	0.005±5.0E-4
	Helium	0.054±0.001	0.015±9.7E-4
	Carbon	0.186±0.003	0.07±0.0035
RightMazeBoron	Proton	0.023±0.001	0.006±6.1E-4
	Helium	0.054±0.002	0.014±8.5E-4
	Carbon	0.186±0.003	0.07±0.003
MiddleMaze	Proton	0.01±7.6E-4	Not Present
	Helium	0.02±5.3E-4	
	Carbon	0.03±0.001	
MiddleDoor	Proton	7.6E-4±7.9E-5	3.5E-5±1.8E-5
	Helium	0.001±1.1E-4	2.0E-4±1.0E-4
	Carbon	0.003±0.0015	5.5E-4±1.7E-4
PrimaryBarrier	Proton	Not Present	3.0E-4±2.3E-4
	Helium		0.008±4.2E-4
	Carbon		0.06±0.003
BeamDump	Proton	Not Present	6.21E-4±1.5E-4
	Helium		0.007±8.3E-4
	Carbon		0.05±1.6E-3

Chapter 8

Discussion and Outlook

Precise estimates and calculations of induced secondary particles with its associated generation of unwanted dose to the patient and hospital personnel is a key element in the planning stages for a particle therapy facility. The motivation for this master thesis work is to obtain generic, but precise, information about the radiation environment in the main area for such dose production, in the treatment room and in the entrance area and corridors surrounding this.

The focus of this master thesis work has been to perform comparative studies of the secondary dose production while irradiating a phantom patient with a standard physical dose (2Gy) from protons, helium and carbon ions. Studies of different, realistic, geometries and locations for the entrance part of the treatment room. By placing water equivalent phantoms representing hospital personnel at several positions in the treatment room entrance region and scoring the effective dose to these phantoms, estimates of the dose received to these positions during a treatment fraction and during a treatment year, with some assumptions concerning the number of fractions per year, can be applied to further investigate and improve the design; shapes, barrier thickness, relative positioning and overall layout of the treatment facility.

Studies of the secondary particles produced when high energetic nuclear particles in the treatment beam interacts with matter were performed and followed up by differential fluence studies of neutrons and photons entering and exiting the featured geometrical structures in order to chart the dose environment during irradiation. The FLUKA Monte Carlo Simulation code allows the creation of relatively comprehensive and realistic treatment room geometries that can incorporate different types of entrance geometries and primary shielding barriers. Emphasis has been put on the radiation environment in three positions inside a standard entrance maze, both with and without layers of boron for additional neutron shielding, located inside the two inner maze arms. And a third maze of identical proportions placed inside the flank wall. A straight corridor geometry with an iron door in the middle, placed in the flank wall of the treatment room was also defined and studied, before introducing a steel layer to the primary barrier and performing a beam dump.

Three different treatment beams made of protons, helium and carbon ions were created to cover a Target Volume inside a patient phantom via an active energy modulation scheme as presented in chapter 7, section 7.1. The dose plateau of the SOBPs were designed in order to be sufficiently flat and no additional attempts at optimizing the treatment plans outside the dose coverage were made. The dose coverage and the delivery of a physical dose of 2 Gy to the Target Volume was applied as the normalization between the three treatment particle types and the dose coverages obtained were estimated to be satisfactory for the purposes and intentions of this comparative study. However, it is quite important to note that the higher RBE of helium and carbon ions, with respect to the biological efficiency of protons, are not accounted for and this effectively increased the number of treatment particles to a higher number than what would otherwise be the case in a clinical setting. The main reason for working with physical dose is that it would be outside of the scope of this thesis project to introduce modelling of biological doses to tissue, as this is still a quite open field with relatively large uncertainties associated with the models applied for quantification of the biological effect from particle therapy. However, from a radiation shielding point of view, the number of helium and carbon ions applied in this work can be thought of as a "worst"case scenarios and is considered as such.

A total of 24 simulation setups covering eight different treatment room layouts for each of the three treatment particles were constructed with flair and performed with application of the FLUKA Monte Carlo simulation tool. The additional dose to the patient phantom from the concrete walls surrounding the treatment room was studied in the simulations named *"Closed-Room"* and the precense of the walls yielded a small, $< 1\%$, increase in the photon and neutron fluence inside the patient phantom when scoring the fluence during irradiation with and without the walls present. However, no noticeable increase in the dose to the patient phantom was observed. Secondary neutrons, photons, and charged particles produced through interactions between the patient phantom and proton, helium, and carbon beams respectively, was observed to contain secondary particles with energies up to the initial beam energy. Due to the fragmentation and the considerably higher initial beam energy of the carbon beam, with 12 nucleons carrying the kinetic energy required to reach the same depth as the single protons and the helium ions, the largest amount of secondary neutrons, photons, protons and heavier ions were produced during carbon ion irradiation of the Target Volume. At the same time, during carbon ion irradiation, attaining the widest energy spectrum when compared to the helium and proton beam spectra. This implies that the scaling of the radiation shielding in a treatment room where proton, helium, and carbon ion beams will be applied, must have its origin in shielding towards carbon ion induced secondary particle production in order to ensure adequately shielding. Generally, it is observed that neutrons and photons are the particles with the largest penetrative power. Neutrons and photons exit the treatment room in high numbers compared to charged particles like protons and heavier secondary ions. Due to this, differential neutron- and photon fluence scoring layers were placed at entrances and exits of

the studied geometries.

The obtained results for the effective doses to water phantoms displayed little variation between the different simulation setups. Of the four different entrances, the 100cm thick iron door (*"MiddleDoor"*) located in the right flank wall, yielded the least amount of effective dose to a worker located on the outside of the door. Concurrently, the maze (*"MiddleMaze"*) located at the same position, resulted in the least amount of dose when compared to the two mazes located inside the primary barrier. These results lead to the observation that there is a clear benefit of locating the entrance to a treatment room in the perpendicular direction with respect to the beam line direction. This is observation is supported by the what one will find when collecting information based upon several particle therapy facility layout drawings. Differential fluence spectra of neutrons entering a hallway placed inside a flank wall, when compared to a hallway inside the primary barrier, showed significantly fewer fast neutrons and thus effectively lessening the shielding burden and dose deposition. For all the different simulation geometry setups, the annual effective doses to worker phantoms located in different positions outside the treatment room, were obtained. The annual effective doses to these worker phantoms were found to be several orders of magnitude lower than the annually allowed dose of 1mSv to the public and, more importantly, the obtained effective doses are far lower than the annually allowed dose of 20 mSv to the personnel working at a radiation treatment facility.

The possibility of optimizing the geometry, material compositions, thicknesses, sizes and relevant positioning of beam the line area, the treatment rooms, the patient area and the workflow for the personnel at a particle therapy facility through Monte Carlo Simulations is very important. The results from the Monte Carlo studies from this master thesis work will hopefully contribute to shed light and insight onto further investigations on this important aspect of the overall planning and building of particle therapy facilities in Norway.

Future Outlook

FLUKA is a powerful and versatile Monte Carlo simulation tool for general shielding applications. This project offers a generic foundation for future simulations and correlated experiments from which one can expand and further to create a data base applicable for detailed studies of the production of secondary particles and the corresponding generation of secondary dose to both the patients and the personnel at a particle therapy facility. The possibility of studying the effect of performing changes to the geometry and layout in advance of the actual building stage of a facility is very important, both with respect to minimization of unwanted particle production and with respect to pre-determination of which areas of a facility that requires special attention when performing the finalization of the radiation shielding design.

Among many of the challenges to be addressed in subsequent proton, helium, and carbon

beam simulations and shielding experiments we here list:

• In order to better approximate a clinical particle therapy treatment situation, apply the simulated distributions of equivalent dose in units of Sv, that take into account the higher RBE of helium and carbon ions should be implemented and used for normalization purposes.

• Introduce beam line components into the beam line; in the case of a spot scanning system, a detailed scanning nozzle with an ionization chamber and vacuum window.

• A rotating gantry moving the treatment beam around the patient that is creating new shielding modelling scenarios that demand further examinations and considerations regarding the treatment room and shielding barriers.

• Benchmark dose measurements in FLUKA with experimental data from an existing treatment facility that adequate dose surveillance system in place and simultaneously offering detailed drawings of building structures. This can be used as measurement verification in conjunction with simulation optimization.

• Study the secondary particle and dose production when applying other particle species than those in this master thesis study.

• Optimize FLUKA simulations with improved biasing regions and longer run times.

Bibliography

[1] F. H. Attix, *Introduction to Radiological Physics and Radiation Dosimetry*. Wiley-VCH Verlag GmbH & Co, 1986.

[2] W. R. Leo, *Techniques for Nuclear and Particle Physics Experiments: A how-to Approach*. Springer Verlag, 1994.

[3] E. B. Podgorsak, *Radiation Physics for Medical Physicists*. Springer Science & Business Media, 2010.

[4] J. E. Turner, *Atoms, Radiation, and Radiation Protection*. Wiley-VCH Verlag GmbH & Co, 2007.

[5] T. F. Thorsteinsen, *Kompendium i Strålingsfysikk*. Universitetet i Bergen, 1995.

[6] G. Knoll, *Radiation Detection and Measurement*. John Wiley & Sons, 2010.

[7] W. D. Newhauser and R. Zhang, "The physics of proton therapy," *Physics in medicine and biology*, vol. 60, no. 8, p. R155, 2015.

[8] M. F. R. Zhang, T.J. Phillip and W. D. Newhauser, "Water equivalent thickness values of materials used in beams of protons, helium, carbon and iron ions," *Physics in medicine and biology*, vol. 55, no. 9, pp. 2481–2493, 2010.

[9] S. Meroli, "Multiple scattering for particles in the matter." http://meroli.web.cern.ch/meroli/lecture_multiple_scattering.html, 2012, [Online; accessed 05-May-2015].

[10] D. Groom and S. Klein, "Passage of particles through matter," *The European Physical Journal C-Particles and Fields*, vol. 15, no. 1-4, pp. 163–173, 2014.

[11] T. E. D. Schardt and D. Schulz-Ertner, "Heavy-ion tumor therapy: Physical and radiobiological benefits," *Reviews of Modern Physics*, vol. 82, no. 1, p. 383, 2010.

[12] C. Leroy and P. G. Rancoita, "Principles of radiation interaction in matter and detection," *World Scientific*, vol. 2, 2009.

[13] Y. Yonekura, H. Tsujii, J.W. Hopewell, and others, *ICRP Publication 127: Radiological Protection in Ion Beam Radiotherapy.* SAGE, 2014.

[14] D. Aadnevik, "Extremely high-granularity digital tracking calorimeter for the detection of scattered protons in proton computed tomography," Master's thesis, University of Bergen, 2014.

[15] U. Linz, *Ion Beam Therapy: Fundamentals, Technology, Clinical Applications*. Springer Science & Business Media, 2011.

[16] D. S. K. Gunzert-Marx, H. Iwase and R. Simon, "Secondary Beam Fragments Produced by 200 MeV/u 12C ions in Water and their Dose Contributions in Carbon Ion Radiotherapy," *New Journal of Physics*, vol. 10, no. 7, p. 075003, 2008.

[17] G. Fehrenbacher, I. Gudowska, A. Mazal, H. Paganetti and others, "Shielding Design and Radiation Safety of Charged Particle Therapy Facilities," 2015.

[18] NCRP, *NCRP Report 144: Radiation Protection for Particle Accelerator Facilities*. National Council on Radiation Protection and Measurements, 2005.

[19] J. H. Hubbell and S. M. Seltzer, "Tables of x-ray mass attenuation coefficients and mass energy-absorption coefficients from 1 kev to 20 mev for elements z = 1 to 92 and 48 additional substances of dosimetric interest," "http://physics.nist.gov/PhysRefData/XrayMassCoef/chap2.html", 1996, "[Online; accessed 24-June-2015]".

[20] G. B. Saha, *Physics and Radiobiology of Nuclear Medicine, fourth edition*. Springer Science & Business Media, 2012.

[21] A. Thompson, I. Lindau, D. Atwood, and others, *Center for X-ray Optics and Advanced Light Source. X-ray Data Booklet*. Lawrence Berkeley National Laboratory, 2009.

[22] K. Johnsen, "Simulations of a therapeutic proton beam with fluka monte carlo code and varian ecplispe proton planning software," Master's thesis, University of Bergen, 2013.

[23] K. Ytre-Hauge, "Measurements of Neutron Doses from Radiotherapy with 12C Ions and Photons," Master's thesis, University of Bergen, 2009.

[24] P. Rinard, "Neutron interactions with matter," *Passive Nondestructive Assay of Nuclear Materials*, pp. 357–377, 1991.

[25] M.B. Chadwick, M. Herman, M.E. Dunn, and others, "ENDF/B-VII.1 Nuclear Data for Science and Technology: Cross Sections, Covariances, Fission Product Yields and Decay Data," pp. 2887–2996, 2011.

[26] E. D. N. Soppera, M. Bossant, "Janis 4: An improved version of the nea java-based nuclear data information system," pp. 294–296, 2014.

[27] R.B. Firestone, H.D Choi, R.M. Lindstrom, G.L. Molnar, and others, "Database of prompt gamma rays from slow neutron capture for elemental analysis," *Lawrence Berkeley National Laboratory*, 2004.

[28] ICRP, *ICRP Publication 103: 2007 Recommendations of the International Commission on Radiological Protection*. Elsevier Health Sciences, 2007.

[29] ——, *ICRP Publication 116: Conversion Coefficients for Radiological Protection Quantities for External Radiation Exposures*. Elsevier Health Sciences, 2010.

[30] ——, *ICRP Publication 60: 1990 Recommendations of the International Commission on Radiological Protection*. Elsevier Health Sciences, 1991.

[31] IAEA, *Radiation Biology: A Handbook for Teachers and Students*. IAEA, 2010.

[32] ICRP, "Icrp publication 92: Relative biological effectiveness (rbe), quality factor (q), and radiation weighting factor (w r)," *Annals of the ICRP*, vol. 33, no. 4, pp. 1–121, 2003.

[33] R. Wilson, "Radiological use of fast protons," *Radiology*, vol. 47, no. 5, pp. 487–491, 1946.

[34] M. Jermann, "Particle therapy statistics in 2014," *International Journal of Particle Therapy*, vol. 2, no. 1, pp. 50–54, 2015.

[35] E. Podgorsak *et al.*, *Radiation Oncology Physics: A Handbook for Teachers and Students*. IAEA, 2005.

[36] O. Jäkel, "Heavy ion radiotherapy," in *New Technologies in Radiation Oncology*. Springer, 2006, pp. 365–377.

[37] K. Ytre-Hauge, "Measurements and monte carlo simulations of neutron doses from radiation therapy with photons, protons and carbon ions," Ph.D. dissertation, Univeristy of Bergen, 2013.

[38] UNSCEAR, *Sources and Effects of Ionizing Radiation*. United Nations Publication, 2008.

[39] NCRP, "Ncrp report no. 160, ionizing radiation exposure of the population of the united states," 2009.

[40] UNSCEAR, *UNSCEAR 2000 REPORT Vol. II - Sources and Effects of Ionizing Radiation*, 2000.

[41] IAEA, "Radiation protection and safety of radiation sources: International basic safety standards," *IAEA Safety Standards Series No. GSR Part 3*, 2014.

[42] ——, "Radiation protection in the design of radiotherapy facilities," *IAEA Safety Reports Series No. 47*, 2006.

[43] B. A.F, *Fundamentals of the Monte Carlo Method for Neutral and Charged Particle Transport*. Citeseer, 2001.

[44] D. D. J.E. Turner and J. Bogard, *Statistical Methods in Radiation Physics*. Wiley-VCH, 2012.

[45] G. Battistoni, B. Francesco, M. Brugger, M. Campanella, M. Carboni and others, "Applications of FLUKA Monte Carlo Code for Nuclear and Accelerator Physics," *Nuclear Instruments and Methods in Physics Research Section B: Beam Interactions with Materials and Atoms*, vol. 269, no. 24, pp. 2850–2856, 2011.

[46] A. F. A. Ferrari, P.R. Sala and J. Ranft, "Fluka-2011 manual," http://www.fluka.org/fluka.php?id=man_onl, 2011.

[47] D. J. W. Chen, "Creating a spread-out bragg peak in proton beams," *Physics in Medicine and Biology*, vol. 56, no. 11, p. N131, 2011.

[48] M. Benedikt and A. Wrulich, "Medaustron—project overview and status," 2011. [Online]. Available: http://dx.doi.org/10.1140/epjp/i2011-11069-9

[49] "Treatment rooms at heidelberg ion-beam therapy center (hit)," http://www.klinikum.uni-heidelberg.de/index.php?id=116936&L=1, [Online; accessed 05-Sep-2015].

[50] J. A. Brennsæter, "Monte carlo simulations of neutron fluence through concrete wall in proton therapy," Master's thesis, Norwegian University of Science and Technology, 2014.

Appendix A

FLUKA Script

A.1 Input Cards

The FLUKA input card for creating a treatment room with a maze (RightMaze) and defining scoring detectors that determine dose in the worker (water) phantoms and differential fluence inside the maze region.

```
TITLE
* Set the defaults for precision simulations
DEFAULTS                                                              PRECISIO
* Define the beam characteristics
BEAM            -0.2      -0.0      -0.0       0.0      -0.0          PROTON
* Define the beam position
BEAMPOS                          -100.0
SOURCE
GEOBEGIN                                                              COMBNAME
    3    0
* Black body
SPH blkbody    0.0 0.0 0.0 100000.0
* Void sphere
SPH void       0.0 0.0 0.0 10000.0
SPH air        0.0 0.0 0.0 2500.0
RPP BIASBOX    -440.0 35.0 -120. 130. 40. 500.
RPP phantom    -35. 35. -10. 10. 0.0 40.
RPP innerBox   -440. 440. -120. 330. -800. 500.
RPP outerBox   -640. 640. -320. 530. -1000. 900.
RPP Worker1    -360. -320. -35. 35. 530. 550.
RPP Worker2    -520. -480. -35. 35. 690. 710.
RPP Worker3    -360. -320. -35. 35. 850. 870.
RPP Worker4    -520. -480. -35. 35. 940. 960.
RPP mazeShie   -640. -200. -320. 530. 500. 900.
RPP exit       -380. -300. -120. 80. 500. 660.
RPP L1         -540. -380. -120. 80. 580. 660.
RPP L2         -540. -460. -120. 80. 660. 740.
RPP L3         -540. -300. -120. 80. 740. 820.
RPP enter      -380. -300. -120. 80. 820. 900.
RPP OutAir1    -700. -100. -220. 330. 900. 1000.
RPP OutAir2    -700. -640. -220. 330. 400. 900.
END
* Black hole
BLKBODY      5 +blkbody -void
```

```
* Void around
VOID         5 +void -air
* Air around the treatment room
AIR          5 +air -outerBox -mazeShie -OutAir1 -OutAir2
* Air around the treatment room
ROOMAIR      5 +innerBox -BIASBOX -phantom
* Walls region
WALLS        5 +outerBox -BIASBOX -innerBox -mazeShie
* Walls region
MAZESHIE     5 +mazeShie -exit -L1 -L2 -L3 -enter -OutAir1 -OutAir2
* Air inside the treatment room
BIASBOX      5 +BIASBOX +innerBox -phantom
* Phantom target
PHANTOM      5 +air +phantom -BIASBOX
WORKER1      5 +Worker1 +exit
WORKER2      5 +Worker2 +L2
WORKER3      5 +Worker3 +enter
WORKER4      5 +Worker4 +OutAir1
HALLWAY      5 +mazeShie +exit -Worker1 -L1
               | +mazeShie +L1 -exit -L2
               | +mazeShie +L2 -Worker2 -L1 -L3
               | +mazeShie +L3 -L2 -enter
               | +mazeShie +enter -Worker3 -L3
OUTAIR1      5 +air +OutAir1 -Worker4 -mazeShie
OUTAIR2      5 +air +OutAir2 -mazeShie
END
       1.0       1.0       1.0       1.0       1.0       1.0       1.0
    56000.    56000.    56000.    56000.    56000.       1.0       1.0
       1.0
GEOEND
* Assign materials to the different regions
ASSIGNMA    BLCKHOLE   BLKBODY
ASSIGNMA      VACUUM      VOID
ASSIGNMA         AIR       AIR
ASSIGNMA    Concrete     WALLS
ASSIGNMA    Concrete  MAZESHIE
ASSIGNMA         AIR   BIASBOX
ASSIGNMA         AIR   ROOMAIR
ASSIGNMA         AIR   HALLWAY
ASSIGNMA         AIR   OUTAIR1
ASSIGNMA         AIR   OUTAIR2
ASSIGNMA       WATER   PHANTOM
ASSIGNMA       WATER   WORKER1
ASSIGNMA       WATER   WORKER2
ASSIGNMA       WATER   WORKER3
ASSIGNMA       WATER   WORKER4
* Concrete
* Concrete has a wide variation in density and composition. The above
* description is for poured structural concrete with 10% moisture
* content. Concrete block will have a density of about 2.05 g/cm3.
* Ranges of concrete composition are : C (8-25%), O (38-60%), Si (8-18%).
* Concrete composition can be analyzed cheaply by commercial laboratories.
MATERIAL                           2.34                              Concrete
COMPOUND        23.0    CARBON     40.0    OXYGEN      12.0   SILICONConcrete
COMPOUND        12.0   CALCIUM     10.0  HYDROGEN       2.0  MAGNESIUConcrete
BIASING          0.0                 1.   ROOMAIR   ROOMAIR
BIASING          0.0                 2.   PHANTOM   PHANTOM
BIASING          0.0                 5.   BIASBOX   BIASBOX
```

```
BIASING          0.0                 20.  MAZESHIE  MAZESHIE
BIASING          0.0                 20.   HALLWAY   HALLWAY
BIASING          0.0                 20.   WORKER1   WORKER1
BIASING          0.0                 20.   WORKER2   WORKER2
BIASING          0.0                 20.   WORKER3   WORKER3
BIASING          0.0                 40.   OUTAIR1   OUTAIR1
BIASING          0.0                 40.   WORKER4   WORKER4
BIASING          0.0                 40.   OUTAIR2   OUTAIR2
EMFCUT                 1.0E-5             BIASBOX   BIASBOX
EMFCUT                 1.0E-5            MAZESHIE  MAZESHIE
EMFCUT                 1.0E-5             HALLWAY   HALLWAY
EMFCUT                 1.0E-5             WORKER1   WORKER1
EMFCUT                 1.0E-5             WORKER2   WORKER2
EMFCUT                 1.0E-5             WORKER3   WORKER3
EMFCUT                 1.0E-5             WORKER4   WORKER4
EMFCUT                 1.0E-5             OUTAIR1   OUTAIR1
* Dose deposited in the maze
USRBIN           10.      DOSE      -21.    -200.0       10.     1000.mazeDo20
USRBIN        -690.0     -10.0     450.0      700.        8.     1100. &
* Energy deposited in the maze
USRBIN           10.    ENERGY      -22.    -200.0       10.     1000.mazeEn20
USRBIN        -690.0     -10.0     450.0      700.        8.     1100. &
* Proton Fluence in the maze (20cm slice)
USRBIN           10.    PROTON      -23.    -200.0       10.     1000.mazePr20
USRBIN        -690.0     -10.0     450.0      700.        8.     1100. &
* Helium Fluence in the maze (20cm slice)
USRBIN           10.  4-HELIUM      -24.    -200.0       10.     1000.mazeHe20
USRBIN        -690.0     -10.0     450.0      700.        8.     1100. &
* Neutron Fluence in the maze (20cm slice)
USRBIN           10.   NEUTRON      -25.    -200.0       10.     1000.mazeNe20
USRBIN        -690.0     -10.0     450.0      700.        8.     1100. &
* Photon Fluence in the maze (20cm slice)
USRBIN           10.    PHOTON      -26.    -200.0       10.     1000.mazePh20
USRBIN        -690.0     -10.0     450.0      700.        8.     1100. &
* Heavy ion Fluence in the maze (20cm slice)
USRBIN           10.  HEAVYION      -27.    -200.0       10.     1000.mazeHi20
USRBIN        -690.0     -10.0     450.0      700.        8.     1100. &
* Neutrons entering the maze hallway
USRBDX           99.   NEUTRON      -40.   BIASBOX   HALLWAY    16000.NeutEnt
USRBDX           0.5     1E-14      300.                            1. &
* Neutrons exiting the maze hallway
USRBDX           99.   NEUTRON      -41.   HALLWAY   OUTAIR1    16000.NeutExt
USRBDX           0.5     1E-14      200.                            1. &
* photons entering the maze hallway
USRBDX           99.    PHOTON      -42.   BIASBOX   HALLWAY    16000.PhotEnt
USRBDX           0.5      1E-5      300.                            1. &
* Photons exiting the maze hallway
USRBDX           99.    PHOTON      -43.   HALLWAY   OUTAIR1    16000.PhotExt
USRBDX           0.5      1E-5      200.                            1. &
* Protons entering the maze hallway
USRBDX           99.    PROTON      -44.   BIASBOX   HALLWAY    16000.ProtEnt
USRBDX           0.5      1E-4      300.                            1. &
* Protons exiting the maze hallway
USRBDX           99.    PROTON      -45.   HALLWAY   OUTAIR1    16000.ProtExt
USRBDX           0.5      1E-4      200.                            1. &
* Helium entering the maze hallway
USRBDX           99.  4-HELIUM      -46.   BIASBOX   HALLWAY    16000.He4Ent
USRBDX           0.5      1E-4      300.                            1. &
```

```
* Helium exiting the maze hallway
USRBDX           99.  4-HELIUM      -47.   HALLWAY   OUTAIR1    16000.He4Ext
USRBDX           0.5      1E-4      200.                           1. &
* HeavyIons entering the maze hallway
USRBDX           99.  HEAVYION      -48.   BIASBOX   HALLWAY    16000.HiEnt
USRBDX           0.5      1E-4      300.                           1. &
* HeavyIons exiting the maze hallway
USRBDX           99.  HEAVYION      -49.   HALLWAY   OUTAIR1    16000.HiExt
USRBDX           0.5      1E-4      200.                           1. &
* Neutron spectrum in Worker 1
USRTRACK         -1.   NEUTRON      -50.   WORKER1    56000.      300.work1Ne
USRTRACK         0.5   1.0E-14                                        &
* Neutron spectrum in Worker 2
USRTRACK         -1.   NEUTRON      -51.   WORKER2    56000.      200.work2Ne
USRTRACK         0.5   1.0E-14                                        &
* Neutron spectrum in Worker 3
USRTRACK         -1.   NEUTRON      -52.   WORKER3    56000.      100.work3Ne
USRTRACK         0.5   1.0E-14                                        &
* Neutron spectrum in Worker 4
USRTRACK         -1.   NEUTRON      -53.   WORKER4    56000.      100.work4Ne
USRTRACK         0.5   1.0E-14                                        &
* Photon Spectrum in Worker 1
USRTRACK         -1.    PHOTON      -54.   WORKER1    56000.      300.work1Pho
USRTRACK         0.5    1.0E-5                                         &
* Photon Spectrum in Worker 2
USRTRACK         -1.    PHOTON      -55.   WORKER2    56000.      200.work2Pho
USRTRACK         0.5    1.0E-5                                         &
* Photon Spectrum in Worker 3
USRTRACK         -1.    PHOTON      -56.   WORKER3    56000.      100.work3Pho
USRTRACK         0.5    1.0E-5                                         &
* Photon spectrum in Worker 4
USRTRACK         -1.    PHOTON      -57.   WORKER4    56000.      100.work4Pho
USRTRACK         0.5    1.0E-5                                         &
* Proton Spectrum in Worker 1
USRTRACK         -1.    PROTON      -58.   WORKER1    56000.      300.work1Pr
USRTRACK         0.5    1.0E-4                                         &
* Proton Spectrum in Worker 2
USRTRACK         -1.    PROTON      -59.   WORKER2    56000.      200.work2Pr
USRTRACK         0.5    1.0E-4                                         &
* Proton Spectrum in Worker 3
USRTRACK         -1.    PROTON      -60.   WORKER3    56000.      100.work3Pr
USRTRACK         0.5    1.0E-4                                         &
* Proton spectrum in Worker 4
USRTRACK         -1.    PROTON      -61.   WORKER4    56000.      100.work4Pr
USRTRACK         0.5    1.0E-4                                         &
* Helium Spectrum in Worker 1
USRTRACK         -1.  4-HELIUM      -62.   WORKER1    56000.      300.work1He4
USRTRACK         0.5    1.0E-4                                         &
* Helium Spectrum in Worker 2
USRTRACK         -1.  4-HELIUM      -63.   WORKER2    56000.      200.work2He4
USRTRACK         0.5    1.0E-4                                         &
* Helium Spectrum in Worker 3
USRTRACK         -1.  4-HELIUM      -64.   WORKER3    56000.      100.work3He4
USRTRACK         0.5    1.0E-4                                         &
* Helium spectrum in Worker 4
USRTRACK         -1.  4-HELIUM      -65.   WORKER4    56000.      100.work4He4
USRTRACK         0.5    1.0E-4                                         &
* HeavyIon Spectrum in Worker 1
```

```
USRTRACK         -1.  HEAVYION      -66.   WORKER1    56000.      300.work1Hi
USRTRACK         0.5    1.0E-4                                        &
* HeavyIon Spectrum in Worker 2
USRTRACK         -1.  HEAVYION      -67.   WORKER2    56000.      200.work2Hi
USRTRACK         0.5    1.0E-4                                        &
* HeavyIon Spectrum in Worker 3
USRTRACK         -1.  HEAVYION      -68.   WORKER3    56000.      100.work3Hi
USRTRACK         0.5    1.0E-4                                        &
* Proton spectrum in Worker 4
USRTRACK         -1.  HEAVYION      -69.   WORKER4    56000.      100.work4Hi
USRTRACK         0.5    1.0E-4                                        &
* Angular Yield of Neutrons exiting the Hallway (maze)
USRYIELD        124.   NEUTRON      -70.   HALLWAY   OUTAIR1          NeAngExt
USRYIELD        180.       0.0      180.       0.5   1.0E-14        3. &
* Angular Yield of Photons exiting the Hallway (maze)
USRYIELD        124.    PHOTON      -71.   HALLWAY   OUTAIR1          PhAngExt
USRYIELD        180.       0.0      180.       0.5    1.0E-5        3. &
* Equivalent Dose to Worker 1
USRBIN           12.   DOSE-EQ      -72.   WORKER1                    DoseEqW1
USRBIN       WORKER1                             1.        1.        1. &
* Equivalent Dose to Worker 2
USRBIN           12.   DOSE-EQ      -73.   WORKER2                    DoseEqW2
USRBIN       WORKER2                             1.        1.        1. &
* Equivalent Dose to Worker 3
USRBIN           12.   DOSE-EQ      -74.   WORKER3                    DoseEqW3
USRBIN       WORKER3                             1.        1.        1. &
* Equivalent Dose to Worker 4
USRBIN           12.   DOSE-EQ      -75.   WORKER4                    DoseEqW4
USRBIN       WORKER4                             1.        1.        1. &
* Total Dose to Worker 1
USRBIN           12.      DOSE      -76.   WORKER1                    DoseW1
USRBIN       WORKER1                             1.        1.        1. &
* Dose to Worker 1 from Neutrons
USRBIN           12.      DOSE      -77.   WORKER1                    NeutW1
USRBIN       WORKER1                             1.        1.        1. &
AUXSCORE      USRBIN   NEUTRON             NeutW1    NeutW1
* Dose to Worker 1 from Photons
USRBIN           12.      DOSE      -78.   WORKER1                    PhotoW1
USRBIN       WORKER1                             1.        1.        1. &
AUXSCORE      USRBIN    PHOTON            PhotoW1   PhotoW1
* Dose to Worker 1 from protons
USRBIN           12.      DOSE      -79.   WORKER1                    ProtoW1
USRBIN       WORKER1                             1.        1.        1. &
AUXSCORE      USRBIN    PROTON            ProtoW1   ProtoW1
* Dose to Worker 1 from helium 4
USRBIN           12.      DOSE      -80.   WORKER1                    HeliumW1
USRBIN       WORKER1                             1.        1.        1. &
AUXSCORE      USRBIN  4-HELIUM           HeliumW1  HeliumW1
* Dose to Worker 1 from Heavy Ions
USRBIN           12.      DOSE      -81.   WORKER1                    HiW1
USRBIN       WORKER1                             1.        1.        1. &
AUXSCORE      USRBIN  HEAVYION               HiW1      HiW1
* Total Dose to Worker 2
USRBIN           12.      DOSE      -82.   WORKER2                    DoseW2
USRBIN       WORKER2                             1.        1.        1. &
* Dose to Worker 2 from Neutrons
USRBIN           12.      DOSE      -83.   WORKER2                    NeutW2
USRBIN       WORKER2                             1.        1.        1. &
```

```
AUXSCORE      USRBIN   NEUTRON              NeutW2    NeutW2
* Dose to Worker 2 from Photons
USRBIN           12.      DOSE      -84.   WORKER2                    PhotoW2
USRBIN       WORKER2                             1.        1.        1. &
AUXSCORE      USRBIN    PHOTON             PhotoW2   PhotoW2
* Dose to Worker 2 from protons
USRBIN           12.      DOSE      -85.   WORKER2                    ProtoW2
USRBIN       WORKER2                             1.        1.        1. &
AUXSCORE      USRBIN    PROTON             ProtoW2   ProtoW2
* Dose to Worker 2 from helium 4
USRBIN           12.      DOSE      -86.   WORKER2                    HeliumW2
USRBIN       WORKER2                             1.        1.        1. &
AUXSCORE      USRBIN  4-HELIUM            HeliumW2  HeliumW2
* Dose to Worker 2 from Heavy Ions
USRBIN           12.      DOSE      -87.   WORKER2                    HiW2
USRBIN       WORKER2                             1.        1.        1. &
AUXSCORE      USRBIN  HEAVYION               HiW2      HiW2
* Total Dose to Worker 3
USRBIN           12.      DOSE      -88.   WORKER3                    DoseW3
USRBIN       WORKER3                             1.        1.        1. &
* Dose to Worker 3 from Neutrons
USRBIN           12.      DOSE      -89.   WORKER3                    NeutW3
USRBIN       WORKER3                             1.        1.        1. &
AUXSCORE      USRBIN   NEUTRON              NeutW3    NeutW3
* Dose to Worker 3 from Photons
USRBIN           12.      DOSE      -90.   WORKER3                    PhotoW3
USRBIN       WORKER3                             1.        1.        1. &
AUXSCORE      USRBIN    PHOTON             PhotoW3   PhotoW3
* Dose to Worker 3 from protons
USRBIN           12.      DOSE      -91.   WORKER3                    ProtoW3
USRBIN       WORKER3                             1.        1.        1. &
AUXSCORE      USRBIN    PROTON             ProtoW3   ProtoW3
* Dose to Worker 3 from helium 4
USRBIN           12.      DOSE      -92.   WORKER3                    HeliumW3
USRBIN       WORKER3                             1.        1.        1. &
AUXSCORE      USRBIN  4-HELIUM            HeliumW3  HeliumW3
* Dose to Worker 3 from Heavy Ions
USRBIN           12.      DOSE      -93.   WORKER3                    HiW3
USRBIN       WORKER3                             1.        1.        1. &
AUXSCORE      USRBIN  HEAVYION               HiW3      HiW3
* Total Dose to Worker 4
USRBIN           12.      DOSE      -94.   WORKER4                    DoseW4
USRBIN       WORKER4                             1.        1.        1. &
* Dose to Worker 4 from Neutrons
USRBIN           12.      DOSE      -95.   WORKER4                    NeutW4
USRBIN       WORKER4                             1.        1.        1. &
AUXSCORE      USRBIN   NEUTRON              NeutW4    NeutW4
* Dose to Worker 4 from Photons
USRBIN           12.      DOSE      -96.   WORKER4                    PhotoW4
USRBIN       WORKER4                             1.        1.        1. &
AUXSCORE      USRBIN    PHOTON             PhotoW4   PhotoW4
* Dose to Worker 4 from protons
USRBIN           12.      DOSE      -97.   WORKER4                    ProtoW4
USRBIN       WORKER4                             1.        1.        1. &
AUXSCORE      USRBIN    PROTON             ProtoW4   ProtoW4
* Dose to Worker 4 from helium 4
USRBIN           12.      DOSE      -98.   WORKER4                    HeliumW4
USRBIN       WORKER4                             1.        1.        1. &
```

```
AUXSCORE      USRBIN  4-HELIUM            HeliumW4  HeliumW4
* Dose to Worker 4 from Heavy Ions
USRBIN           12.      DOSE      -99.   WORKER4                    HiW4
USRBIN       WORKER4                            1.        1.        1. &
AUXSCORE      USRBIN  HEAVYION               HiW4      HiW4
* Set the random number seed
RANDOMIZ          1.
* Set the number of primary histories to be simulated in the run
START            1E6
STOP}
```

A.2 source.f User Routine

The fortran source.f file that defines the beam's energy, weight and initial position.

```
* CREATE SOURCE.FOR
* COPY SOURCE
*
*=== source ============================================================*
*
      SUBROUTINE SOURCE ( NOMORE )
      INCLUDE '(DBLPRC)'
      INCLUDE '(DIMPAR)'
      INCLUDE '(IOUNIT)'
      INCLUDE '(BEAMCM)'
      INCLUDE '(CASLIM)'
      INCLUDE '(FHEAVY)'
      INCLUDE '(FLKSTK)'
      INCLUDE '(IOIOCM)'
      INCLUDE '(LTCLCM)'
      INCLUDE '(PAPROP)'
      INCLUDE '(SOURCM)'
      INCLUDE '(SUMCOU)'
*-----------------------------------------------------------------------*
*
*
      DIMENSION CUMPR(0:51), ENEDGE(52)
*these corresponds to 51 entries in both CUMPR and ENEDGE
*-----------------------------------------------------------------------*
*
*
      LOGICAL LFIRST
      SAVE LFIRST
      DATA LFIRST / .TRUE. /
*-----------------------------------------------------------------------*
*Proton, Helium and Carbon must be seperated into individual source.f files.
*They are grouped together here in one file purely for ease of reading.
*Proton energy group   *Helium energy group   *Carbon energy group
DATA ENEDGE /           DATA ENEDGE /           DATA ENEDGE /
& 147.2945625711E-03,   & 147.4149412804E-03,   & 279.9634188908E-03,
& 147.8604514201E-03,   & 147.9435498732E-03,   & 281.021175846E-03,
& 148.4247559067E-03,   & 148.4707725823E-03,   & 282.0767793522E-03,
& 148.9874908402E-03,   & 148.9966215298E-03,   & 283.1302461547E-03,
& 149.5486707954E-03,   & 149.5211086585E-03,   & 284.1815927738E-03,
& 150.1083101186E-03,   & 150.0442457355E-03,   & 285.2308355086E-03,
& 150.6664229318E-03,   & 150.5660443558E-03,   & 286.2779904414E-03,
```

```
& 151.2230231383E-03,   & 151.0865159461E-03,   & 287.3230734421E-03,
& 151.7781244271E-03,   & 151.6056717678E-03,   & 288.3661001718E-03,
& 152.3317402777E-03,   & 152.1235229209E-03,   & 289.4070860866E-03,
& 152.8838839644E-03,   & 152.6400803466E-03,   & 290.4460464419E-03,
& 153.434568561E-03,    & 153.1553548311E-03,   & 291.4829962957E-03,
& 153.9838069447E-03,   & 153.6693570084E-03,   & 292.5179505123E-03,
& 154.5316118004E-03,   & 154.1820973631E-03,   & 293.5509237657E-03,
& 155.0779956249E-03,   & 154.693586234E-03,    & 294.5819305436E-03,
& 155.6229707305E-03,   & 155.2038338161E-03,   & 295.6109851499E-03,
& 156.1665492491E-03,   & 155.7128501642E-03,   & 296.6381017088E-03,
& 156.7087431358E-03,   & 156.220645195E-03,    & 297.6632941676E-03,
& 157.2495641724E-03,   & 156.7272286901E-03,   & 298.6865762997E-03,
& 157.7890239711E-03,   & 157.2326102985E-03,   & 299.7079617081E-03,
& 158.327133978E-03,    & 157.7367995393E-03,   & 300.7274638282E-03,
& 158.8639054762E-03,   & 158.2398058036E-03,   & 301.7450959304E-03,
& 159.399349589E-03,    & 158.7416383577E-03,   & 302.7608711237E-03,
& 159.9334772836E-03,   & 159.2423063447E-03,   & 303.7748023576E-03,
& 160.4662993736E-03,   & 159.7418187873E-03,   & 304.7869024256E-03,
& 160.9978265222E-03,   & 160.2401845899E-03,   & 305.7971839675E-03,
& 161.5280692454E-03,   & 160.7374125406E-03,   & 306.8056594721E-03,
& 162.0570379143E-03,   & 161.2335113136E-03,   & 307.8123412797E-03,
& 162.5847427587E-03,   & 161.728489471E-03,    & 308.8172415846E-03,
& 163.1111938689E-03,   & 162.2223554652E-03,   & 309.8203724378E-03,
& 163.6364011991E-03,   & 162.7151176404E-03,   & 310.821745749E-03,
& 164.1603745696E-03,   & 163.2067842349E-03,   & 311.8213732891E-03,
& 164.6831236694E-03,   & 163.6973633831E-03,   & 312.8192666927E-03,
& 165.2046580588E-03,   & 164.1868631167E-03,   & 313.8154374601E-03,
& 165.7249871716E-03,   & 164.6752913673E-03,   & 314.8098969595E-03,
& 166.2441203175E-03,   & 165.1626559678E-03,   & 315.8026564294E-03,
& 166.7620666845E-03,   & 165.6489646539E-03,   & 316.7937269801E-03,
& 167.2788353413E-03,   & 166.1342250662E-03,   & 317.7831195968E-03,
& 167.7944352388E-03,   & 166.6184447516E-03,   & 318.7708451405E-03,
& 168.308875213E-03,    & 167.101631165E-03,    & 319.7569143506E-03,
& 168.8221639868E-03,   & 167.583791671E-03,    & 320.7413378469E-03,
& 169.3343101719E-03,   & 168.064933545E-03,    & 321.7241261311E-03,
& 169.8453222709E-03,   & 168.5450639754E-03,   & 322.705289589E-03,
& 170.3552086792E-03,   & 169.0241900643E-03,   & 323.6848384919E-03,
& 170.8639776872E-03,   & 169.5023188296E-03,   & 324.6627829991E-03,
& 171.3716374815E-03,   & 169.9794572059E-03,   & 325.6391331588E-03,
& 171.8781961475E-03,   & 170.4556120465E-03,   & 326.6138989105E-03,
& 172.3836616704E-03,   & 170.930790124E-03,    & 327.5870900864E-03,
& 172.8880419377E-03,   & 171.4049981321E-03,   & 328.5587164127E-03,
& 173.3913447402E-03,   & 171.8782426869E-03,   & 329.5287875119E-03,
& 173.893577774E-03,    & 172.3505303281E-03,   & 330.4973129039E-03,
& 174.3898258549E-03/   & 172.82186752E-03/     & 331.4643020078E-03/
~
*   Cumulative spectrum (Beam Weights)
      DATA CUMPR / 0.D0,
*...+....1....+....2....+....3....+....4....+....5....+....6....+....7..
     & 0.0037617826,
     & 0.0113572171,
     & 0.0190511735,
     & 0.026847045,
     & 0.0347484179,
     & 0.0427590866,
     & 0.0508830711,
     & 0.0591246358,
     & 0.0674883104,
```

```
     & 0.0759789135,
     & 0.0846015784,
     & 0.0933617824,
     & 0.1022653795,
     & 0.1113186368,
     & 0.1205282764,
     & 0.1299015219,
     & 0.1394461518,
     & 0.14917056,
     & 0.1590838253,
     & 0.1691957909,
     & 0.1795171563,
     & 0.1900595838,
     & 0.2008358222,
     & 0.211859852,
     & 0.2231470558,
     & 0.2347144202,
     & 0.246580777,
     & 0.2587670911,
     & 0.2712968098,
     & 0.2841962879,
     & 0.2974953106,
     & 0.311227742,
     & 0.3254323398,
     & 0.3401537886,
     & 0.3554440301,
     & 0.3713639983,
     & 0.3879859229,
     & 0.4053964425,
     & 0.4237009038,
     & 0.4430294459,
     & 0.4635458611,
     & 0.4854609439,
     & 0.5090534391,
     & 0.5347046021,
     & 0.5629589238,
     & 0.5946399536,
     & 0.6310973585,
     & 0.6748275437,
     & 0.7315147259,
     & 0.822172059,
     & 1/
*----------------------------------------------------------------------*
*...+....1....+....2....+....3....+....4....+....5....+....6....+....7..
*----------------------------------------------------------------------*
      NOMORE = 0
*  +-------------------------------------------------------------------*
*  |  First call initializations:
      IF ( LFIRST ) THEN
*  |  *** The following 3 cards are mandatory ***
        TKESUM = ZERZER
        LFIRST = .FALSE.
        LUSSRC = .TRUE.
*  |  *** User initialization ***
      END IF
*  |
*  +-------------------------------------------------------------------*
*  Sample the energy group
```

```
      XI = FLRNDM(DUMMY)
      DO 500 K = 1, 52
        IF(XI .LE. CUMPR(K)) THEN
*Carbon: NEUGRP = K
          ENERGY = ENEDGE(K) -
     &     (XI-CUMPR(K-1))*(ENEDGE(K)-ENEDGE(K+1))/(CUMPR(K)-CUMPR(K-1))
          GO TO 600
        END IF
 500  CONTINUE
      STOP ' Failed to sample the energy group'
 600  CONTINUE
      kount=kount+1
*
*  Npflka is the stack counter: of course any time source is called it
*  must be =0
      NPFLKA = NPFLKA + 1
* Wt is the weight of the particle
      WTFLK (NPFLKA) = ONEONE
      WEIPRI = WEIPRI + WTFLK (NPFLKA)
* Particle type (1=proton.....). Ijbeam is the type set by the BEAM
* card
*  +-------------------------------------------------------------------*
*  |  Heavy ion:
      IF ( IJBEAM .EQ. -2 ) THEN
         IJHION = IPROZ  * 1000 + IPROA
         IJHION = IJHION * 100 + KXHEAV
         IONID  = IJHION
         CALL DCDION ( IONID )
         CALL SETION ( IONID )
         ILOFLK (NPFLKA) = IJHION
*  |
*  +-------------------------------------------------------------------*
*  |  Normal hadron:
      ELSE
         IONID  = IJBEAM
         ILOFLK (NPFLKA) = IJBEAM
      END IF
*  |
*  +-------------------------------------------------------------------*
* From this point .....
* Particle generation (1 for primaries)
      LOFLK (NPFLKA) = 1
* User dependent flag:
      LOUSE  (NPFLKA) = 0
* User dependent spare variables:
      DO 100 ISPR = 1, MKBMX1
         SPAREK (ISPR,NPFLKA) = ZERZER
 100  CONTINUE
* User dependent spare flags:
      DO 200 ISPR = 1, MKBMX2
         ISPARK (ISPR,NPFLKA) = 0
 200  CONTINUE
* Save the track number of the stack particle:
      ISPARK (MKBMX2,NPFLKA) = NPFLKA
      NPARMA = NPARMA + 1
      NUMPAR (NPFLKA) = NPARMA
      NEVENT (NPFLKA) = 0
      DFNEAR (NPFLKA) = +ZERZER
```

```
* ... to this point: don't change anything
* Particle age (s)
      AGESTK (NPFLKA) = +ZERZER
      AKNSHR (NPFLKA) = -TWOTWO
* Group number for "low" energy neutrons
      IGROUP (NPFLKA) = NEUGRP
* Kinetic energy of the particle (GeV)
*Proton:
      TKEFLK (NPFLKA) = ENERGY
*Helium:
*      TKEFLK (NPFLKA) = ENERGY*4.0D0
*Carbon:
*      TKEFLK (NPFLKA) = ENERGY*12.0D0
* Particle momentum
      PMOFLK (NPFLKA) = SQRT ( TKEFLK (NPFLKA) * ( TKEFLK (NPFLKA)
     *                       + TWOTWO * AM (ILOFLK(NPFLKA)) ) )
*  Cosines (tx,ty,tz)
      TXFLK  (NPFLKA) = UBEAM
      TYFLK  (NPFLKA) = VBEAM
      TZFLK  (NPFLKA) = WBEAM
*     TZFLK  (NPFLKA) = SQRT ( ONEONE - TXFLK (NPFLKA)**2
*    &                       - TYFLK (NPFLKA)**2 )
* Polarization cosines:
      TXPOL (NPFLKA) = -TWOTWO
      TYPOL (NPFLKA) = +ZERZER
      TZPOL (NPFLKA) = +ZERZER
* Particle coordinates [cm] that cover the volume in X and Y direction:
* Gaussian sigma 0.297(=0.7FWHM) to account for lateral spread of beam
*Proton:
      CALL FLNRR2(RGAUS1, RGAUS2)
      XFLK (NPFLKA) = (-3.43 + 0.297*RGAUS1)+ FLRNDM(DUMMY)*6.92
      YFLK (NPFLKA) = (-3.445 + 0.297*RGAUS2)+ FLRNDM(DUMMY)*6.905
      ZFLK (NPFLKA) = ZBEAM
*Helium:
*      CALL FLNRR2(RGAUS1, RGAUS2)
*      XFLK (NPFLKA) = (-3.15 + 0.297D0*RGAUS1)+ FLRNDM(DUMMY)*6.27
*      YFLK (NPFLKA) = (-3.15 + 0.297D0*RGAUS2)+ FLRNDM(DUMMY)*6.34
*      ZFLK (NPFLKA) = ZBEAM
*Carbon:
*      CALL FLNRR2(RGAUS1, RGAUS2)
*      XFLK (NPFLKA) = (-3.05 + 0.297*RGAUS1)+ FLRNDM(DUMMY)*6.1
*      YFLK (NPFLKA) = (-3.05 + 0.297*RGAUS2)+ FLRNDM(DUMMY)*6.1
*      ZFLK (NPFLKA) = ZBEAM
*  Calculate the total kinetic energy of the primaries: don't change
      IF ( ILOFLK (NPFLKA) .EQ. -2 .OR. ILOFLK (NPFLKA) .GT. 100000 )
     &   THEN
         TKESUM = TKESUM + TKEFLK (NPFLKA) * WTFLK (NPFLKA)
      ELSE IF ( ILOFLK (NPFLKA) .NE. 0 ) THEN
         TKESUM = TKESUM + ( TKEFLK (NPFLKA) + AMDISC (ILOFLK(NPFLKA)) )
     &          * WTFLK (NPFLKA)
      ELSE
         TKESUM = TKESUM + TKEFLK (NPFLKA) * WTFLK (NPFLKA)
      END IF
*  Flag this is prompt radiation
      LRADDC (NPFLKA) = .FALSE.
      RADDLY (NPFLKA) = ZERZER
*  Here we ask for the region number of the hitting point.
*     NREG (NPFLKA) = ...
```

```
*  The following line makes the starting region search much more
*  robust if particles are starting very close to a boundary:
      CALL GEOCRS ( TXFLK (NPFLKA), TYFLK (NPFLKA), TZFLK (NPFLKA) )
      CALL GEOREG ( XFLK  (NPFLKA), YFLK  (NPFLKA), ZFLK  (NPFLKA),
     &              NRGFLK(NPFLKA), IDISC )
*  Do not change these cards:
      CALL GEOHSM ( NHSPNT (NPFLKA), 1, -11, MLATTC )
      NLATTC (NPFLKA) = MLATTC
      CMPATH (NPFLKA) = ZERZER
      CALL SOEVSV
      RETURN
*=== End of subroutine Source ========================================*
      END
```

Appendix B

FLUKA Materials

Air
Note: Dry air (near sea level)
Density: $0.00120484 g/cm^3$
Mass fraction:
0.0001248 Carbon
0.755267 Nitrogen
0.231781 Oxygen
0.012827 Argon
Water
Note: Water liquid H2O
Density: $1.00 g/cm^3$
Molecular content:
2 Hydrogen
1 Oxygen
Concrete
Poured structural concrete with 10% moisture content.
Density: $2.34 g/cm^3$
Molecular content:
23 Carbon
40 Oxygen
12 Silicon
12 Calcium
10 Hydrogen
2 Magnesium
Boron
Note: Pure Boron
Density: $2.37 g/cm^3$
Atomic number: 5

Iron
Note: Pure Iron
Density: $7.874 g/cm^3$
Atomic number: 26
Steel
Note: Stainless-Steel (typical)
Density: $8.0 g/cm^3$
Molecular content:
18 Chromium
74 Iron
8 Nickel

Appendix C

FLUKA Simulation Setups

All geometry dimensions and their relative placements are measured in *cm* and centred in relation to the coordinate (0,0,0). Positive z-axis is the beam direction and is parallel to the floor, ceiling and flank walls. Initial beam start location is (0,0,-100) and its direction is represented by a red arrow in each of the respective two dimensional simulation layouts below. The main *patient phantom* is made of *water* has and the dimension $70 \times 20 \times 40$ and weighs a total of 54kg. It spans from -35cm to 35cm in x-direction, -10cm to 10cm in y-direction and 0cm to 40cm in z-direction. This is kept constant in all layouts where the patient phantom is present. The Target Volume inside the patient phantom spans from -2.5cm to 2.5cm in both x- and y-directions, and 15cm to 20cm in z-direction. Water equivalent phantoms dubbed *Workers* in featured simulations have the same dimensions as the patient phantom but are rotated and situated at the same height as the patient phantom and beam.

Table C.1: Each Simulation setup is identified by a name and have been running a certain number of primary particle to gain satisfactory statistics. Simulations marked with a '*' has biasing applied to them and the percentage of treatment particles is therefore not applicable. On average, all simulations ran for $\approx$ 90 hours.

Simulation Name Identification	Particle Type	Tot. # of Primaries Simulated	Percentage of Treatment Fraction	# of simulation cycles
WaterPhantom	Proton	300E6	0.52%	60
	Helium	100E6	0.75%	20
	Carbon	12E6	5.29%	12
ClosedRoom	Proton	275E6	0.47%	55
	Helium	64E6	0.48%	32
	Carbon	12E6	5.29%	12
RightMaze*	Proton	60E6	-	60
	Helium	16E6	-	32
	Carbon	2E6	-	10
RightMazeBoron*	Proton	60E6	-	60
	Helium	16E6	-	32
	Carbon	2E6	-	10
MiddleMaze*	Proton	50E6	-	50
	Helium	25E6	-	25
	Carbon	2.4E6	-	12
MiddleDoor*	Proton	80E6	-	40
	Helium	20E6	-	20
	Carbon	2.8E6	-	14
PrimaryBarrier*	Proton	36E6	-	36
	Helium	15E6	-	15
	Carbon	1.2E6	-	12
BeamDump*	Proton	36E6	-	36
	Helium	15E6	-	15
	Carbon	1.2E6	-	12

C.0.1 WaterPhantom

The *"WaterPhantom"* simulation is centred on a homogeneous *water* phantom functioning as the patient as described above.

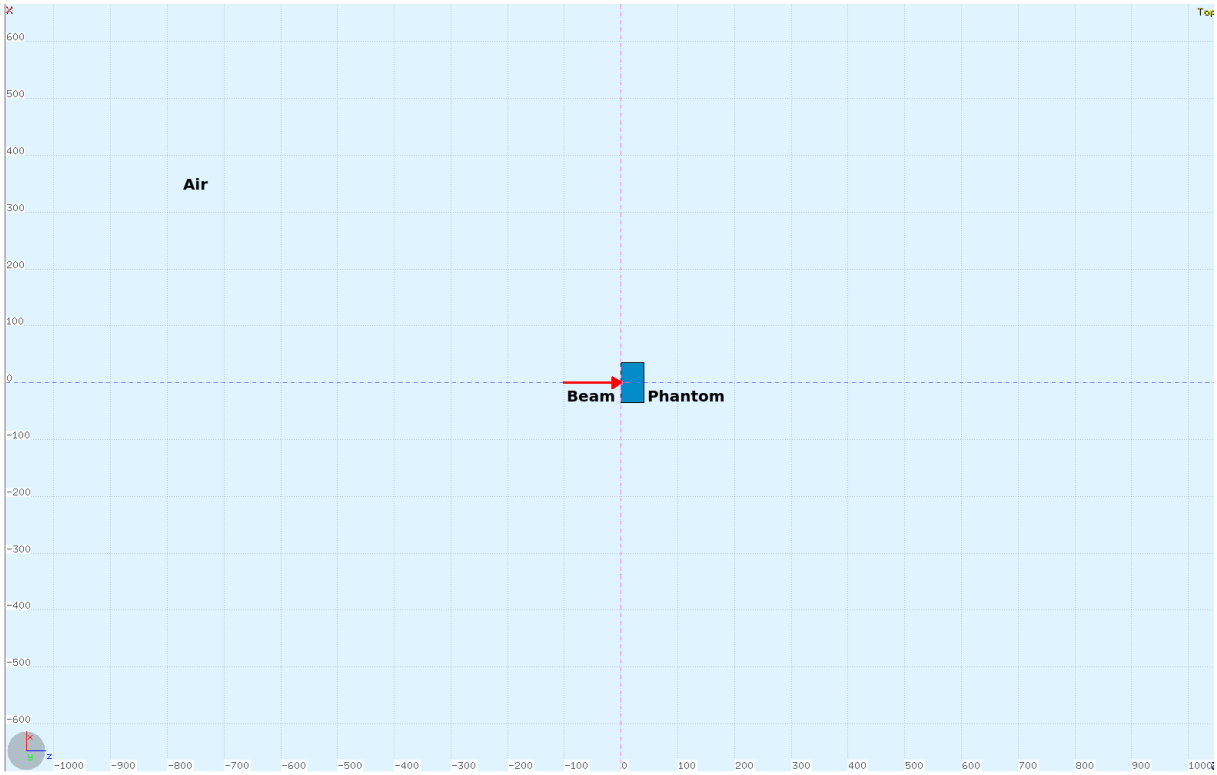

Figure C.1: Two dimensional layout drawing of the *WaterPhantom* setup in Geoviewer viewed along the y-axis (top-down view).

C.0.2 ClosedRoom

The *"ClosedRoom"* simulation introduces the treatment room walls that encompasses the patient phantom. The inside of the treatment room spans from -440cm to 440cm in x-direction, -120cm to 330cm in y-direction and -800cm to 500cm in z-direction. Each flank wall, back wall, floor and ceiling is 200cm thick and made of *concrete*. The primary front wall functioning as the primary barrier is 400cm thick and spans from -640cm to 640cm in x-direction, -320cm to 530cm in y-direction and 500cm to 900cm in z-direction. The red arrow illustrates the beam and its direction.

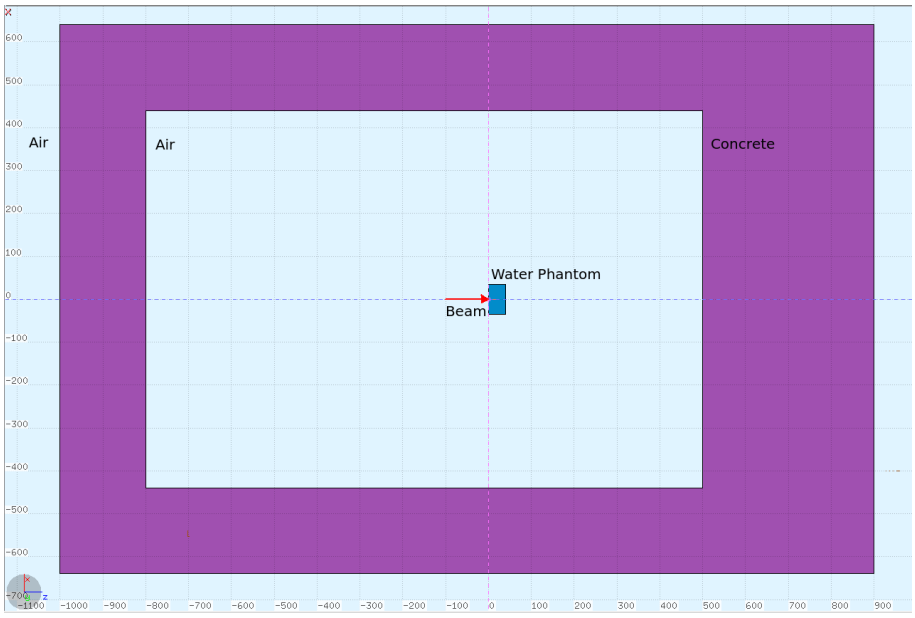

(a) Layout drawing of the treatment room setup in Geoviewer viewed along the y-axis (top-down view).

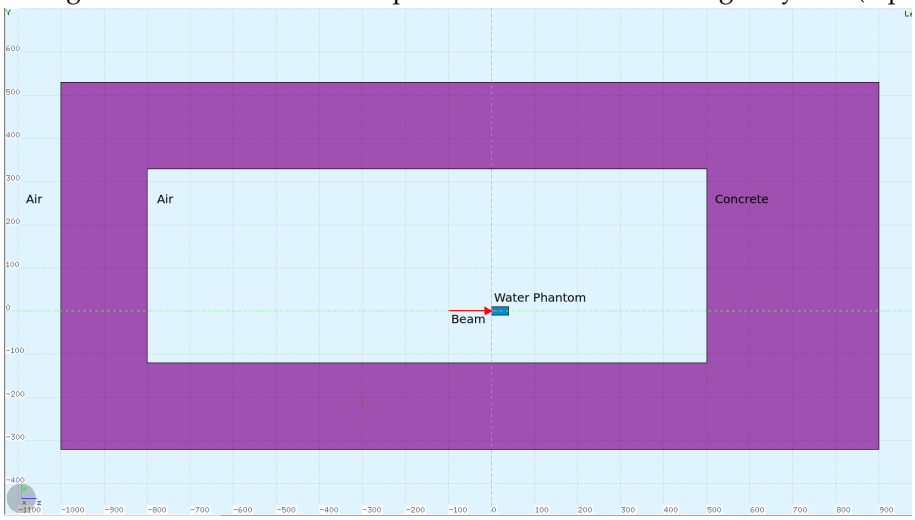

(b) Layout drawing of the treatment room setup in Geoviewer viewed along the x-axis (side view).

Figure C.2: The *"ClosedRoom"* setup in Geoviewer viewed from the top-down (a) and from the side (b).

C.0.3 RightMaze

The *"RightMaze"* simulation introduces the maze located inside the primary barrier as seen in the two-dimensional layout drawing, figure C.3. Each of the three maze arms are 80cm thick and the maze hallway cross section has the dimensions $80cm \times 200cm$ (door sized) in x and y respectively. Four water equivalent phantoms are placed inside and outside the maze and dubbed Worker1, Worker2, Worker3 and Worker4. They are made of water and have the same dimensions as the patient phantom, only rotated. The walls and maze arms are made of concrete.

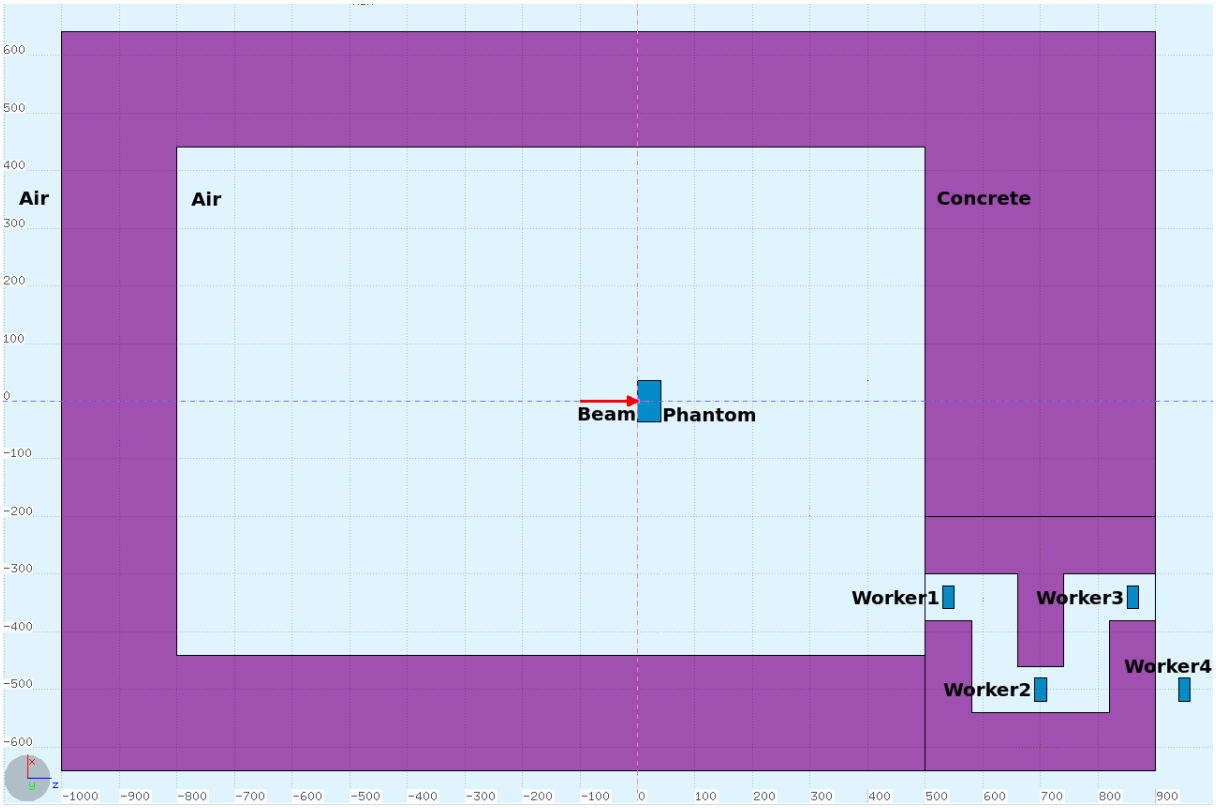

Figure C.3: Two dimensional layout of the *RightMaze* setup in Geoviewer and viewed along the Y-axis (top-down view).

C.0.4 RightMazeBoron

"RightMazeBoron" contains two 10cm thick boron layers (BoronLayer1 and BoronLayer2) that covers the first 10cm of the two inner maze arms. Otherwise the maze is identical to the maze found in *"RightMaze"*.

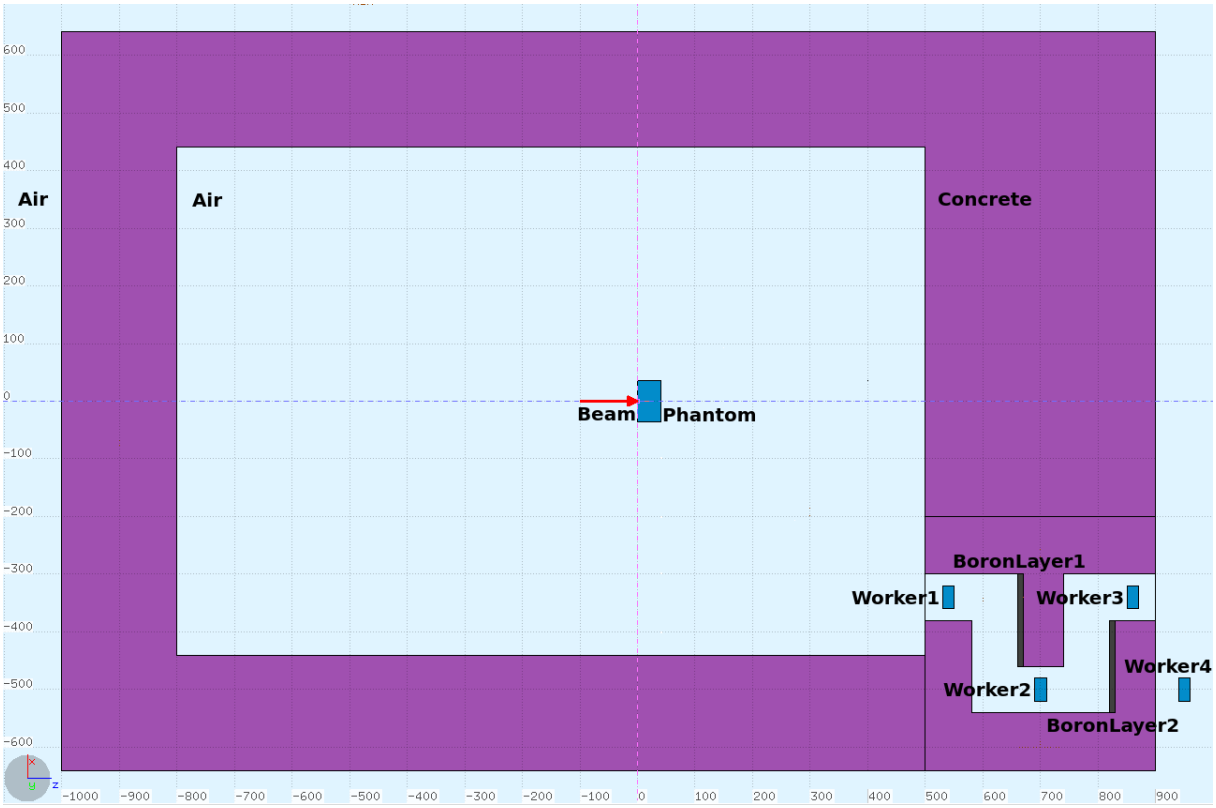

Figure C.4: Two dimensional layout of the *RightMazeBoron* setup in Geoviewer and viewed along the Y-axis (top-down view).

C.0.5 MiddleMaze

An identical maze as the one found in *"RightMaze"* and *"RihtMazeBoron"*is placed inside the right flank wall of the treatment room. The maze is made of concrete and four worker phantoms are placed at the positions shown in figure C.5.

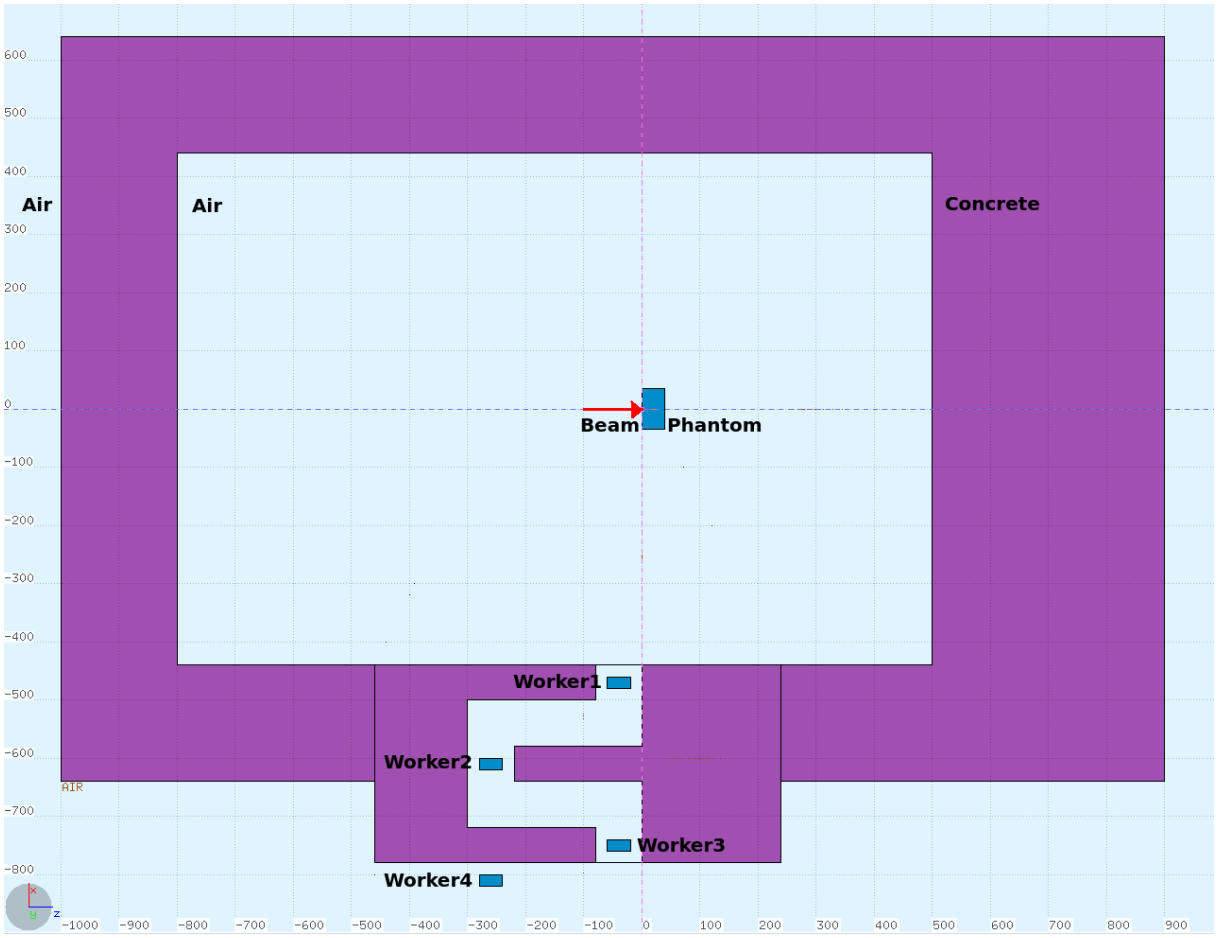

Figure C.5: Two dimensional layout of the *"MiddleMaze"* setup in Geoviewer and viewed along the Y-axis (top-down view).

C.0.6 MiddleDoor

In this simulation the maze (*"MiddleMaze"*) is exchanged with a straight corridor and a 100cm thick *iron* door in the middle of it. Two water phantoms, Worker3 placed directly outside the corridor, and Worker4 placed 150cm to the left of Worker3 and thus placing it behind the wall as illustrated in the layout drawing in figure **??**.

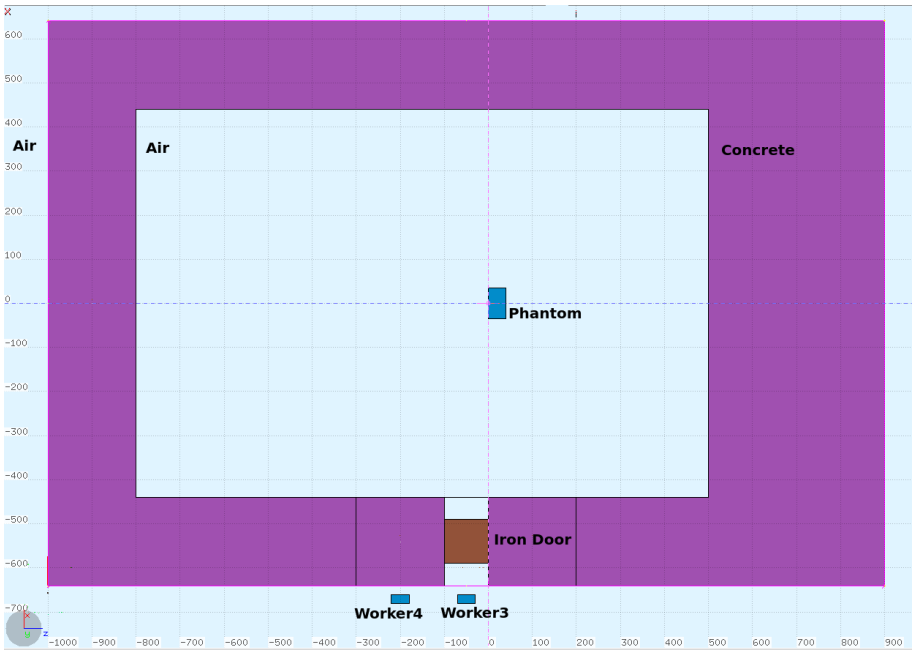

(a) Layout drawing of the middle door setup in Geoviewer viewed along the y-axis (top-down view).

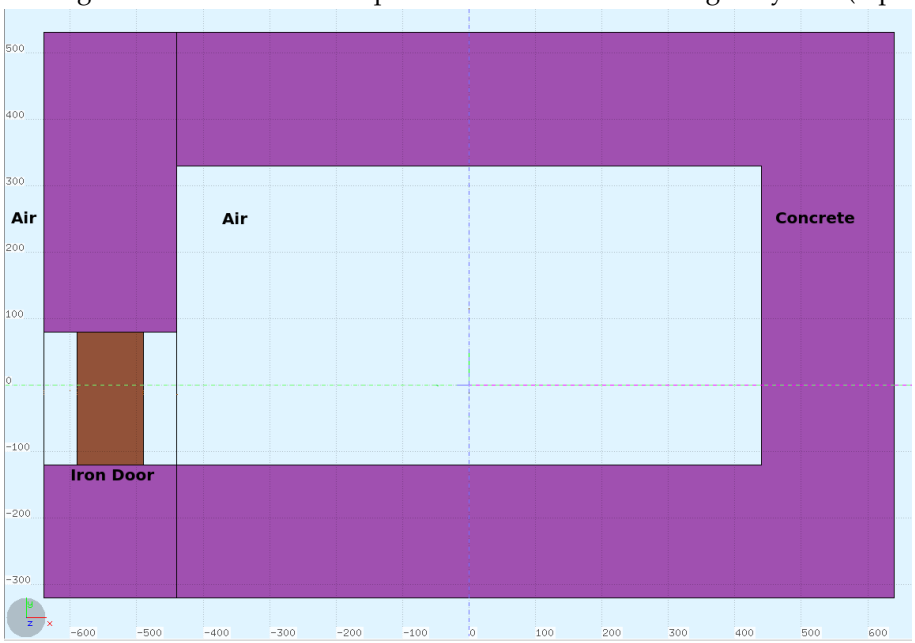

(b) Layout drawing of the middle door setup in Geoviewer viewed along the x-axis (side view).

Figure C.6: The *"MiddleDoor"* setup in Geoviewer viewed from the top-down (a) and from the side (b).

C.0.7 PrimaryBarrier

The primary barrier (front wall) is 400cm thick and divided into four regions equally spaced (100cm) for scoring purposes. A water equivalent phantom, Worker4 is placed on the other side of the primary wall at the same height as the patient phantom.

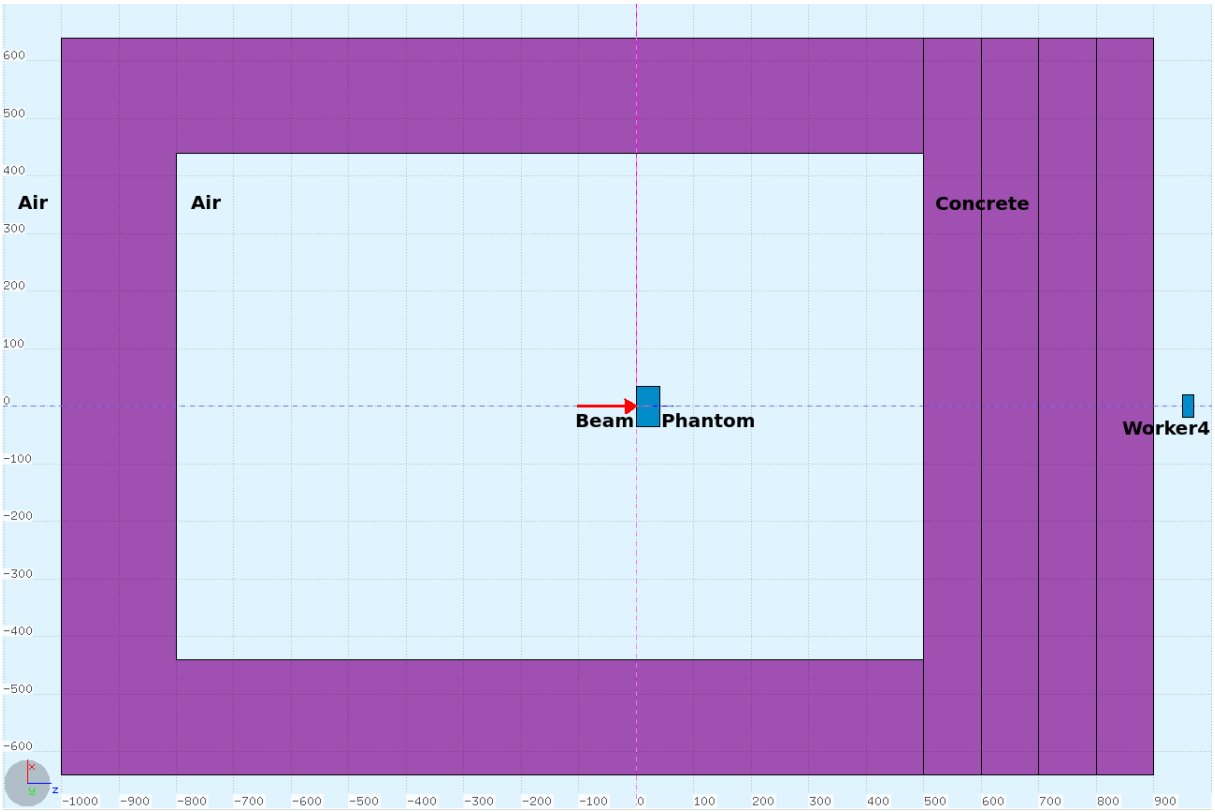

Figure C.7: Two dimensional layout of the *"PrimaryBarrier"* setup in Geoviewer and viewed along the Y-axis (top-down view).

C.0.8 BeamDump

This simulation differentiates itself from *"PrimaryBarrier"* by removing the patient phantom and adding a 30cm thick *steel* layer (SteelLayer) to the primary barrier.

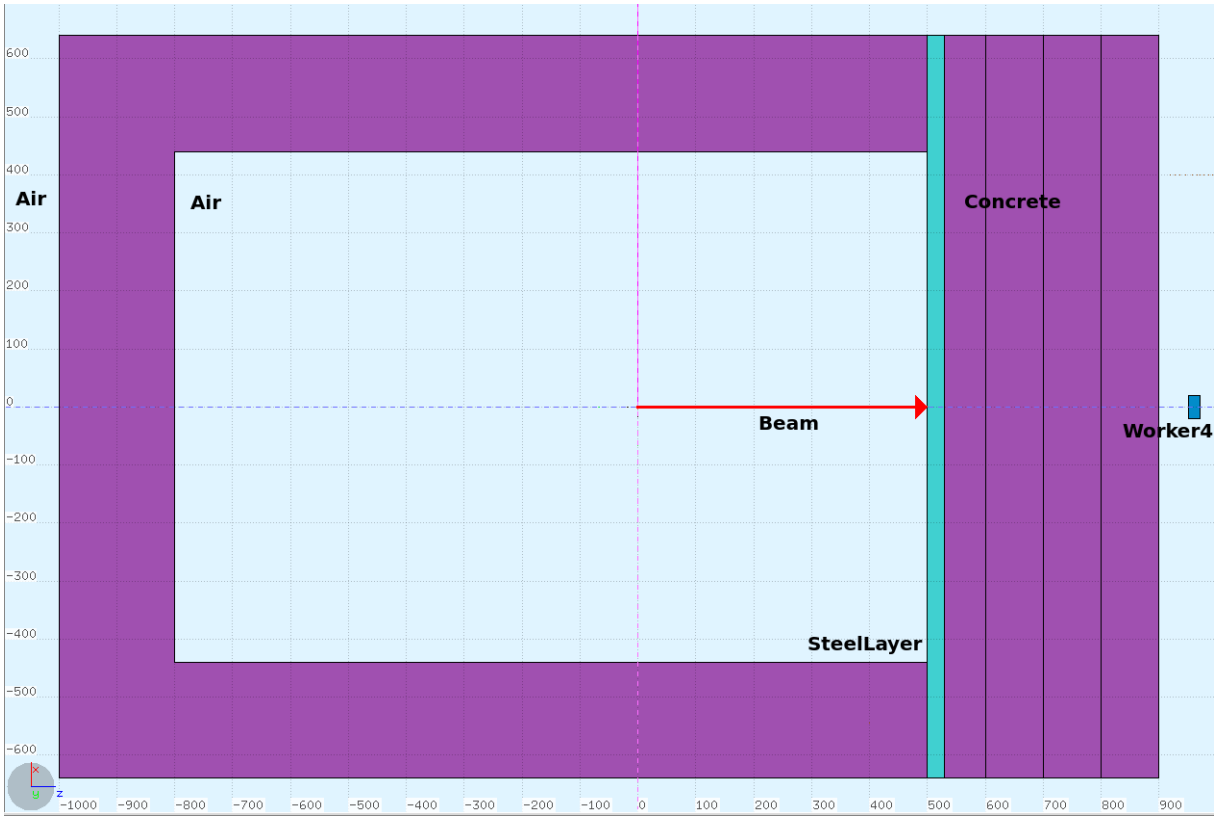

Figure C.8: Two dimensional layout of the *"BeamDump"* setup in Geoviewer and viewed along the Y-axis (top-down view).

Appendix D

Differential Fluence of Secondary Particles Exiting Treatment Phantom

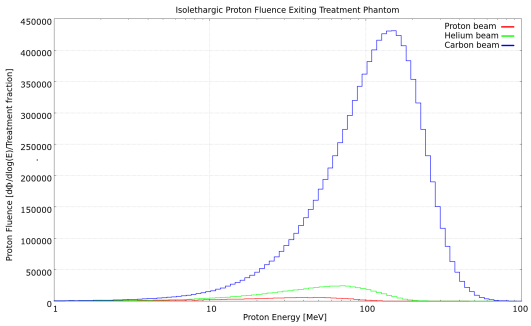

(a) Secondary Protons exiting the treatment phantom.

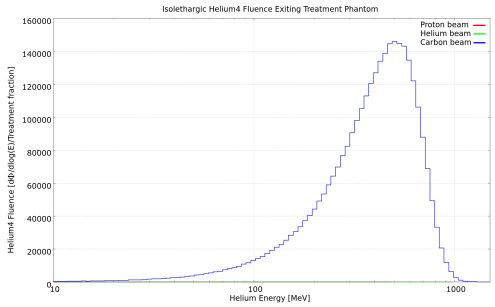

(b) Secondary helium 4 exiting the treatment phantom.

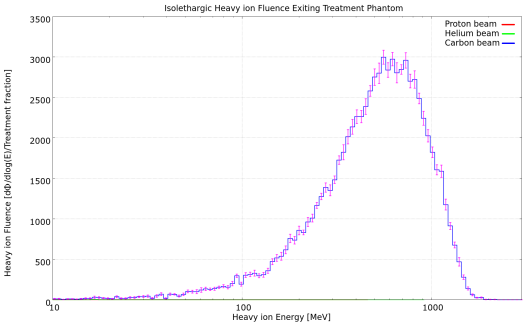

(c) Secondary particles heavier than helium 4 (A<4) exiting the treatment phantom.

Figure D.1: Differential fluence spectrum of some secondary fragmentation particles exiting the treatment phantom.

Appendix E

Treatment Phantom Dose and Fluence (Wall Comparison)

The difference between the absorbed dose and fluence in the treatment phantom with and without the treatment room walls, is obtained by subtracting the dose "Without Walls" from the dose "With Walls", which is expected to be higher due to backscattering. The measurements and results are listed in table E.1 below. Instances where there is no difference, or when the difference is smaller then the error, are marked with "-".

Table E.1: Total absorbed dose in the treatment phantom per treatment fraction [$Gy/treatment fraction$].

Simulated Particle	Dose Without Walls [Gy/treatment]	Dose With Walls [Gy/treatment]	Difference in absorbed dose	Relative change [%]
Proton	2.651E-2±1.788E-7	2.651E-2±2.326E-7	-	-
Helium	2.341E-2±3.768E-7	2.341E-2±5.068E-7	-	-
Carbon	2.562E-2±1.730E-6	2.561E-2±1.295E-6	-3.58E-6±1.51E-6	-0.01±0.006

The difference between the fluence in the treatment phantom is obtained by subtracting the fluence "Without Walls" from the fluence "With Walls", which is expected to be higher due to backscattering, and expressing it as a relative change [%]. The measurements and results are listed in table E.2 below. Instances where there is no difference or where the difference is smaller then the error, are marked with "-".

Table E.2: The fluence of selected secondary particles inside the treatment phantom normalised to treatment fraction [$n/cm^2/Treatment fraction$].

Simulated Particle	Particle fluence [$n/cm^2/treatment$]	Without Walls	With Walls	Change in fluence [%]
Proton	Secondary Protons	6.00E5±5.91E0	6.00E5±7.71E0	-
	Neutrons	4.20E6±9.36E2	4.21E6±1.05E3	0.29±0.02
	Photons	3.27E6±7.68E2	3.28E6±6.39E2	0.5±0.02
	He4	8.64E2±2.96E-1	8.64E2±2.75E-1	-
	Heavy Ions	2.86E1±1.94E-2	2.86E1±2.74E-2	-
Helium	Protons	6.97E5±2.04E2	6.97E5±2.58E2	-
	Neutrons	6.37E6±1.55E3	6.39E6±1.77E3	0.27±0.03
	Photons	2.59E6±6.10E2	2.61E6±7.93E2	0.82±0.03
	Secondary He4	2.38E4±9.08E-1	2.38E4±1.33E0	0.06±0.005
	Heavy Ions	3.48E2±3.84E-1	3.49E2±6.77E-1	-
Carbon	Protons	1.61E6±1.74E2	1.61E6±4.89E2	0.07±0.02
	Neutrons	5.41E6±1.67E3	5.42E6±2.83E3	0.3±0.04
	Photons	3.05E6±1.11E3	3.07E6±8.59E2	0.7±0.03
	He4	4.16E5±1.45E2	4.16E5±2.4E2	-
	Heavy Ions(-Carbon)	1.27E5±1.75E1	1.27E5±1.44E1	-

Appendix F

Effective Dose Measurements in Worker Phantoms

Table F.1: Collection of the effective dose to "Workers" per treatment fraction [$mSv/tr.frac.$] from each treatment beam simulated in each individual simulation setup.

Simulation Setup	Particle Type	Effective Dose to Worker1 [mSv/tr.frac.]	Effective Dose to Worker2 [mSv/tr.frac.]	Effective Dose to Worker3 [mSv/tr.frac.]	Effective Dose to Worker4 [mSv/tr.frac.]
RightMaze	Proton	1.04E-3±1.06E-5	1.02E-4±1.29E-6	4.07E-6±1.99E-7	8.26E-7±8.45E-8
	Helium	1.70E-3±1.28E-5	1.86E-4±1.74E-6	9.20E-6±2.41E-7	2.59E-6±1.65E-7
	Carbon	2.86E-3±1.34E-5	4.11E-4±3.02E-6	3.16E-5±5.76E-7	1.19E-5±5.99E-7
RightMazeBoron	Proton	1.04E-3±1.09E-5	9.84E-5±1.27E-6	3.94E-6±2.31E-7	1.03E-6±1.04E-7
	Helium	1.69E-3±9.01E-6	1.81E-4±1.71E-6	9.24E-6±3.87E-7	2.39E-6±1.44E-7
	Carbon	2.86E-3±1.34E-5	4.11E-4±3.02E-6	3.16E-5±5.76E-7	1.19E-5±5.99E-7
MiddleMaze	Proton	2.83E-4±4.56E-6	4.78E-6±1.79E-7	2.31E-6±3.70E-8	4.02E-8±1.81E-8
	Helium	4.20E-4±3.98E-6	7.76E-6±1.26E-7	3.78E-6±1.49E-7	1.01E-7±2.08E-8
	Carbon	4.59E-4±7.22E-6	1.04E-5±2.97E-7	6.22E-6±1.24E-6	1.91E-7±3.14E-8
MiddleDoor	Proton			1.29E-7±1.34E-8	5.92E-9±3.00E-9
	Helium	-	-	1.91E-7±1.86E-8	3.43E-8±1.77E-8
	Carbon			5.67E-7±2.51E-7	9.31E-8±2.93E-8
PrimaryBarrier	Proton				5.08E-8±3.93E-8
	Helium	-	-	-	1.39E-6±7.10E-8
	Carbon				1.07E-5±4.61E-7
BeamDump	Proton				1.06E-7±3.11E-8
	Helium	-	-	-	1.15E-6±1.41E-7
	Carbon				8.14E-6±2.66E-7